OPTICAL MULTICORE FIBER SHAPE SENSORS

A NUMERICAL AND EXPERIMENTAL PERFORMANCE ASSESSMENT

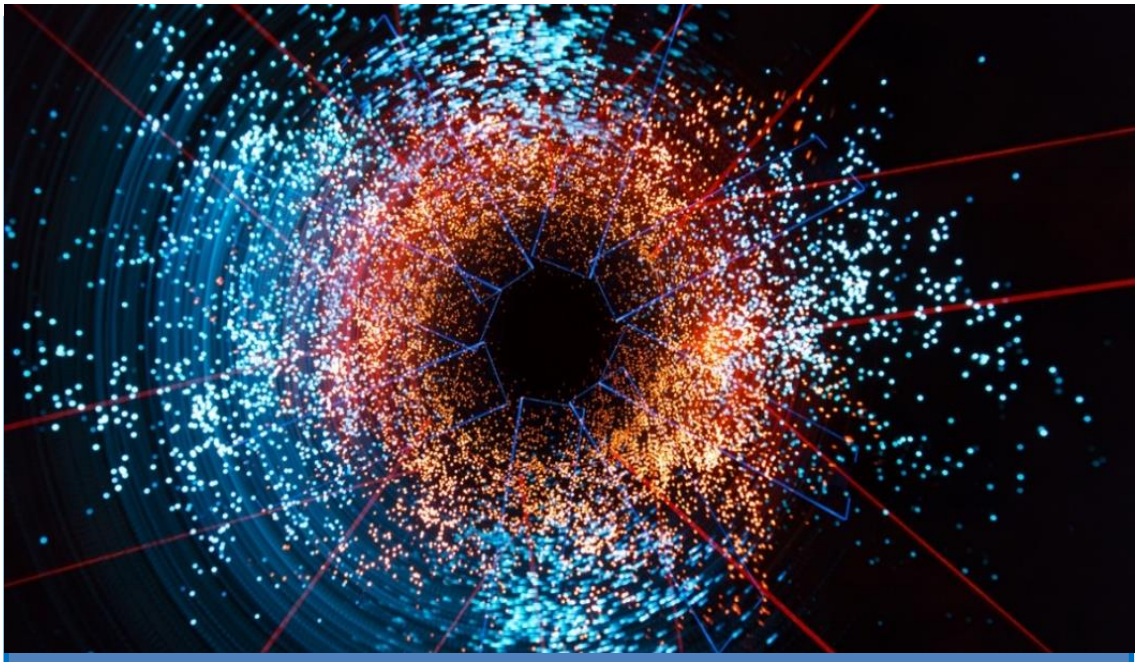

UNIVERSITAT POLITÈCNICA DE VALÈNCIA

A thesis submitted for the Degree of Doctor of Philosophy at the Universitat Politècnica de València

Candidate

Ignazio Floris

Thesis Supervisors

Prof. Dr. Jose M. Adam Martínez

Prof. Dr. Pedro A. Calderón García

May 2020


ICITECH
CIENCIA Y TECNOLOGÍA DEL HORMIGÓN
iTeAm
Instituto de Telecomunicaciones
y Aplicaciones Multimedia
MARIE CURIE ACTIONS
FINESSE

UNIVERSITAT POLITÈCNICA DE VALÈNCIA

INSTITUTE OF CONCRETE SCIENCE AND TECHNOLOGY

&

INSTITUTE OF TELECOMMUNICATIONS AND MULTIMEDIA APPLICATIONS

PHD IN BUILDING ENGINEERING

Optical Multicore Fiber Shape Sensors.

A numerical and experimental performance assessment

I am among those who think that science has great beauty.

(Maria Skłodowska-Curie)

ABSTRACT

Structural Health Monitoring (SHM) is a discipline that quantitatively assesses the integrity and performance of infrastructures, relying on sensors, and support the development of efficient Maintenance and Rehabilitation (M&R) plans. Optical Multicore Fiber (MCF) Shape Sensors offer an innovative alternative to traditional methods and enable the reconstruction of the deformed shape of structures directly and in real-time, with no need of computation models or visual contact and exploiting all the advantages of Optical Fiber Sensors (OFS) technology. Despite the intense research efforts centered on this topic by research groups worldwide, a comprehensive investigation on the parameters that influence the performance of these sensors has not been conducted yet.

The first part of the thesis presents a numerical study that examines the effects of strain measurement accuracy and core position errors on the performance of optical multicore fiber shape sensors in sensing three-dimensional curvature, which is at the basis of shape reconstruction. The analysis reproduces the strain measurement process using Monte Carlo Method (MCM) and identifies several parameters which play a key role in the phenomenon, including core spacing (distance between outer cores and sensor axis), number of cores and curvature measured. Finally, a set of predictive models were calibrated, by fitting the results of the simulations, to predict the sensors performance.

Afterward, an experimental study is proposed to evaluate the performance of optical multicore fiber in sensing shape, with particular focus on the influence of strain sensors length. Two shape sensors were fabricated, by inscribing long (8.0 mm) and short (1.5 mm) Fiber Bragg Gratings (FBG) into the cores of a multicore seven-core fiber. Thus, the performance of the two sensors was assessed and compared, at all the necessary phases for shape reconstruction: strain sensing, curvature calculation and shape reconstruction.

To conclude, an innovative approach, based on the Saint-Venant's Torsion Theory, is presented to determine the twisting of multicore fiber and to compensate the errors due to twisting during shape reconstruction. The efficiency of the theoretical approach was then corroborated performing a series of twisting tests on a shape sensor, fabricated by inscribing FBGs sensors into an optical spun multicore seven-core fiber.

The investigation of the mechanical behavior of multicore optical shape sensors has synergically involved diverse disciplines: Solid Mechanics, Photonics, Statistics and Data Analysis. Such multidisciplinary research has arisen from the prolific cooperation between the Institutes of the Institute of Science and Technology of

Concrete (ICITECH) and the Institute of Telecommunications and Multimedia Applications (iTEAM) - Photonics Research Labs (PRL) - of Universitat Politècnica de València (UPV), in addition to valuable collaboration with other members of the European ITN-FINESSE project, to which this work belongs.

This research work aims to enhance the performance optical multicore fiber shape sensors and support the development of new sensor geometries, with great potential for structural health monitoring applications.

RESUMEN

La Monitorización de la Salud Estructural (MSE) evalúa cuantitativamente la integridad y el comportamiento de las infraestructuras y permite desarrollar planes eficaces de Mantenimiento y Rehabilitación (M&R), utilizando los datos de los sensores. Sensores de forma basados en fibra óptica multinúcleo ofrecen una alternativa a los métodos tradicionales y permiten la reconstrucción de la deformada de estructuras de forma directa y en tiempo real, sin necesidad de modelos de cálculo o contacto visual y con todas las ventajas de la tecnología de los Sensores de Fibra Óptica (SFO). A pesar de los grandes esfuerzos en la investigación centrada en este tema por parte de los grupos de investigación de todo el mundo, todavía no se ha realizado una investigación exhaustiva que estudie los parámetros que influyen en el comportamiento de estos sensores.

En la primera parte de la tesis se presenta un estudio numérico en el que se examinan los efectos de la precisión de la medición de la tensión y los errores de posición del núcleo en el comportamiento de los sensores de forma basados en fibra óptica multinúcleo para definir la curvatura tridimensional, que es la base de la reconstrucción de la forma. El análisis reproduce el proceso de medición de la tensión utilizando el método de Monte Carlo (MC) e identifica una serie de parámetros que desempeñan un papel en el proceso, entre ellos la separación del núcleo (distancia entre los núcleos exteriores y el eje del sensor), el número de núcleos y la curvatura medida. Por último, se calibró un conjunto de modelos de predicción ajustando los resultados de las simulaciones para predecir el comportamiento de los sensores.

A continuación, se propone un estudio experimental para evaluar el comportamiento de los sensores de forma basado en fibra óptica multinúcleo, con especial atención en la influencia de la longitud de los sensores de deformación. Se fabricaron dos sensores de forma, inscribiendo Fiber Bragg Gratings (FBG) con longitudes de 8,0 mm y 1,5 mm en los núcleos de una fibra multinúcleo de siete núcleos. Así, se evaluó y comparó el comportamiento de los dos sensores en todas las fases necesarias para la reconstrucción de la forma, incluyendo la medición de la tensión, el cálculo de la curvatura y la reconstrucción de la forma.

Para concluir, se presenta un enfoque innovador, basado en la Teoría de la Torsión de Saint-Venant, para determinar la torsión de la fibra multinúcleo y compensar los errores debidos a la torsión durante la reconstrucción de la forma. La eficiencia del enfoque teórico fue verificada realizando una serie de pruebas de torsión en un sensor de forma, fabricado inscribiendo los sensores de FBGs en una fibra óptica multinúcleo torcida y siete núcleos.

La investigación del comportamiento mecánico de los sensores ópticos de forma multinúcleo ha involucrado sinérgicamente diversas disciplinas: Mecánica del sólido, Fotónica, Estadística y Análisis de datos. Esta investigación multidisciplinaria ha surgido de la prolífica cooperación entre el Instituto de Ciencia y Tecnología del Hormigón (ICITECH) y el Instituto de Telecomunicaciones y Aplicaciones Multimedia (iTEAM) – Laboratorio de Investigación Fotónica (LIF) - de la Universidad Politécnica de Valencia (UPV), además de la valiosa colaboración con otros miembros del proyecto europeo ITN-FINESSE, al que pertenece este trabajo.

Este trabajo de investigación puede permitir mejorar el comportamiento de los sensores de forma basados en fibra óptica multinúcleo y apoyar el desarrollo de nuevas geometrías de sensores, con un gran potencial para aplicaciones de control de la salud estructural.

RESUM

Structural Health Monitoring (SHM) avalua quantitativament la integritat i el comportament de les infraestructures i permet desenrotllar plans eficaços de Maintenance and Rehabilitation (M&R), utilitzant les dades dels sensors. Optical Multicore Fiber (MCF) Shape Sensors oferixen una alternativa als mètodes tradicionals i permeten la reconstrucció de la forma de la deformació de les estructures de forma directa i en temps real, sense necessitat de models de càlcul o contacte visual i amb tots els avantatges de l'Optical Fiber Sensors (OFS) Technology. A pesar dels grans esforços en la investigació centrada en aquest tema per part dels grups d'investigació de tot el món, encara no s'ha realitzat una investigació exhaustiva que estudie els paràmetres que influïxen en el comportament d'aquestos sensors.

En la primera part de la tesi es presenta un estudi numèric en què s'examinen els efectes de la precisió del mesurament de la tensió i els errors de posició del nucli en el comportament dels sensors de forma basats en fibra òptica multinucli per a definir la curvatura tridimensional, que és la base de la reconstrucció de la forma. L'anàlisi reproduïx el procés de mesurament de la tensió utilitzant el mètode de Monte Carlo (MC) i identifica una sèrie de paràmetres que exercixen un paper en el procés, entre ells la separació del nucli (distància entre els nuclis exteriors i l'eix del sensor), el nombre de nuclis i la mesura de la curvatura. Finalment, es va calibrar un conjunt de models de predicció ajustant els resultats de les simulacions per a predir el comportament dels sensors.

A continuació, es proposa un estudi experimental per a avaluar el comportament dels sensors de forma basat en fibra òptica multinucli, amb especial atenció en la influència de la longitud dels sensors de deformació. Es van fabricar dos sensors de forma, inscrivint Fiber Bragg Gratings (FBG) amb longituds de 8,0 mm i 1,5 mm en els nuclis d'una fibra multinucli de set nuclis. Així, es va avaluar i es va comparar el comportament dels dos sensors en totes les fases necessàries per a la reconstrucció de la forma, incloent el mesurament de la tensió, el càlcul de la curvatura i la reconstrucció de la forma.

Per a concloure, es presenta un enfocament innovador, basat en la Teoria de la Torsió de Saint-Venant, per a determinar la torsió de la fibra multinucli i compensar els errors deguts a la torsió durant la reconstrucció de la forma. L'eficiència de l'enfocament teòric va ser verificada realitzant una sèrie de proves de torsió en un sensor de forma, fabricat inscrivint els sensors de FBGs en una fibra òptica de set nuclis de filat múltiple.

La investigació del comportament mecànic dels sensors òptics de forma multinucli ha involucrat sinèrgicament diverses disciplines: Mecànica del sòlid, Fotónica,

Estadística i Anàlisi de dades. Aquesta investigació multidisciplinària ha sorgit de la prolífica cooperació entre l'Institut de Ciència i Tecnologia del Formigó (ICITECH) i l'Institut de Telecomunicacions i Aplicacions Multimèdia (iTEAM) – Laboratori de investigación fotònica (LIF) - de la Universitat Politècnica de València (UPV), a més de la valuosa col·laboració amb altres membres del projecte europeu ITN- FINESSE, al qual pertany aquest treball.

Aquest treball d'investigació pot permetre millorar el comportament dels sensors de forma basats en fibra òptica multinucli i ajudar al desenrotllament de noves geometries de sensors, amb un gran potencial per a aplicacions de control de la salut estructural.

ACKNOWLEDGMENTS

First and foremost, I would like to express my profound and sincere gratitude to my Thesis's supervisors, Professor Jose M. Adam and Professor Pedro A. Calderón, and my supervisor in the European Project FINESSE, Professor Salvador Sales. Their knowledge and guidance helped me in all the times of my research and writing this thesis. It has been a great honor and pleasure working with them.

I am grateful to all my colleagues from the ICITECH (Instituto de Ciencia y Tecnología del Hormigón), especially to Vicent Penadés, Manolo Buitrago, Enrique Serra, for the time we spent together, for their support and interesting discussions. I would like to express my deep gratitude to Rafael Shehu and Valentino Sangiorgio for their friendship, their support and their enthusiasm. A special thank you to all the members of the ITN-FINESSE framework from been incredibly kind and helpful throughout.

I would like to greatly thank the European Union's Horizon 2020 Research and Innovation Program that funded the research described in this thesis under the Marie Sklodowska-Curie Action Grant Agreement N° 722509.

Lastly and most significantly, I would like to express my deepest and sincere gratefulness to my family for the love and the support all these years. Without their constant trust and support, it would have been impossible to successfully finish this intense period of my career.

Finally, I would like to thank Valencia and its surroundings that will remain fond in my memory.

CONTENTS

LIST OF FIGURES

LIST OF TABLES

CHAPTER 1

INTRODUCTION AND OBJECTIVES

1.1 Introduction

Civil infrastructures are an integral part of modern economies and societies. The transport of goods and people depends on the reliable operation of railways, roads, bridges and tunnels. Dams and water distribution systems provide clean water for agriculture, households, and manufacturing. The production of energy is based on the correct operation of wind turbines, dams, pipelines, gas and oil platforms.

Because of corrosion, aging, and fatigue, caused by stress cycling, the structural integrity of the aforementioned components degrades over time. This deterioration can happen gradually or suddenly, as a result of unexpected loading or extreme natural events such as earthquakes, tornados or inundations. Frequent and careful inspections in addition to efficacious Maintenance and Rehabilitation (M&R) plans can contain degradation, prevent disasters and extend infrastructure lifetime.

Over the past decades, most of the existing civil infrastructures have exceed their exceeded service life and their conditions have gravely deteriorated. To cite an instance, the American Society of Civil Engineers reported in 2017 that 39% of the bridges in the United States were more than 50 years old, as shown in Fig. 1.1., and 9.1% of them were structurally deficient, while the cost for their rehabilitation was estimated to be $123 billion [1]. The same report evinces that dams were also in extremely serious conditions, since their average age was 56 years and 17% of them were identified as high-hazard potential, while an investment of nearly $45 billion would have been necessary to repair aging and resolve the criticalities.

Such structurally deficient rating has attracted a great deal of attention in aftermath of various recent catastrophic bridges collapses that have risen concern in the scientific and technical community. Kinzua Bridge, State Park, Pennsylvania, partially collapsed in July 2003 during a tornado. In August 2007 Mississippi River Bridge, Minneapolis, Minnesota, collapsed, killing 13 people and injuring 145. Subsequent investigations demonstrated that the bridge had been rated structurally deficient prior to its catastrophic failure, while the cause of collapse was resulted to be an under-designed gusset plate [2]. In March 2018, the concrete pedestrian bridge of the Florida International University campus in Miami, Florida, while still under construction, disastrously collapsed onto the Tamiami Trail (U.S. Route 41) resulting in 6 deaths and 8 injuries. An examination conducted by the Federal Highway Administration found faults in the structural design, consisting in an

overestimation of the strength of the bridge in the region that failed in addition to an underestimation of the design load [3,4]. More recently, the Morandi Bridge, Genoa, Italy, officially Viadotto Polcevera, ruinously collapsed in August 2018, resulting in 43 fatalities and 9 injuries. After investigation, the bridge was proved to be structurally deficient and the steel cables were found to be corroded [5].

From such context comes the urgent necessity for effective monitoring systems and for the definition of the concept of Structural Health Monitoring (SHM).

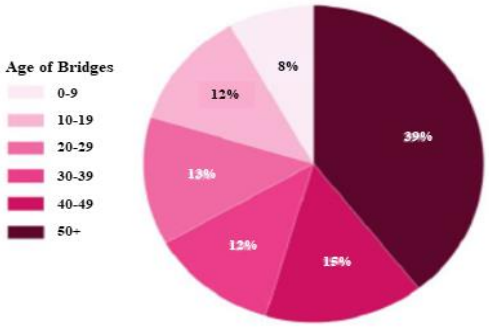

Fig. 1.1. Age of the American Bridges [1].

Fig. 1.2. Aftermath of Morandi Bridge collapse, Genoa, Italy (August 2018). The tragedy killed 43 people and left 600 homeless [6].

1.2 Structural Health Monitoring and Sensors

The objective of structural health monitoring of existing building, civil structures and infrastructures is the continuous and non-destructive evaluation of the structural integrity based on the measurement of key structural and environmental parameters. The deployment of SHM systems, thanks to more frequent and more quantitative assessments, does ensure the development of efficacious maintenance and rehabilitation plans and guarantees the selection of the most cost-effective interventions, being carried out at the proper moment. Moreover, it remarkably mitigates the hazard to human life.

Structural health monitoring involves the integration of one or several of the following components: visual inspection techniques, sensors, smart materials, data transmission, computational power, and processing ability. Even though the majority of the M&R strategies rely heavily on intermittent visual inspection techniques, the installation of sensors for SHM purposes has long been proved to be a notably more effective alternative [7–12].

Lopez-Higuera et al. proposes a worthwhile SHM classification according to different levels of knowledge [13]:

Level I) Is the structure damaged? Simple damage detection;

Level II) Where is the damage? Damage localization;

Level III) How severe is the damage? Severity assessment;

Level IV) How long will the structure survive? Lifetime prognostication.

Level V) Automatization. Self-prognosis, self-diagnosis, and self-healing.

Several types of sensors and methods can be utilized to achieve these objectives [8].

Strain Gages [14,15] and Fiber Bragg Gratings [16] are widely used to directly measure strain. Strain measurements provide valuable information for damage detection purposes and allow the implementation of stress–strain analysis to determine the level of stress in the material, in a single component or in the whole structure. Regrettably, the installation of these sensors can be costly. Furthermore, complex models need to be developed and significant approximations are required to understand the structure behavior from the limited number of measurement points [17].

Acoustic Emission (AE) sensors are able to detect high frequency elastic waves in structural component in the range of 0.5-3 MHz and can be employed to identify crack propagation and monitor its evolution [18,19]. Guided Wave Testing (GWT) is a non-destructive evaluation method that utilizes ultrasonic mechanical waves, which are propagated by actuators in structures and then detected using sensors. The damage in the structure can be identified from the changes in wave propagation,

although, frequently, the analysis is difficult, and the accuracy of the results is low. These sensors are mostly employed to monitor the health conditions of simple structures, such as plate systems or pipelines.

Vision-based approaches for SHM of civil infrastructure offer a noncontact alternative to sensors employment [20,21]. A vision-based measurement system consists of image acquisition devices, computers, and an image processing software. The data collected from cameras are processed with specific numerical algorithms to obtain the mechanical parameters for structural monitoring, detect visual abnormalities or cracks and extract displacement time histories. Image processing techniques can provide an alternative to manual inspections, but suffer from the same limitation [12]: inability to realize in the field continuous monitoring due to complicated site conditions; infrastructure closure during the data acquisitions; uncertain ability of the algorithm to recognize different structural distresses. In addition to camera-based methods, radio detection and ranging (RADAR) has been implemented in structural health monitoring [22–24], allowing the deformation tracking of large structure, but with lower accuracy.

Vibration-based damage identification methods, generally performed using accelerometers, are one of the most broadly used approaches in civil infrastructure health monitoring, since it permit the understanding of the global structural behavior with a limited number of sensors and measurement points [25–27]. Vibration-based damage detection approaches can generally be divided into: model-based and data-based. Model-based methods for damage identification consist in the comparison of the measured structural response with predictions resulting from computational models of the analyzed structure [28]. The presence of damage in the structure, as well as its localization and its severity assessment, can be determined from the differences between predicted and measured data. The main limitation of this method is that the development of an accurate computational models is not always easy and, sometimes, not even possible. Data-based approaches rely on pattern recognition algorithms and compare data obtained from the intact and the damaged structure [29]. The principal limitations of these approaches are that data of one or more damaged conditions are generally not available *a priori*, and, in the case of existing structures, even the data from the intact structure are, oftentimes, not available.

All the previous approaches present several limitations, in particular, the necessity of complex computational models or numerical algorithms to analyze the data and interpret the global structure behavior. Shape sensing based on Optical Fiber Sensors offers a valuable alternative to the traditional approaches. Optical Multicore Fiber Shape Sensors consist in optical cables that allow the continuous, dynamic and direct tracking of the structure shape without any necessity of visual contact. The advantages of such technology are multiple:

I) Ability to sense the deformed shape of the structure directly, without computational and numerical models and with no necessity of approximations

or assumptions about the characteristic of the structure, such as mass, stiffness, mechanical properties;

II) Ease of installation in civil structures, being the sensor a single cable;

III) No need for visual contact;

IV) Capability of continuous, dynamic, real-time and durable monitoring with no need of infrastructure closure for data acquisition;

V) Advantages of optical fiber sensor technologies (illustrated in the following Section).

In the light of the above, it results crucial the comprehensive investigation of this innovative technology.

1.3 Shape sensing based on Optical Fiber Sensors

Optical Fiber Sensors (OFS) have undergone a tremendous expansion over the last few decades (see Fig. 1.3) in several different fields [30], such as engineering [31,32], industrial [33], medical [34], chemical [35,36] and biological [37,38]. The principal reasons behind this substantial growth are their considerable advantages over their electrical counterparts, including compactness, lightweight, electrically passive operation, resistance to harsh environments, and multiplexing capabilities. Besides, OFSs have an inherent ability to sense a variety of measurands (as defined by [39]) in continuous development, such as strain [40,41], temperature [36], moisture [42], vibrations [43], chemical agents [38], and many others [44], using the optical fiber itself as a sensor.

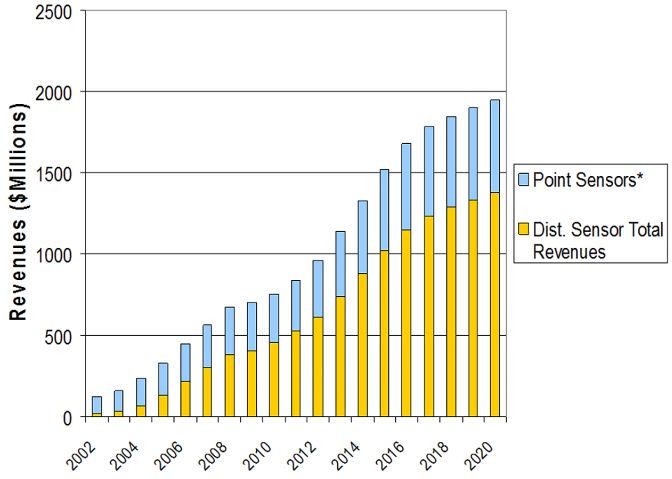

Fig. 1.3. Point sensor and distributed sensor market revenue and forecast, 2002–2020. Sources: historical data from Light Wave Ventures, OIDA forecast from member input. Courtesy of OIDA [13].

One of the current frontier of the fiber-optic sensing technologies is shape sensing [45], which has been an area of great interest for many researchers and consists in the possibility to dynamically track position and shape of an optical fiber. Fiber Optic Shape Sensors (FOSS) consist of optical Multicore Fibers (MCF) (or sometimes multi-fiber cables, with the same section geometry but larger core spacing) capable of sensing multidimensional curvature along the sensor's length, by comparing the longitudinal strain detected in different cores, and, hence, reconstructing shape [46].

Since curvature sensing using Fiber Bragg Gratings (FBG) inscribed in different cores of a MCF was first reported almost 20 years ago [47], a lot of progress has been made in this new branch. The two-dimensional shape of a multicore fiber was estimated based on distributed strain measurement [48,49]. An innovative approach for the three-dimensional shape reconstruction of a multicore optical fiber based on the numerical integration a set of Frenet-Serret equations was proposed by Moore and Rogge [50]. As a consequence, this emerging technology has become attractive for its possible application in many fields. Fiber-optic shape sensing based on FBGs written into a MCF was employed in catheters, needles and minimally invasive surgery systems [34,51,52]. Tunnel monitoring was performed using multicore fiber displacement sensor [53]. Barrera et al. demonstrated a multicore optical fiber shape sensors suitable for use under gamma radiation [54].

Notwithstanding the extensive research that has been focused on this novel topic, an in-depth study on the parameters that influence the performance of optical multicore fiber shape sensors is still missing. This research work will examine such aspect with the aim of assessing the performance of these sensors and enhancing their accuracy.

1.4 Objective and scope of this study

The overall aim of this PhD Thesis is to assess the performance of optical multicore fiber shape sensor with embedded strain sensors. To achieve its defined overall aim, the Thesis has five specific objectives:

- **Objective 1:** The improvement of the shape reconstruction approaches currently available in the literature, by providing a new methodology for three-dimensional curvature calculation;
- **Objective 2:** The identification of the parameters that influence the accuracy of the MCF shape sensor by means of a numerical and experimental study;
- **Objective 3:** The calibration of analytical predictive models relating the two parameters which mainly affect the accuracy of the three-dimensional curvature calculation (namely, curvature magnitude and bending direction angle), which may lead to design more performing MCF sensors;

- **Objective 4:** The design of an innovative experimental setup to assess the performance of MCF shape sensors and evaluate the effects of parameters that cannot be simulated, such as the strain sensors length;
- **Objective 5:** The development of a novel approach for shape reconstruction with twisting compensation using spun MCF.

1.5 Dissertation overview

This dissertation is structured in the following manner:

Chapter 1: Provides general background information and motivations and outlines research objective, chapter organization, research framework and recent scientific outcomes.

Chapter 2: Reviews of the current state of the art on shape sensing using optical multicore fiber and multi-fiber sensors, examining patents, experimental and theoretical researches, and illustrates an overview of the research background, including the fiber-optic curvature and shape sensors previously designed, the possible applications of these sensors and the their technical limits.

Chapter 3: Presents the methodology employed in this study for shape reconstruction using optical multicore fibers with inscribed FBGs. First, the procedure utilized to sense strain in the cores of a MCF, based on FBGs wavelength tracking, is discussed. Secondly, an innovative method for three-dimensional curvature sensing in MCFs through the calculation of the strain plane is proposed. Finally, the approach for 2D and 3D shape reconstruction, based on the numerical integration of the Frenet-Serret formulas, is illustrated.

Chapter 4: Investigates the effects of strain measurement and core position errors on the accuracy of MCF shape sensor in sensing bending direction and curvature, which are the inputs for shape reconstruction. In addition, the roles played by core spacing (distance between outer core and fiber axis), measured curvature and number of outer cores are identified. To conclude, a series of predictive models, which describe the mathematical relationship between the variables identified and the sensors accuracy are proposed.

Chapter 5: Focuses on the influence of the FBGs length on the accuracy of multicore fiber used to sense shape. A novel experimental setup for the performance assessment of MCF shape sensors is illustrated. Afterward, a comparison between the performances of the two MCF shape sensors based on short and long FBGs is drawn.

Chapter 6: Proposes and experimentally demonstrates a new approach, based on the Saint-Venant's Torsion Theory, for twisting sensing using optical spun multicore fiber with embedded strain sensors. Furthermore, a novel methodology for shape reconstruction, in presence of fiber twisting, is introduced.

Chapter 7: Summarizes the results and findings of the research and gives recommendations.

1.6 Research framework and recent scientific outcomes

This investigation was carried out within the ITN-FINESSE framework, funded by the European Union's Horizon 2020 Research and Innovation Program under the Marie Sklodowska-Curie Action Grant Agreement N° 722509 with a budget of 3,880,324.44 € [55]. FINESSE is a collaborative research and training network, gathering together 26 European universities, research centers and industrial partners with complementary expertise with the ultimate vision of a widespread implementation of distributed optical fiber sensor systems for a safer society.

The study of the mechanical behavior of multicore optical fiber used to sense strain, curvature, twisting and shape has required the synergic implementation of several disciplines: Solid Mechanics, Photonics, Statistics and Data Analysis. The aforementioned multidisciplinary research work has been possible thanks to the intense and efficacious cooperation between the Institutes of the Institute of Science and Technology of Concrete (ICITECH) and the Institute of Telecommunications and Multimedia Applications (iTEAM) - Photonics Research Labs (PRL) - of *Universitat Politècnica de València (UPV)*, in addition to valuable collaboration within the European ITN-FINESSE network.

Student exchanges and scientific events are of paramount importance for PhD students' growth, by simulating multidisciplinary skills, encourage networking and expanding their knowledge concerning specific topics. The subsections below list the secondments conducted, the scientific events attended, and the scientific outcomes of the research.

1.6.1 Secondments within the European ITN-FINESSE framework

1) Entity: Laboratory of Experimental Rock Mechanics (LEMR) – École Polytechnique Fédérale de Lausanne (EPFL), Lausanne, Switzerland;
   Period: September 2018;
   Objective: Feasibility Study of the monitoring of rock fracture due to earthquake using Optical Fiber Sensors.

2) Entity: CALSENS, Valencia, Spain;
   Period: November 2018/January 2019;
   Objective: Research on the monitoring of Steel Truss Bridges using Optical Fiber Sensors.

3) Entity: Department of Engineering – University of Cambridge (UCAM), Cambridge, United Kingdom;
   Period: September 2019/January 2020;

Objective: Research on the Tunnel Monitoring using Optical Multicore Fiber Shape Sensors.

1.6.2 Training events within the ITN-FINESSE framework

1) PhD School on Distributed Sensing Methods, Alcalá de Henares, Spain (September 2017);

2) PhD School on Speciality Fibres, Jena, Germany (April 2018);

3) PhD School on Entrepreneurship in Photonics, Leuven, Belgium (December 2018);

4) PhD School on Field Application and Standardisation, Cambridge, United Kingdom (September 2019).

1.6.3 Other training events

1) 7th International Summer School on Smart Materials & Structures, Trento, Italy (July 2018).

1.6.4 National Conferences attended

1) Spanish Optoelectronics Meeting (OPTOEL), Zaragoza, Spain (July 2019) with the following contribution:
"Measurement uncertainty of Seven-core Multicore Optical Shape Sensors".

1.6.5 International Conferences attended

1) 26th International Conference on Optical Fiber Sensors (OFS26), Lausanne, Switzerland (September 2018);

2) 7th European Workshop on Optical Fiber Sensors (EWOFS), Limassol, Cyprus (October 2019) with the following contributions:
"Temperature-insensitive 2D inclinometer based on pendulum-Assisted fiber Bragg gratings"
and
"Measurement uncertainty of 7-core multicore fiber shape sensors";

3) Asia Communications and Photonics Conference (ACP), Chengdu, China (November 2019) with the following contribution:
"Experimental study of the influence of FBG length on Optical Multicore Shape Sensors performance";

4) SPIE Photonics West 2020, San Francisco, USA (February 2020) with the following contribution:
"Twisting compensation of Optical Multicore Fiber Shape Sensors for Flexible Medical Instruments".

1.6.6 Peer-reviewed Journal Articles:

1) Floris I, Sales S, Calderón PA, Adam JM. Measurement uncertainty of multicore optical fiber sensors used to sense curvature and bending direction. Meas J Int Meas Confed 2019;132. doi:10.1016/j.measurement.2018.09.033.

2) Floris I, Calderón PA, Sales S, Adam JM. Effects of core position uncertainty on optical shape sensor accuracy. Meas J Int Meas Confed 2019;139. doi:10.1016/j.measurement.2019.03.031.

3) Floris I, Madrigal J, Sales S, Adam JM, Calderón PA. Experimental study of the influence of FBG length on optical shape sensor performance. Opt Lasers Eng 2020;126:105878. doi:10.1016/j.optlaseng.2019.105878.

4) Zheng D, Cai Z, Floris I, Madrigal J, Pan W, Zou X, et al. Temperature-insensitive optical tilt sensor based on a single eccentric-core fiber Bragg grating. Opt Lett n.d. doi:10.1364/OL.99.099999.

5) Floris I, Madrigal J, Sales S, Calderón PA, Adam JM. Twisting measurement and compensation of optical shape sensor based on spun multicore fiber. Mech Syst Signal Process 2020;140:106700. doi:10.1016/j.ymssp.2020.106700.

CHAPTER 2 STATE OF THE ART

2.1 Optical Fiber Sensors

In the past decades, optical multicore fiber shape sensing has attracted a great deal of attention among researchers and industries. This innovative technology has great potential for the structural health monitoring of civil structures and finds a number of industrial and medical applications that requires curvature, twisting and 2D/3D shape sensing, since it enables the determination of the three-dimensional position of any point on an optical fiber.

There are several alternative technologies available in the market capable of performing shape sensing:

- Shape sensing based on electrical sensors [15,56,57];
- Vibration-based shape sensing using accelerometers [26–28,58] ;
- Visual systems consisting of acquisition devices, computers, and processing software able to reconstruct shape using data collected by cameras [20,21] and radio detection and ranging (RADAR) [22–24];
- Electro-mechanical sensing systems which reconstruct shape by measuring angles with tilt sensors [44], such as inclinometers [59–62];
- Optoelectronic shape sensing [63,64].

Nevertheless, shape sensing becomes particularly critical in the applications that require- real-time and continuous tracking of a dynamic object and visual contact is obstructed. In addition, since the sensor must be attached to the object intended to be monitored, compact and small size, flexibility and embedding capability are also necessary in order to guarantee easy installation. In the light of the above, the implementation of optical multicore fiber shape sensors results extremely convenient thanks to the remarkable advantages of optical fiber technologies [13,16,65–70], comprising:

- Compactness, small size and lightweight;
- Flexibility;
- Monolithicity (no need of assembly, being manufactured as a single piece);
- Electrically passive operation;
- Resistance to harsh environments, including humidity, severe temperature, chemical and radiation;
- Immunity to Electromagnetic Interference (EMI);
- Corrosion resistance;
- Embedding capability;
- Multiplexing capability;

- Intrinsic safety (no electricity required in the sensor);
- High sensitivity and accuracy;
- Ability to sense a variety of measurands in continuous development, such as strain [40,41], temperature [36], moisture [42], vibrations [43], chemical agents [38], and many others [44].

Such advantages come from the extraordinary characteristic of silica (drawing glass), of which are made the large majority of optical fibers. Silica has high mechanical tensile and even flexural strength as well as high flexibility and almost perfect elastic behavior. Furthermore, silica is chemically stable and practically inert [71–74]. On the other hand, the process of optical fiber manufacturing, fiber drawing, developed to provide high speed and high performance in data transmission for communication applications, requires extremely high accuracy and specialization. A preform tip is heated, then the optical fiber is pulled out in an apparatus known as draw tower. Therefore, the exceptional characteristics of silica and the extremely advanced draw process guarantee to optical fibers sensor these unique properties. Finally, the multiplexing capability, which is the ability to multiplex a multitude of optical sensors on one single fiber and monitor them by a single remote interrogator unit, provides a notable advantage of this technology for the sensing application over the shape sensing alternatives.

2.2 Optical Multicore Fiber Shape Sensors

In this section, a review of the advancements in optical multicore fiber shape sensing and the possible applications of this technology are presented. The process of shape reconstruction using optical multicore fiber is articulated in several parts: strain sensing, curvature calculation and shape reconstruction. Optical fiber sensors are well recognized as highly sensitive strain and temperature sensors [16,75,76]. Table 2.1 summarizes the principal achievements regarding curvature and shape sensing, present in the literature.

Table 2.1. Historical progress in optical multicore fiber shape sensing.

Starting year	Contribution	Description	Refs.
1980s	Fiber Bragg Grating	Fiber Bragg Gratings, optical fiber reflectors that reflects particular wavelengths of light and transmits all other, were proved to be able to sense strain and temperature.	[75]
1980s	Multiplexing technique	The development of multiplexing techniques to interrogate several Bragg grating sensors on a common fiber path enabled quasi-distributed measurements of strain and temperature.	[77–79]

~ 1998	MCF-based interferometric bending sensor	The employment of optical multicore fiber enabled the measurement of degree and orientation of bending by comparing the strain in a pair of cores, using interferometric interrogation.	[80–83]
~ 2000	Bending sensor using FBGs	Curvature measurements were demonstrated by using fiber Bragg gratings. The gratings were written into separate cores of a multicore fiber and acted as independent, but isothermal, strain gauges, providing a temperature-independent measurement of the local curvature.	[47]
~ 2003	3D bend sensor	By employing three or more non-aligned strain sensors inscribed into the cores of an optical multicore fiber section, it was possible to measure the local three-dimensional curvature (curvature magnitude and bending direction).	[84–86]
~ 2004	2D and 3D shape sensor	Shape sensing was enabled by the development of approaches to reconstruct the shape of an optical multicore fiber with embedded FBGs, from the curvature sensed along the sensor, by aligning successive arc segments of fixed curvature.	[48,87,88]
~ 2007	Shape sensor using OFDR	Optical Frequency Domain Reflectometry (OFDR) technique permitted distributed shape sensing based on Rayleigh scattering using an optical multicore fiber.	[49,89]
~ 2012	Novel method for 3D shape sensing	An innovative method, based on the numerical resolution of a set of Frenet-Serret equations, was proposed to reconstruct complex three-dimensional fiber shapes as a continuous parametric solution, instead of sequence of arcs.	[50,90].
~ 2014	Twisted seven-core multicore fiber	Optical twisted seven-core multicore fibers for sensing applications were designed and manufactured to enable twisting compensation in shape sensing. The use of twisted MCF increases the sensitivity to twisting.	[91–94]
~ 2014	Continuous gratings in multicore fiber	An inscription apparatus and fabrication scheme that allow the continuous inscription of gratings over meters in all cores of multicore fiber through UV transparent coating were proposed. Continuous gratings increase signal to noise ratio and shape sensing precision if compared to the bare Rayleigh scattering of the optical fiber without gratings	[92]
~ 2016	Shape sensor using Brillouin scattering	Distributed shape sensing based on Brillouin scattering was performed using an optical multicore fiber and a Brillouin optical time-domain analyzer.	[95]
~ 2017	Force and shape sensor	A force and shape sensor for medical applications was developed using an optical multicore fiber with embedded FBGs. The presence of force feedback in medical instruments has been demonstrated to contain tissue damage.	[96]

2.2.1 Strain sensing

2.2.1.1 Fiber Bragg Grating

Fiber Bragg Gratings (FBG) are Bragg reflectors, well-established as highly sensitive strain and temperature single-point sensors (quasi-distributed sensing) [16,75]. FBGs are the most widely used optical fiber sensors and have a multitude of engineering applications [97–104]. Furthermore, they are the most appropriate OFSs for dynamic sensing, since reach high frequency data acquisition (~ kHz).

FBGs are constructed by laterally exposing the core of an optical fiber to an intense laser light with periodic pattern. The exposure generates a permanent increment of the refractive index of the core. This fixed index modulation is a grating and has a period that depends on the exposure pattern. A fiber Bragg grating allows the transmission of some wavelengths and reflects others, corresponding to the FBG wavelength peak, which is related to its period. Since the period of a grating varies with temperature and longitudinal strain, it is possible to sense these quantities by tracking the grating wavelength peak.

2.2.1.2 Distributed sensing

Light scattering is a phenomenon caused by the interaction between the atoms or molecules of a medium and the incident electromagnetic (EM) waves that pass through it and consists in light absorption of energy and its re-emission in different directions and with various intensity. Light scatters through three different processes: Raman (sensitive to temperature), Brillouin (sensitive to both temperature and strain), and Rayleigh (sensitive to strain). Only Rayleigh and Brillouin scattering are utilizable to sense the strain of the medium. In the 80s, such loss in propagation was first exploited for the development of distributed sensing configurations using optical fibers. The idea of distributed sensing consists in a sensing element with linear geometry and in a sensing system able to measure the value of the measurand considered, e. g. strain, at any position along the sensing element. The performances of Distributed Optical Fiber Sensors (DOFS) are evaluated by three characteristics that are generally interdependent: the accuracy on the measured quantity, the sensing length or sensing range (range for the position) and the spatial resolution (minimum distance to measure variations in the measurand along the optical fiber equivalent to the gauge length of a discrete sensor). Compared with FBGs, distributed sensors have significantly lower frequency data acquisition, which depends on the technology and on the sensing range (an indicative value could be ~ mHz / Hz). DOFSs have been comprehensively reviewed in the literature [76,105–108].

2.2.1.3 Distributed Sensors based on Rayleigh scattering

DOFSs based on Rayleigh scattering are usually classified into two categories: Optical Time Domain Reflectometry (OTDR) and Optical Frequency Domain Reflectometry (OFDR).

An OTDR launches laser light pulse into an optical fiber. The returning light, Rayleigh backscattered light, is collected and is fed into the receiver where its optical power is measured as a function of time (attenuation in the time domain). The evolution of the power over time of the detected signal provides information of position and magnitude of the quantity to be measured distributedly along the fiber length [109]. The efficiency of OTDR is very limited when high spatial resolution (less than one meter) is required, while the common sensing range is around 1/10 km [76,105,108].

OFDR systems have attracted the interest of many researchers driven by the necessity of short spatial resolutions (millimeter scale) and cost effective distributed optical fiber sensors. On the other hand, the sensing range of this technique results to be notably less than OTDR and, commonly, in the range of 10/35m [76,105,108]. OFDR operates in the frequency domain (or Fourier domain). OFDR sensor system tunes a frequency range and receives a frequency response of the optical fiber, which is converted into the time/spatial domain by Fourier transform.

Optical frequency domain reflectometry exists in two variants: Incoherent OFDR (I-OFDR) and Coherent OFDR. The main difference is that in I-OFDR the source is not pulsed, but generates CW light by modulating the optical intensity with radio frequency (RF) signals. While in the case of Coherent OFDR, the source is obtained by sweeping the optical frequency [109].

OFDR Rayleigh sensing can be performed simply by utilizing the inherent Rayleigh scattering from the core of the fiber. Otherwise, in order to increase the sensitivity in distributed strain sensing, the Rayleigh signal strength can be enhanced by exposing the optical fiber to ultraviolet (UV) laser [110] or inscribing continuous grating into the cores of the fiber [91,111].

2.2.1.4 Distributed Sensors based on Brillouin scattering

The most significant distributed optical fiber sensing techniques based on Brillouin scattering are: Brillouin Optical Time Domain Reflectometry (BOTDR) and Brillouin Optical Time Domain Analysis (BOTDA).

BOTDR refers to the time domain interrogation of back-propagating spontaneous Brillouin scattering. The concept is analogous to the OTDR relied on Rayleigh backscattering, but, in this case, the spatial resolution is in the range of 1 meter/tens of meters and the sensing range is up to tens of kilometers [76,105,112].

BOTDA has a more elaborated form than BOTDR and is based on Stimulated Brillouin Scattering (SBS). BOTDA technique consists in the launch, from both the extremities of optical fiber, of an intense pulse and Continuous Wave (CW) light with a frequency difference equivalent to the Brillouin frequency shift [105,113]. The intense pump pulse interacts locally during its propagation with the weak CW probe and the gain obtained by the probe at each location along the fiber length can

be determined by analyzing the probe amplitude in the time domain. This stimulated scattering process produces a more intense Brillouin scattering that requires less averaging to achieve a reasonable Signal to Noise Ratio (SNR) of the system.

2.2.2 Curvature sensing

Curvature calculation is the preliminary step for shape reconstruction. The first achievements in curvature sensing (also called bending sensing) were reached in the 1990s. Greenaway et al. filed a patent (International Patent and US Patent in 1998) describing an optical fiber bending sensor based on MCF able to measure the degree and orientation of the bending present in the sensor length [80,81]. In 1999, Blanchard et al. described a novel three-core photonic crystal fiber and demonstrated its ability to measure bending in two dimensions using interferometric interrogation at a single wavelength [82]. Gander et al. (2000) first demonstrated curvature measurements by using Bragg grating inscribed in multicore fiber [47]. Flockhart et al. in 2003 first demonstrated the use of fiber Bragg gratings written into three separate cores of a multicore fiber for two-axis curvature measurement [84]. Clements filed a patent (2003) illustrating a flexible "Smart cable" able to measure the local curvature and torsion along its length [86]. In 2004 MacPherson at al. first reported on the use of a 4-core multicore fiber incorporating FBG strain sensors in each core as a fiber optic pitch and roll sensor [85].

In addition to strain and curvature sensing by using optical fiber sensor technology, the attention of researchers concentrated on the development of multiplexing techniques [77], in order to perform quasi-distributed measurements. One of the first examples of this method was proposed by Kersey and Morey, in 1993. A technique for the detection of wavelength shifts in wavelength-encoded fiber Bragg grating sensors was proved capable of interrogating several Bragg grating sensors on a common fiber path, using a mode-locked laser principle [78].

With the advent of multiplexing capabilities, finally, quasi-distributed sensing was performed. Chen and Sirkis filed a patent (1998) describing a fiber optic system able to produce a plurality of strain measurements along one fiber path for determining the shape of a flexible body, by using Bragg grating sensor technology and time, spatial, and wavelength division multiplexing [79]. Barrera et al. developed a multipoint and two-dimensional curvature optical fiber sensor based on a non-twisted homogeneous four-core fiber, using Wavelength Division Multiplexing (WDM) [114]. A novel experimental setup was developed, shown in Fig. 2.1, and an array of 15 FBGs was fabricated and tested by sensing constant curvatures. The sensor resulted able to sense curvature with high accuracy, obtaining a standard deviation under 1.6% in the applied curvature range.

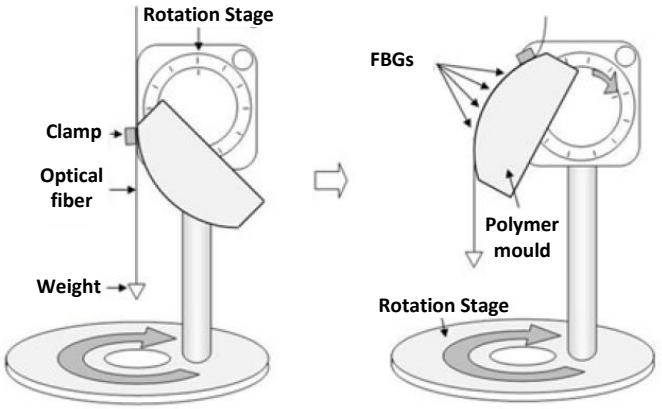

Fig. 2.1. Characterization setup for the measurement of uniform curvatures [114].

Furthermore, alternative technologies to fiber Bragg grating were employed to perform optical fiber curvature sensing. Barrera et al. developed a directional curvature sensor based on long period gratings inscribed in a multicore optical 7-core multicore fiber [115].

2.2.3 Shape sensing

When the ability of optical multicore fiber to sense curvature was widely recognized, research efforts focused on the shape reconstruction. In 2004, Miller et al. proposed an approach to reconstruct the two-dimensional shape of an optical multicore fiber with embedded FBGs based on the local curvature estimated from distributed strain measurements [48]. The shape algorithm estimated the local shape utilizing osculating (or tangential) circles of curvature equal to the curvature measured. Finally, the fiber shape could be reconstructed as a sequence of arc segments separated by the grating spacing. Lunwei et al. (2004) developed a sensor device comprising a plurality of FBG sensors mounted on the body of a flexible wire and able to sense shape in real-time [87]. The curvature was calculated from the strain measured in the FBGs and interpolated between the sensor nodes. Then, the shape was reconstructed as sequence of arc segments with different curvature. In 2007, Duncan et al. measured shape and position of an optical multicore fiber under a variety of circumstances using two sensing techniques, fiber Bragg gratings and Rayleigh backscatter, and drew a comparison between the results of the measurements [49]. In 2008, Froggatt and Duncan filed a patent describing a fiber optic position and/or shape sensor based on Rayleigh scatter and optical multicore fiber [89].

Theretofore, research and development efforts mainly centered on two-dimensional shape sensing, while the performance of MCF-based three-dimensional shape sensors were unsatisfactory. A significant improvement was then brought by Moore and Rogge, who developed, in 2012, an innovative approach for the three-

dimensional fiber shape reconstruction, based on the numerical resolution of a set of Frenet-Serret equations [50,90]. The method offers remarkable advantages over prior approaches, determining complex three-dimensional as a continuous parametric solution rather than an integrated series of discrete planar bends. Employing the aforementioned approach Zhao et al. (2016) first utilized Brillouin scattering to perform distributed shape sensing based on 7-core multicore fibers [95].

The approach presented in [50] is valid in all the conditions that avoid the external twisting. Otherwise, the fiber twisting generates significant errors in shape sensing [116]. The effects of the external twisting were first studied by Askins et al., who proposed, in 2008, a method for estimating the twisting of an optical fiber from internal strain state and designed a large-scale model of a tether fiber, 100X, to study this phenomenon [117]. A solution to finally overcome the effects of twisting was first designed by Westbrook et al. of OFS Labs. (2014), who manufactured an optical twisted seven-core multicore fiber for sensing applications, illustrated in Fig. 2.2, with fiber Bragg gratings inscribed along its length and with a twist of 50 turns per meter to increase the twisting sensitivity [91,92]. The optical multicore fiber could be interrogated using two different types of sensing signals: the FBGs inscribed into the optical fiber cores (enhanced signal) or the light scattering from the inherent Rayleigh scattering of the fiber cores. In this way, the fiber twisting could be calculated as a difference between the state of strain of outer and central cores, even if no experiment was performed to investigate the accuracy in twisting sensing. One year later, Cooper et al. of Fibercore designed and fabricated an optical spun (or twisted) multicore fiber for communications and sensing applications with a spin pitch of 15.4 mm (64.9 turn/m) [93,94].

With its consolidation, based-MCF shape sensing has found application in several fields and many instruments relied on this technology have been developed. Chan and Parker filed a patent in 2015 describing a method for rendering the shape of a multi-core optical fiber or multi-fiber bundle in three-dimensional space and in real time based on measured fiber strain data [118]. Khan et al. developed (2019) a shape sensor based on optical multicore fiber with fiber Bragg gratings to sense the shape of flexible medical instruments, such as catheters and endoscopes (see Fig. 2.3) [52].

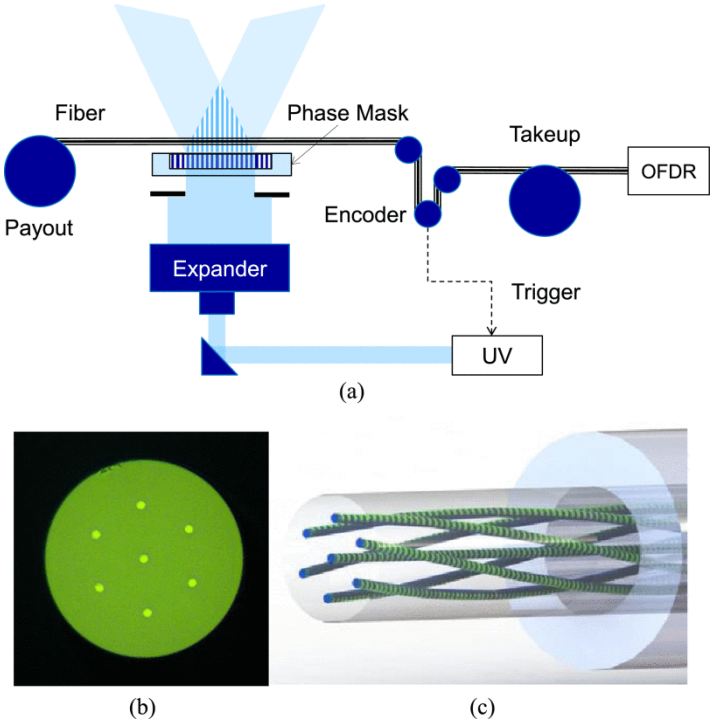

Fig. 2.2. (a) Array inscription apparatus for continuous fabrication of gratings in all cores through UV transparent coating. (b) Cross-section of an optical seven core fiber with coating removed. (c) Twisted multicore fiber schematic [92].

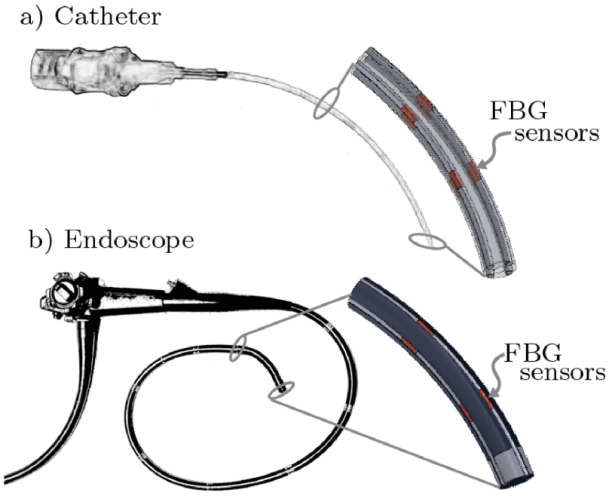

Fig. 2.3. Example of applications of optical multicore fiber shape sensors in numerous flexible medical instruments: (a) Catheter (b) Endoscope [52].

2.3 Applications

When optical fiber shape sensing became a mature technology, the attention of scientists and engineers was directed to its possible applications, thanks to its advantages compared to existing methods. This section revises the current state of the art on applications that require shape sensing, with particular emphasis on the research works in which optical fiber shape sensing was utilized.

2.3.1 Civil engineering

2.3.1.1 Geotechnical monitoring

Landslides and slope movements are a significant hazard that can result in many fatalities and much property loss [119,120]. Geotechnical monitoring consists in continuous measurements and real-time analysis of the main geotechnical and environmental parameters in order to detect anomalous behavior in the initial phases and promptly intervene. Geotechnical inclinometers are used to determine the shape of ground movements, including the following data: direction, magnitude, rate and depth [61]. Such information is of essential importance to understand the behavior of landslides and slope movements and to develop intervention strategies [121]. Thanks to the resistance to corrosion, the capability of sensing shape with no visual contact and the ability to perform continuous and real-time monitoring, optical fiber shape sensors are particularly fit for the purpose.

For these reasons, a lot of research has been concentrated on the development of optical fiber inclinometer. Some authors have exploited the potentialities of MCFs to develop monolithic inclinometers [122,123]. In addition, an extensive research has been focused on the design of distributed optical multi-fiber inclinometers for ground movement monitoring, obtained by fastening several optical fibers with embedded strain sensors on a tube, as shown in Fig. 2.4 [124–128]. These sensors are essentially cantilever beams with one end fixed. While the sections geometry are the same as optical multicore fibers (three-core or four-core geometry), but these solutions offer a notably greater core spacing, distance between the sensor axis and the outer cores, compared with standard multicore fibers (differs by orders of magnitude) in order to achieve better accuracy in curvature sensing. On the other hand, the extremely advanced draw process of optical multicore fibers guarantees remarkable more compactness, higher manufacturing accuracy and the smaller core spacing ensures minimal temperature gradients.

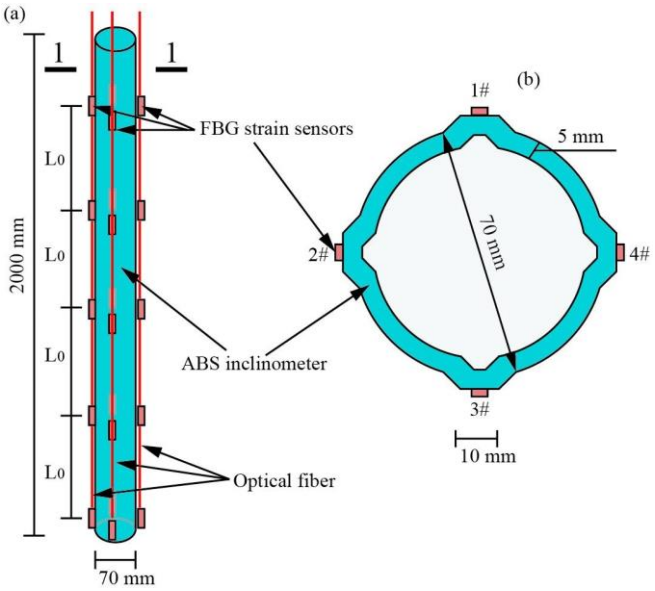

Fig. 2.4. (a) Schematic diagram of FBG-based inclinometer; (b) Cross-section. [125]

2.3.1.2 Structural health monitoring of civil infrastructures

Structural health monitoring systems provide information about the performance and conditions of structures and infrastructures through the observation of their in-service behaviors [13]. For this purpose, optical MCF shape sensing can offer an efficient nondestructive method for the direct, continuous and real-time monitoring of the global behavior of civil infrastructures.

MacPherson et al. first proposed an application in tunnel health monitoring of multiplexed fiber Bragg grating strain sensors based on multicore fiber [129]. A sensor, consisting in a series of gratings, inscribed into the cores of an optical four-core fiber, and able to measure curvature along its length, was configured to monitor displacement between the segments of a concrete tunnel section and was proved to reach a resolution of ±0.1 mm.

To the best knowledge of the author, optical fiber shape sensor has not been employed in bridge health monitoring [19,130,131]. Nevertheless, the approaches based on optical multicore fiber for direct shape sensing have great potentialities in this field. By way of example, Kissinger et al. designed a dynamic fiber-optic shape sensor based on multiplexed Bragg gratings inscriber in 4 fibers attached to a flexible support, which can be employed to study the response of bridges under dynamic loads [132]. The sensor was tested using a cantilever test object and resulted able to measure structural displacements and vibrations over an interferometric bandwidth of 21 kHz. In addition, it has been demonstrated that the deflection of a bridge span under designed loads, an important parameter for bridge safety evaluation, can be

efficiently measured by using inclinometers, with consideration similar as those made above for geotechnical inclinometers [62].

Another potential application of optical multicore fiber shape sensors is the monitoring of the verticality and the deformed shape of buildings, bridge piles, and towers [133]. Bang et al. developed a sensor composed by an array of multiplexed FBGs for the measurement of strain and bending deflection of an 1.5 MW wind turbine tower, as illustrated in Fig. 2.5 [134]. With the aim of monitoring the dynamic structural behavior of the wind turbine, 10 FBG sensors were arrayed and installed on the inner surface of the tower located at the primary wind direction. A similar analysis can be performed by using an optical multicore fiber shape sensor with the significant advantages of determining the three-dimensional deformed shape of the tower with a single MCF array and easier installation.

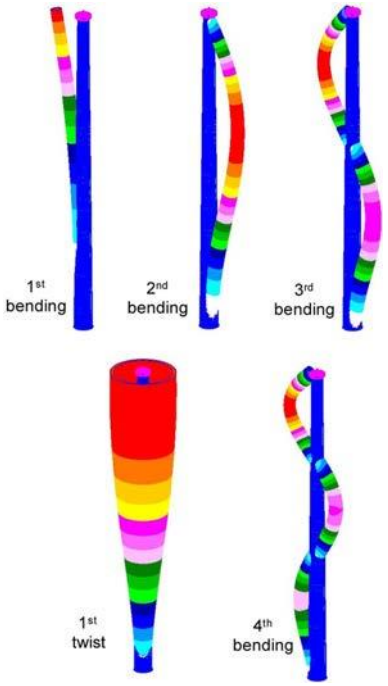

Fig. 2.5. Mode shapes of the wind turbine tower [134].

Finally, thanks to their resistance to high-energy ionizing environments, as demonstrated in [54], optical multicore fiber shape sensor are particularly suitable for the structural health monitoring of nuclear central and spent nuclear fuel repository, which is of vitally importance considering that radiations can be extremely hazardous to humans or to the environment.

2.3.2 Industrial and aerospace engineering

The reconstruction of the displacement field of a structure is a fundamental capability for the structural health monitoring of critical components. One of the common problems in aerospace engineering is the determination of the shape of a wing from strain measurements. The most widely used approaches to achieve this goal are: the inverse Finite Element Method, the Modal Method and Ko's Displacement Theory, comprehensively reviewed in [135]. The three methods require heavy computational cost in addition to the use of a considerable number of strain sensors. Optical fiber strain sensors have disrupted the sector and brought remarkable improvements, thanks to the their advantages compared with tradition electrical sensors, such as high frequency data acquisition, low cost, small size, lightweight, anti-electromagnetic interference, multiplexing ability and the capability of adapting to complex environment [102,136,137]. Nonetheless, optical multicore fiber can bring even more significant enhancements, offering an alternative to traditional method and allowing the shape to be measured directly and dynamically with no necessity of developing a computational model. In 2006, Klute et al. of Luna Innovations developed a new technology, which enables the distributed and axially co-located differential strain measurements based on optical multicore fiber and OFDR. This approach generates complex shape data, as shown in the picture below, of Variable Geometry Chevron (VGC), which is a (NiTinol) actuators-based morphing system, flight tested by Boeing shortly before [116].

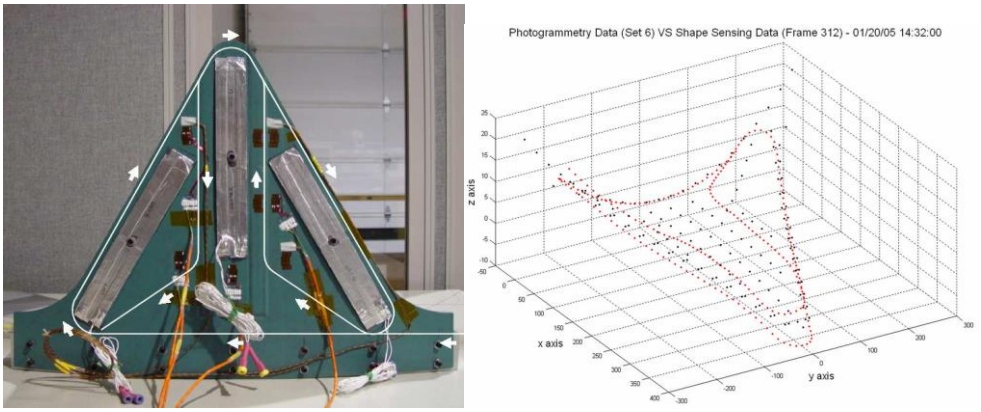

Fig. 2.6. Fiber-optic shape sensing on a morphing chevron: (a) **S**hape multicore tether routing configuration; (b) Photogrammetry (black) vs. Shape Sensing (red) Data Points [116].

2.3.3 Medical applications

2.3.3.1 Surgical instruments

For the correct manipulation of medical instruments inside the patient body, it is essential to dynamically track their position and shape during a surgical procedure,

as it has been deeply analyzed in [138]. Therefore, optical multicore fiber and multi-fiber shape sensing has enormous potentialities in the medical field and has been implemented in needles, catheters, endoscopes and continuum robots for a multitude of clinical applications, including colonoscopy [52], epidural administration (see Fig. 2.7) [139], endovascular navigation [140], cardiac and ophthalmic procedures [141], minimally invasive surgery [51,142] and biopsy [52,141].

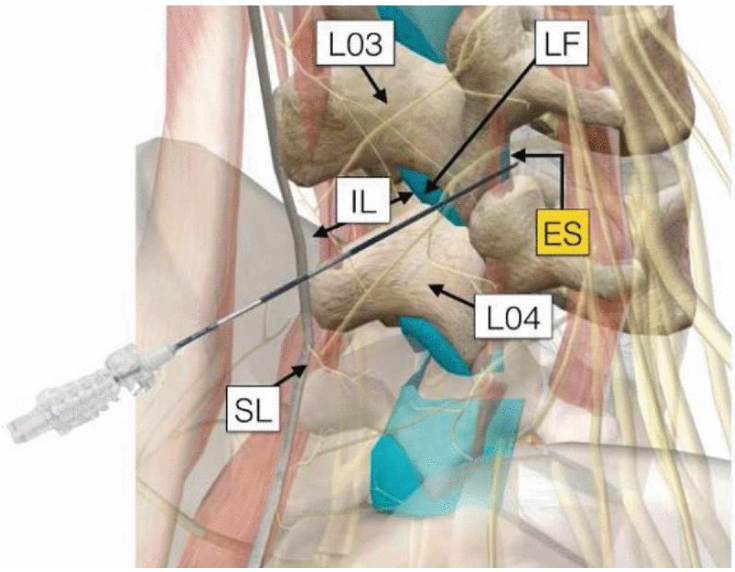

Fig. 2.7. Fiber-optic based needle for real-time guidance in epidural anesthesia [139].

Traditional approaches used nowadays to track position and shape of medical instruments have some limitations. External imaging devices based on fluoroscopy or ultrasound enable the position and the shape of medical devises to be determined. Regrettably, such techniques have several disadvantages, comprising bulkiness, high cost, exposure to radiations and low-speed data acquisition. Alternatively, when employing needles and catheters, doctors can identify the instrument location relying on the resistance felt through it, which is a subjective evaluation criterion. Optical multicore fiber and multi-fiber shape sensors embedded in medical instruments provide a valid alternative to these traditional methods, relying on the competitive advantages of optical fiber sensors technology, such as flexibility, compactness, lightweight and intrinsic safety.

Lunwei et al. (2004) developed a FBG-based shape sensor for intelligent colonoscopy composed of a flexible wire with attached optical fibers [87]. Experiments were performed in the colon of a live swine. The FBGs sensors captured the deformation of the sensor wire and enabled the shape of the colonoscope to be reconstructed. Roesthuis et al. (2014) designed a prototype of a flexible nitinol needle with embedded an array of 12 FBGs sensors, able to measure the axial strain

and curvature and to reconstruct the 3D needle shape from the curvature [143]. The maximum errors between the experiments and the results obtained from beam theory-based model were 0.20 mm (in-plane deflection with single bending), 0.51 mm (in-plane deflection with double bending), and 1.66 mm (out-of-plane). Moon et al. in 2014 developed a highly flexible, thin optical shape sensor to be integrated into minimally invasive surgery systems [51]. The sensor was fabricated by arranging and epoxy molding three optical fibers with inscribed FBGs in a triangular shape and had a length of 115 mm and a diameter of 870 μm, ensuring high-bending operation up to 90°. Real-time shape monitoring was performed with a sampling rate of 3.74 Hz and the average tip position error resulted to be 1.50% of the total sensor length.

The detection of force in medical instruments has been demonstrated to support the containment tissue damage. Khan et al. designed, in 2017, a force and shape sensor able to estimate simultaneously the shape of medical devices and the interaction forces between the instrument and the surrounding environment [144]. The sensor consisted in three single optical fiber with embedded FGSs with the same geometrical configuration as optical multicore 3-core fiber. Khan et al. proposed (2019) a technique to the reconstruct the shape of a flexible instrument in 3D Euclidean space based on data from Fiber Bragg Gratings inscribed in multicore fibers [52].

Nowadays, endovascular aortic repair procedures are generally conducted relying on two-dimensional fluoroscopy imaging, which exposes patients to X-rays. Optical multicore fiber shape sensing offers an alternative to this method, containing the risks for patients. Jäckle et al. (2019) developed an optical MCF shape sensors for endovascular navigation using an optical multicore fiber with inscribed a set of FBGs. The sensor was obtained employing 3 cores of a multicore 7-core fiber and was able to sense curvature and shape from the strain sensed by the FBGs [140]. Furthermore, an optimized shape sensing model to enhance the sensor accuracy was developed and enabled shape reconstruction with an average error of 0.35–1.15 mm and maximal error of 0.75–7.53 mm over the whole 38 cm sensing length.

2.3.3.2 Posture monitoring

Another possible application of optical MCF shape sensing in medical field is the detection of spinal posture changes, although, to the best of the author's knowledge, such subject has not been investigated yet. Plamondon et al., in 2006, conducted an experimental study to evaluate a hybrid system composed of two inertial sensors for the three-dimensional measurement of trunk posture, as illustrated in Fig. 2.8 [63]. Wong and Wong (2007) proposed a method for monitoring postural changes in sitting using 3 tri-axial accelerometers [58]. Artem et al. (2015) developed a tape sensor, composed of interconnected and programmable sensor nodes on a flexible electronics substrate and proposed its employment as wearable posture monitoring device using a deformation sensing algorithm [64]. Compared with these existing

methods, shape sensing based on optical multicore fiber has several advantages, particularly convenient in this application scenario: compactness, flexibility, lightweight, high sensitivity and accuracy, high frequency data acquisition and embedding and multiplexing capability.

Fig. 2.8. Experimental setup of the hybrid system for three-dimensional trunk posture measurement: (a) static validation; (b) short dynamic validation; (c) long dynamic validation [63].

2.4 Technical limits and sources of errors

Several experimental studies investigated the accuracy of optical multicore fiber and optical multiple single-core fiber. To the author's best knowledge, it was found that the average accuracy of these sensors in sensing shape and position is ~1 mm [52,140,142,145–149] and the highest accuracy reached was ~ 0.3 mm [150]. Regrettably, it is not possible to draw a comparison among the vast multitude of optical-fiber-based shape sensors reported in the literature, since their accuracy in shape sensing was not assessed in standardized conditions. In particularly, in each experiment, the sensor length and the complexity of the shape measured, parameters which greatly influence the sensor performance, were highly variable.

Moreover, the research studies that have investigated the source of errors, which influence performance of these sensors are extremely limited. The most significant are here examined.

Jäckle et al. introduced an innovative approach for curvature interpolation implementable to enhance the accuracy of shape reconstruction algorithms [151]. Ordinarily, strain sensors are uniformly distributed, with a constant center-to-center distance, along the length of a shape sensor. The missing curvatures, in the portion of the shape sensor where there are no strain sensors, are determined by interpolation. Curvature interpolation is one source of errors for shape sensing, particularly relevant when quasi-distributed strain sensors are employed, such as FBGs (the more the distance between the strain sensor is, the more significant the impact of curvature interpolation is). In the aforementioned study, an averaged cubic approach was proposed to interpolate the curvature between FBGs sensor, while sensing the shape of an arc and an s-curve. The method presented was demonstrated to be more efficient than the cubic and nearest neighbor interpolation approaches. However, it should be taken into consideration that the efficiency of curvature interpolation approaches can depend on the measured shape.

Henken et al. performed an error analysis to quantify the accuracy of FBG-based shape sensors with three-core configuration and to assess the suitability of this method for robotic medical needle steering [152]. Several parameters were considered in the simulations: measured wavelength inaccuracy; photoelastic coefficient; sensor geometry inaccuracies (errors in core spacing - distance between outer cores and central axis - and angular spacing); and the measured curvature inaccuracies that propagates on the shape reconstruction. It was found that the accuracy of FBG-based shape sensing implemented in a needle can be in the order of 10% of the deflection at the tip, depending on the configuration. Nevertheless, when tip deflection is smaller than approximately 1 mm, it cannot be detected accurately. This approach presents several limitations:

- Inaccuracies in measured wavelength of 6 and 4 pm, correspond to the resolutions of the interrogators, were added to the FBG wavelength for the needle and triplet, respectively. These inaccuracies should have a Gaussian distribution to represent the real strain measurement errors;
- The inaccuracy of photoelastic coefficient and sensor geometry were simulated setting to a value each of the variables of interest randomly selected from a uniform distribution with a range that is stepwise enlarged from 0 to 0.04 for photoelastic coefficient, from 0 to 0.04 mm for core spacing, from 0 to 4° or 40° for angular spacing for needle or triplet, respectively. To define a uniform distribution of the inputs it should have been considered a mean value and a standard deviation instead of a range.
- No test was performed to verify that the sample records chosen was statistically significant;
- It is difficult to predict the combined effect of the inaccuracies and no predictive model was developed;
- The outcomes of the simulations are not a set of distributions;

- The propagation of the errors in curvature sensing to shape reconstruction were simulated using the equation of the beam elastic line based on the Euler–Bernoulli beam theory. Such approach is valid only for two-dimensional shape sensing and it only covers the case of small deflections of a beam, subjected to lateral loads. These hypotheses are, oftentimes, not satisfied in the problem considered.

Another significant source of errors is the sensors twisting, as demonstrated in several studies [116,148,152], although most of the approaches for shape sensing neglects it [50,132,144,150]. Askins et al. first studied this phenomenon, by manufacturing a large-scale model of a tether fiber, 100X [91]. Nevertheless, an experimental study that investigates the effects of twisting in optical multicore fiber shape sensors is still missing.

In the light of the above, notwithstanding the vast research efforts focused on this subject, an exhaustive study on the parameters that affect the performance of optical multicore fiber shape sensors has not been conducted yet. In consequence, this research work will particularly concentrate on this aspect.

CHAPTER 3 SHAPE RECONSTRUCTION

3.1 Introduction

When an optical multicore fiber sensor is fastened only at one extremity and the constraints are frictionless, the natural frame of the curve coincides with the material sensor frame [153]. This Chapter describes the process for shape reconstruction (the reconstruction of the sensor frame) employed in this study by using optical multicore fiber shape sensors with embedded strain sensors.

A novel approach, based on the strain plane calculation, was developed to determine the three-dimensional curvature in each instrumented section of the sensor from the values of strain sensed in the cores and improve the methods of shape reconstruction available in the literature. Next, the shape of the fiber can be reconstructed by numerical integration of the 3D curvature along its length. In this research work, it was used the approach proposed by Moore and Rogge. based on numerical integration of the Frenet-Serret equations [50].

The flowchart of the whole shape reconstruction process is shown in the figure below.

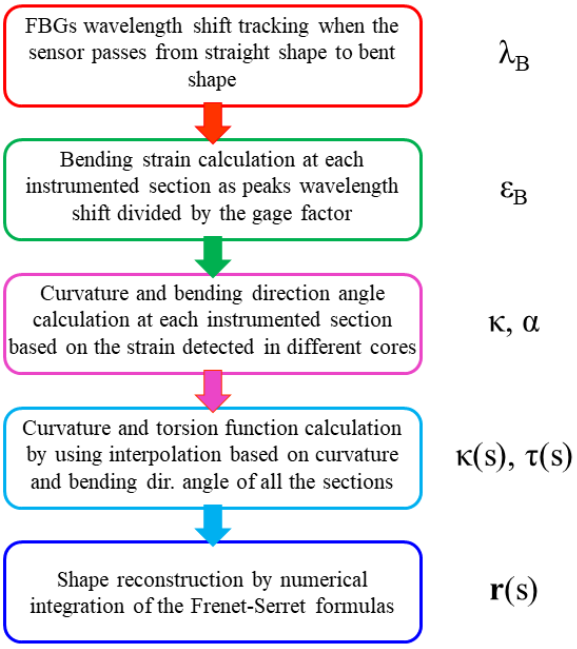

Fig. 3.1. Flowchart of shape reconstruction process.

It is worth noticing that, although in this research the strain in the cores was only sensed by employing Fiber Bragg Gratings sensors and tracking their peaks wavelength, the same methodology is still valid, with regard to three-dimensional curvature and shape sensing, when the strain is sensed by means of different sensing technique, such as Rayleigh or Brillouin scattering.

3.2 Strain sensing using Fiber Bragg Gratings

The engineering strain (or engineering extensional strain, longitudinal strain or nominal strain) is expressed as the ratio between the length variation and the initial undeformed length of an object measured along a reference axis. The strain is defined as tensile and positive, if there is an elongation, while it is compressive or negative, when the object shortens. The strain unit, ε, is a dimensionless value and can be calculated by:

$$\varepsilon = \frac{L_f - L_i}{L_i} = \frac{\Delta L}{L_i} \tag{3.1}$$

Where L_f, L_f and ΔL are, respectively, the initial length, the final length and the length variation of the object considered.

Fiber Bragg Gratings (FBG) are a type of distributed Bragg reflector, well-established as highly sensitive strain and temperature sensors [16], since they were first proposed in the late 1980s [75]. FBG sensors have many engineering applications [97–104], thanks to their advantages over electric sensors, including: intrinsic safety, multiplexing capabilities, immunity to electromagnetic interference (EMI), resistance to radiation, chemicals and harsh temperatures, lightweight and compactness.

FBGs are constructed in a short segment of optical fiber by laterally exposing a core to a periodic pattern of intense laser light. As a results, periodically modulates light refractive index is generated in the core [97]. The light propagates through the core with negligible attenuation or signal variation, except for those wavelengths that satisfy the Bragg condition, which are affected and, consequently, strongly back-reflected, as shown Fig. 3.2. The sensing capability of FBGs comes from variation of the grating period under thermal or tension expansion [104]. The Bragg wavelength, which is the reflected wavelength, λ_B, is defined by the relationship:

$$\lambda_B = 2n_{eff}\Lambda \tag{3.2}$$

where, n_{eff}, is the effective refractive index of the grating in the fiber core, also called modal index, and Λ is the grating period. n_{eff} quantifies the velocity of light propagation as compared to its velocity in vacuum and depends either on the mode in which the light propagates (for multimode waveguides) or on the wavelength.

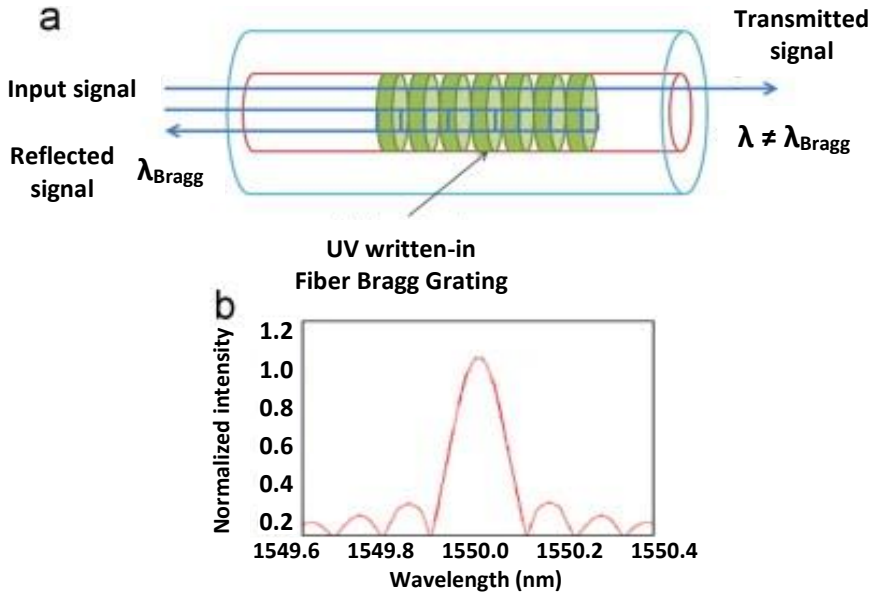

Fig. 3.2. Fiber Bragg grating operation principle [41]; (a) Schematic of FBG signal reflection; (b) FBG typical spectrum.

The Bragg wavelength varies with the change of Λ that in turn changes with expansion induced by temperature variations and with tension induced by strain. The general equations to express the strain–temperature relationship for the FBG strain sensor are the following:

$$\frac{\Delta\lambda_1}{\lambda_1} = \frac{\Delta\lambda_\varepsilon}{\lambda} + \frac{\Delta\lambda_T}{\lambda} = (1 - P_e)\varepsilon + (\alpha_T + \zeta)\Delta T \tag{3.3}$$

where P_e, α_T, ζ and ΔT are, respectively, the optical elasticity coefficient, the thermal expansion coefficient, the thermal-optics coefficient and temperature variation, while, λ_1 is the Bragg wavelength of the FBG that experiences both temperature and strain variations. The equation that describes the FBG wavelength shift due to temperature variations is:

$$\frac{\Delta\lambda_2}{\lambda_2} = \frac{\Delta\lambda_T}{\lambda} = (\alpha_T + \varsigma)\Delta T \tag{3.4}$$

in which λ_2 is the Bragg wavelength of a grating experiencing only temperature variation.
Therefore, the strain can be calculated combing the previous equations:

$$\varepsilon = \frac{\left(\frac{\Delta\lambda_1}{\lambda_1} - \frac{\Delta\lambda_2}{\lambda_2}\right)}{(1 - P_e)} \tag{3.5}$$

3.3 3D curvature calculation through strain plane determination

In order to calculate the shape of the fiber, the multi-dimensional curvature must be determined along the sensor length. To do so, the employment of optical multicore fiber (MCF) is particularly convenient. In fact, MCFs are monolithic and compact cables, which, thanks to the multiple cores (see Fig. 3.3) allow strain sensing in several points of each instrumented section (section with embedded strain sensors). Hence, the three-dimensional curvature can be calculated from the values of strain.

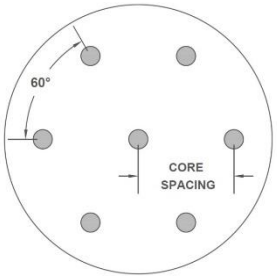

Fig. 3.3. Optical Multicore seven-core fiber cross-section.

In order to simplify the problem and enable the calculation of the curvature from a limited number of points of measurement in each section, it is necessary to make a series of assumptions, known as assumptions of the Euler-Bernoulli beam theory [154]:

- The cross-section is infinitely rigid in its own plane (the cross sections remain plane);
- The cross-section of a beam remains plane after deformation;
- The cross-section remains normal to the deformed axis of the beam (the cross sections remain normal to the centerline);
- The bending does not produce the elongation of the beam centerline [155].

Furthermore, it is supposed that the errors made by approximating with a constant value the strain along the length where it is sensed (the length of the FBG for quasi-distributed sensors or the spatial resolution for distributed strain sensors) are negligible.

In addition, in most cases when dealing with MCF shape sensors, it is also possible to hypothesize that along the entire section the temperature is constant (there are no temperature gradients inside the section), considered the small core spacing (distance between the outer cores and the fiber axis), so that no temperature compensation is necessary. Obviously, the correctness of this hypothesis should be ascertained for optical shape sensors with large radius.

For instance, considering a dual-core fiber (gratings at the same temperature), under the assumption made, bending induces difference in the strain between the gratings in proportion to the distance from the neural axis, as shown in Fig. 3.4.

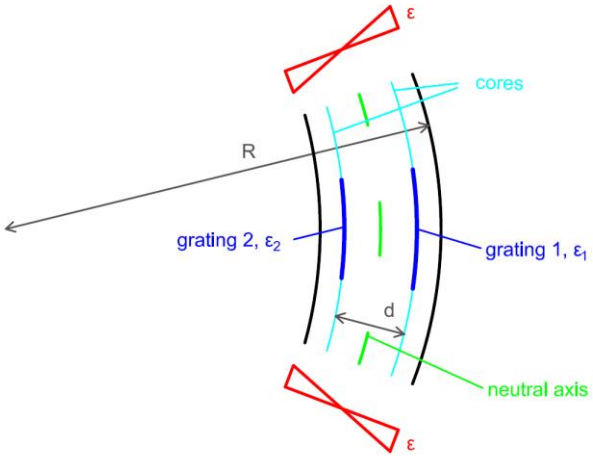

Fig. 3.4. Multi-core fiber with two gratings for curvature sensing.

By comparing pairs of gratings, it is possible to calculate the magnitude of curvature using the following equation:

$$\kappa = \Delta\varepsilon/d = (\varepsilon_1 - \varepsilon_2)/d = 1/R \tag{3.6}$$

where κ is the curvature, ε_1 and ε_2 are the strains detected by the two FBGs, d is the distance between the cores and R is the bending radius [47].

3.3.1 Strain plane determination

In this research work, a novel approach was developed to calculate the three-dimensional curvature by using multicore fiber.

The three-dimensional curvature is defined, once calculated the magnitude of curvature, which quantifies how much the fiber is bent, and the bending direction angle, which identifies the direction of bending. By using a MCF with at least three non-aligned cores, the curvature can be determined in three dimensions, by calculating the strain surface (also called strain function, strain distribution or strain plane) $\varepsilon(x,y)$, illustrated in the Fig. 3.5.

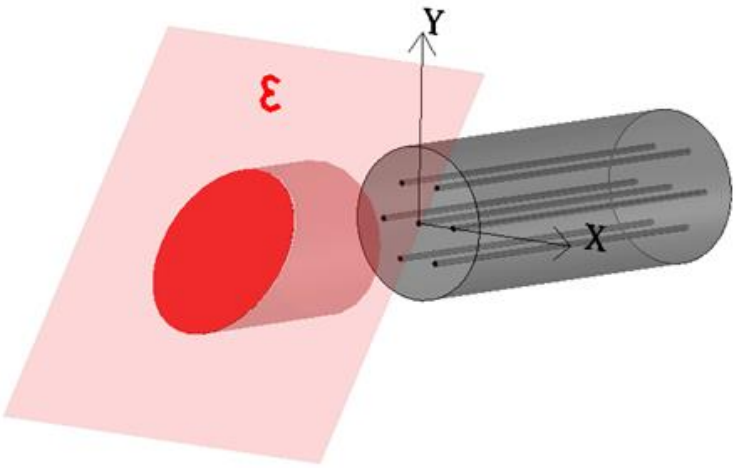

Fig. 3.5. 3D distribution of the strain in a MCF due to bending and tensile force.

According to the Euler-Bernoulli beam theory and under the hypotheses presented above, the strain surface, $\varepsilon(x,y)$, which describes the strain variation due to bending along the section, is a plane. This is the reason why it can be determined only if the strain of at least three non-aligned cores is known.

The equation of this plane can be determined from the coordinates of the cores (after defining a local Cartesian Coordinate System (x,y) centered on the mid-section) and the values of strain measured. The strain distribution, $\varepsilon(x,y)$, in a generic section, is defined when are known the longitudinal strain of the section (average strain, $avg(\varepsilon)$),ε^{long}, and the two components of curvature, κ_x and κ_y, with respect to the reference axes of the section, x and y, or the magnitude of the vector curvature, $|\kappa|$, and the bending direction angle, α, which identifies the bending direction:

$$\varepsilon(x,y) = a + bx + cy \tag{3.7}$$

$$where\ \ a = \varepsilon^{long}; b = \kappa_x; c = \kappa_y;$$

where a, b, and c are the coefficients of the equation of the strain plane, equal to, respectively, the longitudinal strain, ε^{long}, and the two components of curvature, κ_x and κ_y, since they are the partial derivatives of $\varepsilon(x,y)$ with respect to x and y:

$$\kappa_x = \partial\varepsilon(x,y)/\partial x \ ; \ \kappa_y = \partial\varepsilon(x,y)/\partial y \tag{3.8}$$

If the strain is sensed at only 3 points (three-core sensor), the equation of the strain plane can be calculated by replacing the coordinates of the cores and the values of strain measured and obtaining a system of three linear equation.

When n cores are available, the strain is detected at n points and the strain function can be calculated by minimizing the Sum of Squared Errors (SSE), as shown in the following equations:

$$SSE(a,b,c) = \sum_{i=1}^{n}(\varepsilon_i - a - bx_i - cy_i)^2 \tag{3.9}$$

$$\nabla SSE(a,b,c) = 0 \tag{3.10}$$

$$\begin{cases} \frac{\partial SSE(a,b,c)}{\partial a} = 0 \rightarrow na + b\sum_{i=1}^{n} x_i + c\sum_{i=1}^{n} y_i = \sum_{i=1}^{n} \varepsilon_i \\ \frac{\partial SSE(a,b,c)}{\partial b} = 0 \rightarrow a\sum_{i=1}^{n} x_i + b\sum_{i=1}^{n} x_i^2 + c\sum_{i=1}^{n} x_i y_i = \sum_{i=1}^{n} x_i \varepsilon_i \\ \frac{\partial SSE(a,b,c)}{\partial c} = 0 \rightarrow a\sum_{i=1}^{n} y_i + b\sum_{i=1}^{n} x_i y_i + c\sum_{i=1}^{n} y_i^2 = \sum_{i=1}^{n} y_i \varepsilon_i \end{cases} \tag{3.11}$$

For the section geometries considered in this study (3-core, 4 core and 7-core fiber), thanks to the section symmetry, the system of equations becomes diagonal:

$$\begin{cases} na + 0 + 0 = \sum_{i=1}^{n} \varepsilon_i \\ 0 + b\sum_{i=1}^{n} x_i^2 + 0 = \sum_{i=1}^{n} x_i \varepsilon_i \\ 0 + 0 + c\sum_{i=1}^{n} y_i^2 = \sum_{i=1}^{n} y_i \varepsilon_i \end{cases} \tag{3.12}$$

Once the strain function equation has been determined, the magnitude of the vector curvature, $|\kappa|$, and the bending direction angle, α, can be calculated:

$$|\kappa| = \sqrt{\kappa_x^2 + \kappa_y^2} \tag{3.13}$$

$$\alpha = \tan^{-1}(\kappa_x/\kappa_y) \tag{3.14}$$

Figs. 3.6 and 3.7 show the curvature vector and the bending direction angle.

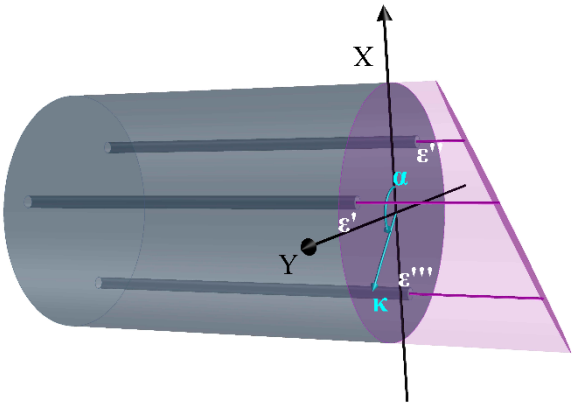

Fig. 3.6. 3D strain surface and curvature vector in a 3-core MCF due to bending and tensile force.

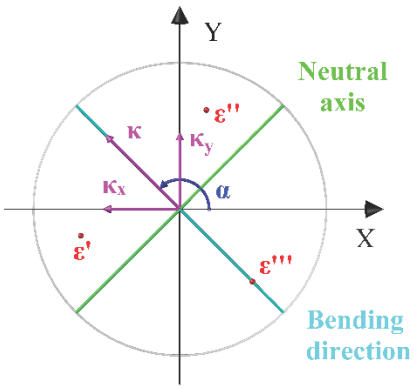

Fig. 3.7. Curvature and bending direction in a MCF cross-section subject to bending.

It should be pointed out that **a central core does not have any effect on the calculation of curvature and bending direction angle** (second and third equations of system), as its coordinates *x* and *y* are null [91].

It should be stressed that the method here proposed is only valid when external twisting is prevented (no local twisting forces are induced in the sensor). The effects of the external twisting will be discussed in Chapter 6.

It is worth noting that the mathematical approach, here presented, for 3D curvature calculation is valid for any section geometry with a generic number of cores *n* and without any symmetry, provided that there are at least three non-aligned cores. Therefore, it is particularly convenient when dealing with any not-standard multicore fiber.

3.4 Numerical integration of the Frenet-Serret formulas

In this study, the shape of the sensor was reconstructed from the 3D curvature along the fiber through numerical integration of the Frenet-Serret formulas, one of the most used approaches, first proposed by Moore and Rogge [50].

When the curvature and bending direction angle values are known in several sections, the function of curvature $\kappa(s)$ and torsion $\tau(s)$ along the fiber can be calculated by interpolation or curve fitting [50,151]. Once these functions and the boundary conditions are known, which are the position $\boldsymbol{r_0}$ and the Frenet frame $\boldsymbol{T_0}$, $\boldsymbol{N_0}$, $\boldsymbol{B_0}$ of the starting point, the shape can be reconstructed through numerical integration of the Frenet-Serret formulas, which can be written as:

$$\begin{bmatrix} \boldsymbol{T}' \\ \boldsymbol{N}' \\ \boldsymbol{B}' \end{bmatrix} = \begin{bmatrix} 0 & \kappa & 0 \\ -\kappa & 0 & \tau \\ 0 & -\tau & 0 \end{bmatrix} \begin{bmatrix} \boldsymbol{T} \\ \boldsymbol{N} \\ \boldsymbol{B} \end{bmatrix} \tag{3.15}$$

where $\boldsymbol{T}$, $\boldsymbol{N}$ and $\boldsymbol{B}$ are respectively tangent, normal and binormal vectors.

Alternatively, if only bi-dimensional curvature is measured, it is still possible to perform 2D shape reconstruction. In this case, only the curvature function is taken into account and the Frenet-Serret formulas become:

$$\begin{bmatrix} \boldsymbol{T}' \\ \boldsymbol{N}' \end{bmatrix} = \begin{bmatrix} 0 & \kappa \\ -\kappa & 0 \end{bmatrix} \begin{bmatrix} \boldsymbol{T} \\ \boldsymbol{N} \end{bmatrix} \tag{3.16}$$

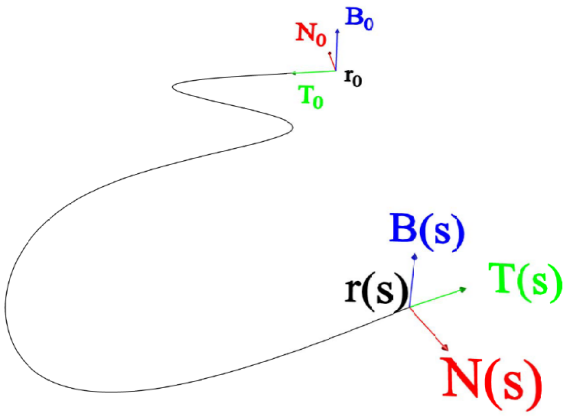

Fig. 3.8. Space curve and Frenet-Serret frames at the starting point 0 at a generic point s.

3.5 Conclusions

This Chapter presented an innovative approach for shape reconstruction using optical multicore fiber with embedded Fiber Bragg Gratings. First, the longitudinal strain along the fiber is detected, by tracking the wavelength, a technique widely used in the literature [54,93,143,151,152,156,157]. Next, the curvature in each instrumented section is calculated, using a novel method, developed in this research work. Such method relies on the determination of the strain plane and allows the curvature calculation of any type of fiber section, once the value of strain and the location of at least three nonaligned cores are known. Finally, the shape of the sensor is reconstructed using the method, first proposed by Moore and Rogge, in 2012, to reconstruct complex three-dimensional fiber shapes as a continuous parametric solution through the numerical resolution of a set of Frenet-Serret equations [158].

The fundamental advantage of this method compared to those previously reported in the literature is the capability of calculating the curvature of any multicore fiber geometry. In fact, the alternative approaches were developed taking into account a particular section geometry and cores configuration, for instance the three-core section with equal angular spacing [158].

CHAPTER 4
EFFECTS OF STRAIN RESOLUTION AND CORE POSITION ERRORS

4.1 Introduction

This chapter describes a numerical study carried out to investigate the uncertainty of optical multicore fiber shape sensors in the calculation of three-dimensional curvature (or curvature and bending direction) and longitudinal strain, caused by the strain measurement and core position errors. High precision in curvature and bending direction computation is crucial for efficient shape sensing, being the inputs of the process of shape reconstruction. Furthermore, curvature and bending direction sensing are employed in a number of in structural health monitoring applications infrastructures [133], such as continuous monitoring of the verticality of structures, including buildings, towers, bridge piles, tunnel displacement, etc.

An algorithm was designed to reproduce the real measurement process and simulate the real position of the cores and strain measurement uncertainty of each core, supposing that they are affected by random errors with a Gaussian distribution, characterized by different standard deviations (SD) [159,160]. The Monte Carlo method was employed to carry out the analysis, taking into consideration the influence of curvature measured and core spacing (distances between the sensor axis and the outer cores), in both of the cases, and number of cores, only in the case of core positions errors.

Finally, the propagation laws of errors were successfully identified and a series of predictive models were calibrated, by fitting the simulations outcomes. The equations of these models describe the influence of strain sensing inaccuracy and core position errors on the optical multicore fiber performance, taking into account the role played by the other parameters.

4.2 Methodology

4.2.1 Monte Carlo Method

Widely accepted as an efficient problem solving tool, the Monte Carlo Method (MCM) is an experimental probabilistic technique designed to solve complex linear and nonlinear statistical or scientific problems [161–164]. Since modern computers can efficiently simulate large numbers of experimental trials that have random

outcomes, MCM, a large class of computational algorithms, were developed to confront processes that could not be easily predicted with the aim of obtaining numerical results and modeling the probability of different outcomes that rely on repeated random sampling.

Despite the exactness of analytical methods, they are only suitable for simple cases that admit a closed-form solution, whereas identifying distribution propagation in complex problems requires approximations and simulations [160]. The MCM can be used to determine the probability distribution for an output quantity from the probability distributions assigned to the input quantities on which the output quantity depends in order to define the law of propagation [160,165]. When applied to the propagation of uncertainty, the MCM mimics the real probabilistic measurement process by mean of the uncertainty of random sampling and generation hundreds of thousands of measures and resulting outcomes to individuate the relationship between the variables involved. Before the simulation, a specification of the input probability distribution needs to be defined to perform the random sampling.

The MCM has previously been used to simulate optical curvature sensing [166,167]; it has been utilized, for instance, to mimic curvature gauges by means of ray tracing and identify the relationship between fiber curvature and light-loss.

In this research, MCM was employed to simulate, as shown in Fig. 4.1, the effects on curvature and bending direction angle calculation of:

- Case of study 1. The strain measurement uncertainty (the errors in strain measurement mimic the different strain resolution of the interrogation system);
- Case of study 2. The effects of core position errors.

  It was assumed that the errors that affect different cores and different sections are independent and uncorrelated, have only one random component and follow a standard normal distribution (the Gaussian probability distribution is the simulation input) with a certain standard deviation (SD). For each trial and in all the cores, the errors simulated were added to the correct value.

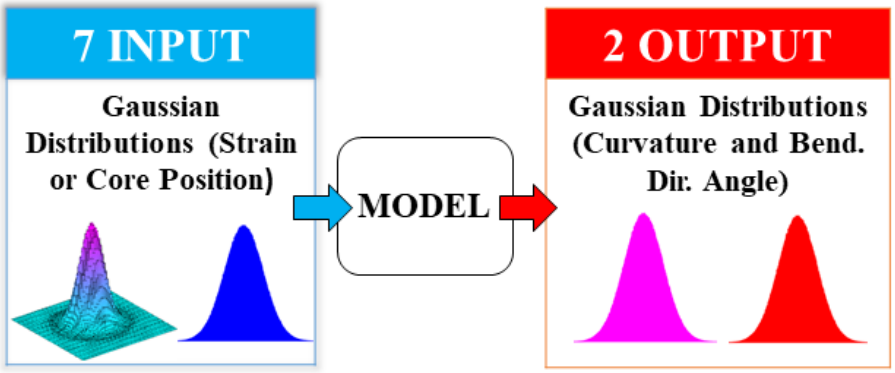

Fig. 4.1. Procedure for curvature and bending direction angle distribution calculation.

4.2.2 Source of errors

The errors in strain measurement represent the errors of the strain measurement process, which depend on interrogation process: resolution of the interrogation system and environmental conditions: temperature, vibrations, etc.; in the case of FBGs, the technique used to track the peaks and determine the shift of wavelength, conversion of shift of wavelength in strain, while, the spatial resolution, in the case of distributed sensing based on Brillion and Rayleigh scattering.

In multiple single-core optical fiber shape sensors, the core position errors are acquired during manufacture and depend on the optical fiber drawing technique, the production equipment used for the multicore fibers and fiber bundles, and on the technique used to fasten the fibers to the support (generally a tube), as well as the support's characteristics. Regrettably, manufacturers rarely provide information on any such errors.

4.2.3 Stopping rules

MCM effectiveness is a function of the number of trials in the simulation (sample size). When the number of samples increases, the simulation converges to a constant outcome and thus should be halted. Regrettably, the number of trials necessary for steady outcome cannot be theoretically calculated [168]. Nonetheless, in most cases a sample size between 10^5 and 10^6 replicates seem to be satisfactory [163,169]. Furthermore, a number of observations of 10^6 can commonly be envisaged to achieve a 95 % coverage probability for the output variable, so that this size is right to one or even two significant digits [160].

Each simulation in this research was performed with the following number of iterations and stopping criteria:

- First case of study: 10^6 iterations. For each simulation, the total dataset consisted of 5 subdatasets with $2 \cdot 10^5$ trials each, then, to ensure that the

simulations were statistically significant, the values obtained with the five subdatasets were compared with the value given by the total dataset.

- Second case of study: $3 \cdot 10^6$ replicates. It was considered a dataset composed of 3 subdatasets with 10^6 iterations each. Hence, to verify the statistical significance of the simulations, a comparison was drawn between the results of the total dataset and the ones obtained with the three subdatasets.

4.3 Case of study 1 - Strain resolution effects

4.3.1 Multi-step procedure for curvature and bending direction calculation

An algorithm was developed in MATLAB® code [170] to generate the error distribution by the Monte Carlo method and compute the resulting distribution of longitudinal deformation, curvature and bending direction. The procedure can be summarized as follows:

- Step 1. Strain calculation in all the cores, given the fiber geometry, longitudinal deformation, curvature and bending direction;
- Step 2. Simulation of strain Gaussian distribution in all the cores, given the standard deviation in strain detection;
- Step 3. Calculation of longitudinal deformation, curvature and bending direction angle distribution through Multivariate Linear Regression analysis;
- Step 4. Tests of Statistical Significance.

4.3.2 Part a) Uncertainty in curvature calculation

Fifteen simulations were performed to study the measurement uncertainty in curvature determination considering: longitudinal strain equal to 0 με; bending direction corresponding to axis x; three different values of core spacing, including 70, 50 and 30 μm; five different values of standard deviation in strain measurement, including 5, 2.5, 1, 0.5 and 0.2 με. The values of strain measurement were chosen considering that the resolution of commercial interrogation system is nowadays around 1 με and a great effort is paid in increasing the precision of these device measurements. Therefore, a reasonable value of strain measurement SD is between 5 and 0.2 με. Since the sensed curvatures have no influence on curvature distribution, their values were calculated so that the maximum strain value in the section, without measurement errors, was equal to 1000 με, as shown in Table 4.1.

Table 4.1. Simulations for identification of uncertainty in curvature calculation.

Simulation Nº	Longitudinal Strain [με]	Angle between Bend. Dir. and axis x [rad]	Curvature [m^{-1}]	Core spacing [μm]	SD in Strain Measurement [με]
1	0.00	0.00	14.286	70.00	5.00
2	0.00	0.00	14.286	70.00	2.50
3	0.00	0.00	14.286	70.00	1.00
4	0.00	0.00	14.286	70.00	0.50
5	0.00	0.00	14.286	70.00	0.20
6	0.00	0.00	20.000	50.00	5.00
7	0.00	0.00	20.000	50.00	2.50
8	0.00	0.00	20.000	50.00	1.00
9	0.00	0.00	20.000	50.00	0.50
10	0.00	0.00	20.000	50.00	0.20
11	0.00	0.00	33.333	30.00	5.00
12	0.00	0.00	33.333	30.00	2.50
13	0.00	0.00	33.333	30.00	1.00
14	0.00	0.00	33.333	30.00	0.50
15	0.00	0.00	33.333	30.00	0.20

4.3.3 Part b) Uncertainty in bending direction calculation

Eighteen simulations were performed with a view to analyzing the measurement uncertainty in determining the angle between bending direction and axis x, considering:

- longitudinal strain equal to 0 με;
- bending direction corresponding to axis x;
- three different values of core spacing, namely 70, 50 and 30 μm;
- three different values of standard deviation in strain measurement, namely 5, 1 and 0.2 με;
- two different values of curvature for each core spacing value, as shown in Table 4.2.

Fig. 4.2 shows an example of the Gaussian error distributions in the cores of the first simulation of the first case study, part b. The exact values of strain in the core, not affected by measurement errors, are shown in Table 4.3.

Table 4.2. Simulations for identification of uncertainty in bending direction calculation.

Simulation Nº	Longitudinal Strain [με]	Angle between Bend. Dir. and axis x [rad]	Curvature [m^{-1}]	Core spacing [μm]	SD in Strain Measurement [με]
1	0.00	0.00	0.071	70.00	5.00
2	0.00	0.00	0.214	70.00	5.00
3	0.00	0.00	0.071	70.00	1.00
4	0.00	0.00	0.214	70.00	1.00
5	0.00	0.00	0.071	70.00	0.20
6	0.00	0.00	0.214	70.00	0.20
7	0.00	0.00	0.200	50.00	5.00
8	0.00	0.00	0.400	50.00	5.00
9	0.00	0.00	0.200	50.00	1.00
10	0.00	0.00	0.400	50.00	1.00
11	0.00	0.00	0.200	50.00	0.20
12	0.00	0.00	0.400	50.00	0.20
13	0.00	0.00	0.500	30.00	5.00
14	0.00	0.00	0.833	30.00	5.00
15	0.00	0.00	0.500	30.00	1.00
16	0.00	0.00	0.833	30.00	1.00
17	0.00	0.00	0.500	30.00	0.20
18	0.00	0.00	0.833	30.00	0.20

Table 4.3. Strain values in the seven cores without measurement errors in the first simulation of the 1º case study, part b.

Curvature [m^{-1}]			Core spacing [μm]		SD in Strain Measurement [με]	
0.71			70.00		5.00	
ε_1	ε_2	ε_3	ε_4	ε_5	ε_6	ε_7
0.00	5.00	2.50	-2.50	-5.00	-2.50	2.50

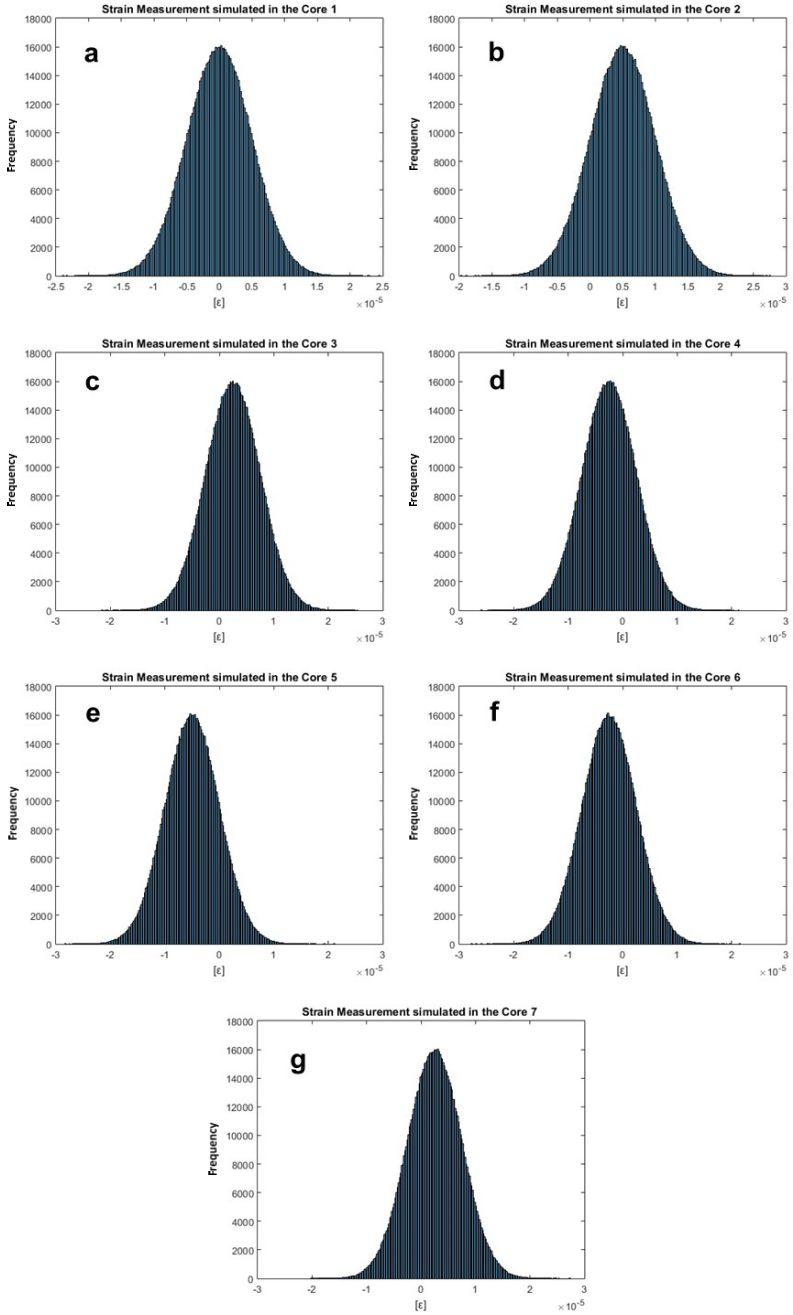

Fig. 4.2. Strain measurement simulated in the first simulation of the identification of uncertainty in bending direction in core 1 (a); core 2 (b); core 3 (c); core 4 (d); core 5 (e); core 6 (f); core 7 (g).

4.3.4 Calculating curvature, bending direction and longitudinal strain

Considering the error-affected strain value generated by MCM, the curvature and bending direction were calculated in each trial to determine the relation between core spacing and the standard deviations of strain measurement and curvature and bend direction angle.

The strain surface was first calculated considering the strain values of the 7 cores through a Multivariate Linear Regression analysis, as illustrated in Section 3 of Chapter 3. The curvature was then calculated by Eqs. (4.1) and (4.2) with the known strain plane equation $\varepsilon(x,y)$:

$$\kappa = \sqrt{\kappa_X^2 + \kappa_Y^2} \tag{4.1}$$

$$\kappa_x = \Delta\varepsilon_x/2s;\ \kappa_y = \Delta\varepsilon_y/2s \tag{4.2}$$

where κ is the curvature, κ_x and κ_y are, respectively, the components of curvature along the axis x and y, $\Delta\varepsilon_x$ and $\Delta\varepsilon_y$ are the variations in strain along the axis x and y respectively and s is the spacing core, the distance between the fiber center and the outer core centers. The bending direction, or direction of maximum curvature, and longitudinal strain (average strain in the section) were then calculated.

4.4 Case of study 1 - Results of the analyses

This section deals with the outcome of the experiments for longitudinal, curvature and bending direction calculation.

4.4.1 Longitudinal strain distribution

The longitudinal strain of the fiber distribution (supposed equal to zero without measurements errors) was calculated for each simulation. Fig. 4.3 shows an example of the longitudinal strain distribution (first simulation of the first case study, part b), which is clearly Gaussian. The SD of the distribution remained below a value of $2 \cdot 10^{-6}$ με during the entire simulation.

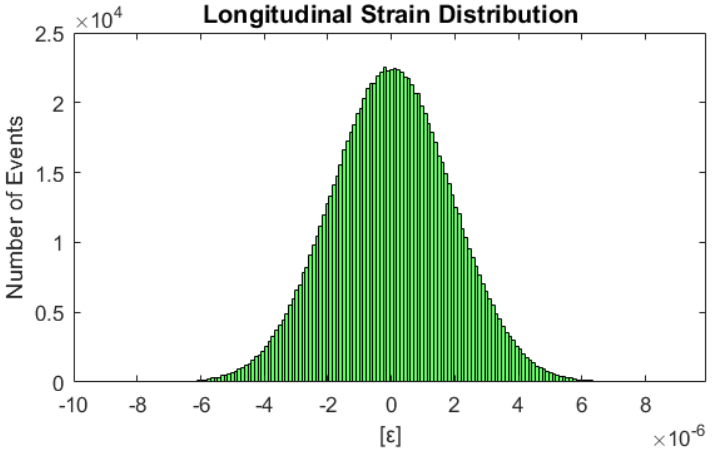

Fig. 4.3. Longitudinal fiber strain measurement simulated in the 7 core in the first simulation of the first case study, part b [171].

4.4.2 Test of statistical significance

As explained in Subsection 4.2.3, MCM requires a stopping rule that determines the length of the sample records (number of samples in the simulation). Since the appropriate number of iterations cannot be estimated theoretically [23], we opted for 10^6, which seems to be enough in most cases [18,24]. The correctness of this assumption was later verified. For each simulation, the curvature distribution of the total dataset, consisting of 5 subdatasets with $2 \cdot 10^5$ trials each, was determined and its standard deviation was compared with the standard deviation of the distribution of the subdatasets. The percentage error of the subdatasets' SD was then compared with that of the total dataset SD for each simulation by Eq. (4.3):

$$Ep = [(s^T - s^S)/s^T]100 \tag{4.3}$$

where *Ep* is the percentage error, s^T is the standard deviation of the total dataset and s^S is the standard deviation of the subdataset.

4.4.3 Part a) Curvature calculation

Fifteen simulations were carried out to evaluate the effect of the errors on strain measurement and the variation of core spacing in curvature sensing, as explained at point 4.3.2, including different SD values in strain measurement and core spacing. Since the curvature was calculated as the vector addition of the two curvature components along the *x* and *y* axes by Eq. (4.1), curvature is a positive-definite function, so that in the neighborhood of the origin the shape of the distribution is distorted, as can be seen in Fig. 4.4. To avoid this inconvenience, the distributions of the curvature components along the *x* and *y* axes may be studied, as shown in Fig. 4.5. In view of this, in the first part of this case study only considerable curvatures

far removed from the value of zero were analyzed. Fig. 4.6 shows, as example, the distribution of the curvature in the first simulation of the first case of study, part a. The curvature distribution is still Gaussian.

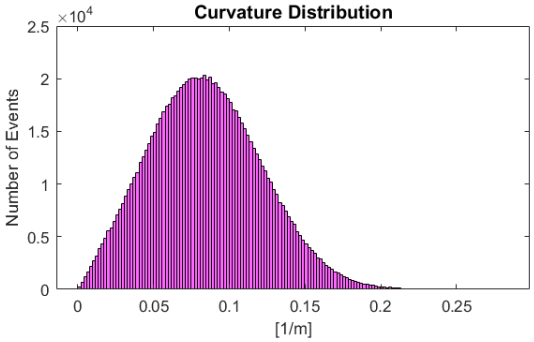

Fig. 4.4. Curvature distribution in first simulation for the identification of uncertainty in bending direction calculation [171].

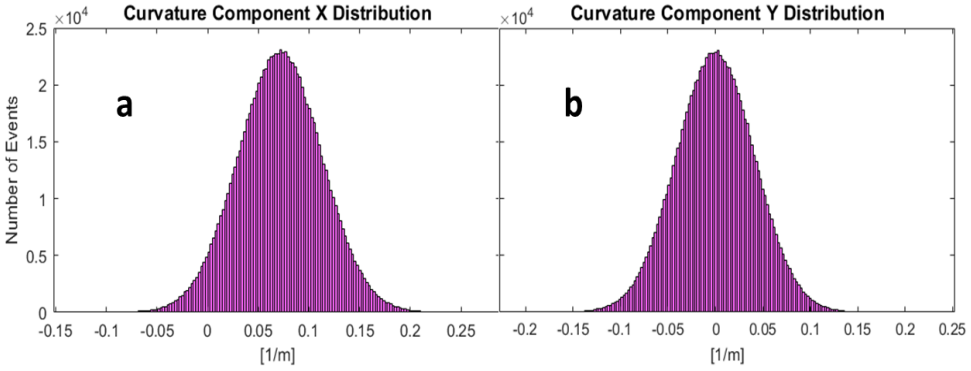

Fig. 4.5. Distribution of curvature along axis *x* (a) and the axis *y* (b) in first simulation for the identification of uncertainty in bending direction calculation [171].

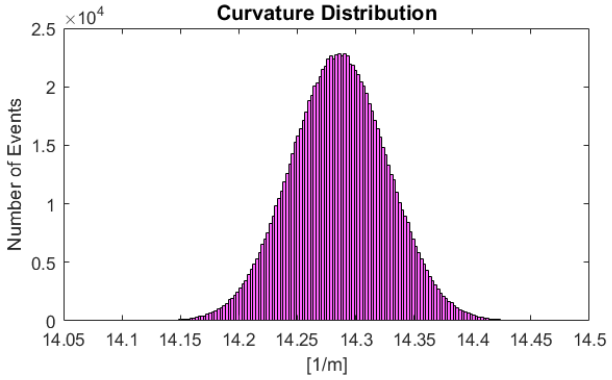

Fig. 4.6. Curvature distribution in first simulation for the identification of uncertainty in curvature calculation [171].

The outcomes of the first experiment are shown in Table 4.4. Three different core spacing values and five different SD values were considered in strain measurement. The curvature values were calculated so that the maximum strain value in the section, without measurement errors, was equal to 1000 με. This was possible since the curvature sensed had no influence on the curvature distribution. Curvature distribution was calculated for each simulation considering its SD.

Fig. 4.7 shows the variation of the curvature and strain standard deviations at a constant core spacing value. As can be seen, curvature SD varies linearly with strain SD. The regression line equations and coefficients of determination (R^2) are shown in the figure.

Table 4.4. Curvature standard deviation results.

Simulation Nº	**Curvature [m^{-1}]**	**Core spacing [μm]**	**SD in Strain Measurement [με]**	**Curvature SD [m^{-1}]**
1	14.2857	70.00	5.00	0.0412
2	14.2857	70.00	2.50	0.0206
3	14.2857	70.00	1.00	0.0083
4	14.2857	70.00	0.50	0.0041
5	14.2857	70.00	0.20	0.0016
6	20.0000	50.00	5.00	0.0578
7	20.0000	50.00	2.50	0.0289
8	20.0000	50.00	1.00	0.0115
9	20.0000	50.00	0.50	0.0058
10	20.0000	50.00	0.20	0.0023
11	33.3333	30.00	5.00	0.0963
12	33.3333	30.00	2.50	0.0481
13	33.3333	30.00	1.00	0.0192
14	33.3333	30.00	0.50	0.0096
15	33.3333	30.00	0.20	0.0038

The curvature SD variation with constant core spacing at a constant SD deviation value is shown in Fig. 4.8. In this case, the relationships are not linear and were approximated by a quadratic polynomial, whose equations are shown in the figure.

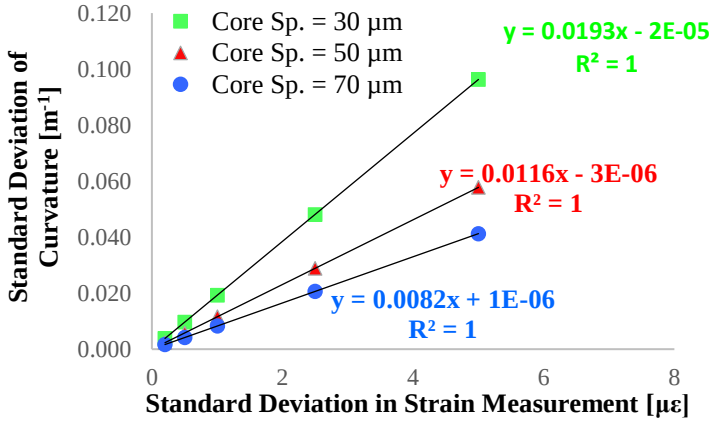

Fig. 4.7. Curvature SD results for each strain SD point at constant core spacing values.

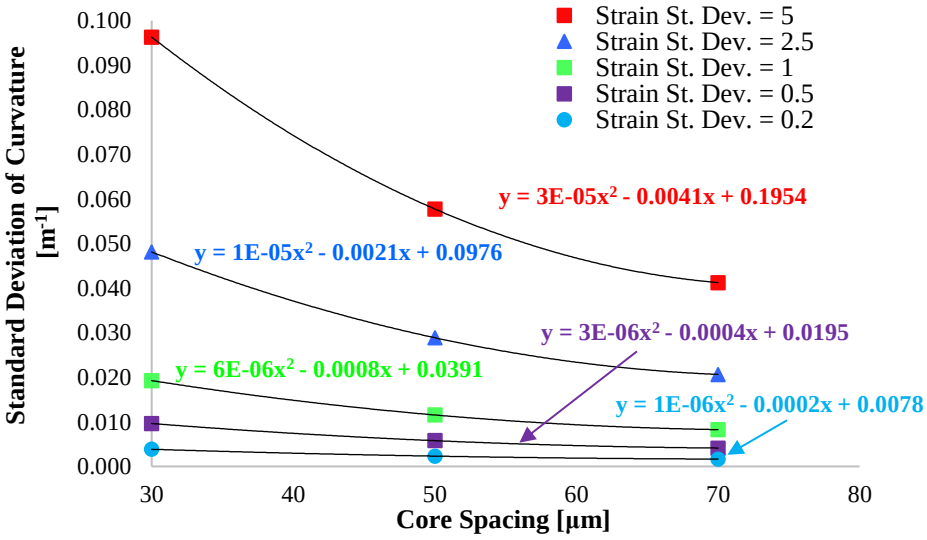

Fig. 4.8. Curvature SD results for each core spacing point at constant values of strain SD.

To prove the correctness of the simulations, a test of statistically significant was carried out, as explained in Section 4.4.2. The results of the comparison between Curvature SD of the total dataset and subdataset and the resulting the percentage errors of all the simulations in the first case study, part a, are listed in Table 4.5 and 4.6. The highest percentage error obtained was 0.340, indicating that the simulation can be considered statistically significant.

Table 4.5. Curvature SD results; comparison of subdatasets and total datasets.

Simulation N°	SD Curvature					
	1º subdat.	2º subdat.	3º subdat.	4º subdat.	5º subdat.	Total dataset.
1	0.041250	0.041247	0.041209	0.041243	0.041257	0.041241
2	0.020658	0.020605	0.020615	0.020704	0.020586	0.020633
3	0.008245	0.008251	0.008248	0.008258	0.008269	0.008254
4	0.004125	0.004113	0.004120	0.004117	0.004121	0.004119
5	0.001654	0.001647	0.001644	0.001651	0.001649	0.001649
6	0.057681	0.057791	0.057660	0.057810	0.057844	0.057757
7	0.028966	0.028846	0.028876	0.028797	0.028860	0.028869
8	0.011551	0.011525	0.011510	0.011553	0.011578	0.011543
9	0.005769	0.005768	0.005782	0.005777	0.005787	0.005777
10	0.002312	0.002306	0.002310	0.002311	0.002310	0.002310
11	0.096011	0.096468	0.096271	0.096349	0.096428	0.096305
12	0.048108	0.048173	0.048150	0.048026	0.048092	0.048110
13	0.019209	0.019247	0.019250	0.019275	0.019251	0.019247
14	0.009626	0.009604	0.009620	0.009620	0.009631	0.009620
15	0.003844	0.003851	0.003842	0.003846	0.003842	0.003845

Table 4.6. Curvature standard deviation results; percentage errors.

Simulation N°	Percentage Error				
	1º dataset	2º dataset	3º dataset	4º dataset	5º dataset
1	-0.022	-0.015	0.078	-0.005	-0.037
2	-0.117	0.137	0.091	-0.340	0.230
3	0.107	0.038	0.076	-0.044	-0.177
4	-0.135	0.154	-0.015	0.041	-0.044
5	-0.277	0.114	0.315	-0.136	-0.015
6	0.132	-0.058	0.168	-0.091	-0.150
7	-0.336	0.079	-0.025	0.251	0.033
8	-0.065	0.161	0.288	-0.082	-0.299
9	0.129	0.151	-0.093	-0.009	-0.177
10	-0.088	0.166	0.013	-0.065	-0.025
11	0.306	-0.169	0.036	-0.045	-0.128
12	0.003	-0.130	-0.083	0.174	0.038
13	0.196	-0.003	-0.018	-0.148	-0.025

14	-0.061	0.166	0.004	0.004	-0.114
15	0.022	-0.158	0.086	-0.025	0.075

4.4.4 Part b) Calculating bending direction angle

The second part of the case study involved the impact of the strain measurement SD and core spacing on the bending direction calculations. The bending direction and the angle between the bending direction and the x axis (null without measurement errors) were estimated for each trial. The distribution of the bending direction angle was then considered for each simulation. Once again, as in the strain measurement, the distribution of the resulting quantity was Gaussian, as can be seen from Fig. 4.9. The bending direction angle distribution was studied in the interval from $-\pi$ to $+\pi$ in order to identify all the possible configurations of the bending axis.

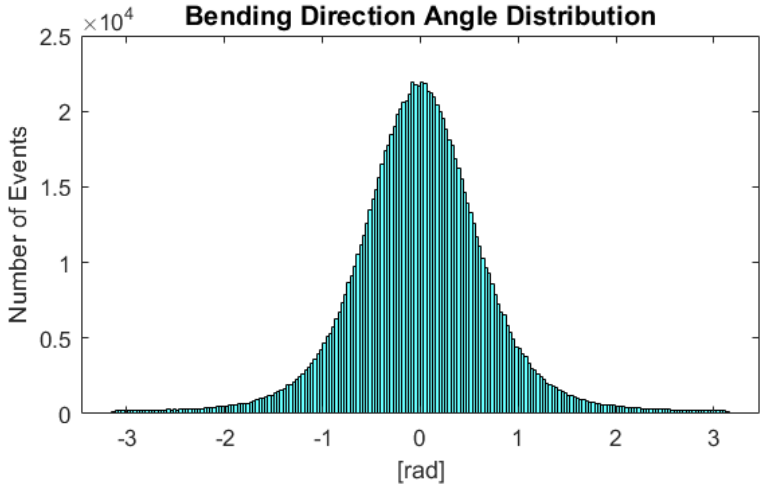

Fig. 4.9. Bending direction angle distribution of the first simulation to identify uncertainty in bending direction calculations.

The SD associated with each simulation are listed in Table 4.7. Three different values of core spacing and three different values of standard deviation in strain measurement were considered. Since the standard deviation of the bending direction angle distribution was found to be closely dependent on the curvature sensed in the preliminary analysis, two different curvature values were considered for each strain SD and core spacing value.

Table 4.7. Bending direction angle standard deviation results.

Simulation N°	Curvature [m^{-1}]	Core spacing [μm]	SD in Strain Measur. [με]	Bend. Dir. Angle SD
1	0.0714	70.00	5.00	0.7142
2	0.2143	70.00	5.00	0.1964
3	0.0714	70.00	1.00	0.1164
4	0.2143	70.00	1.00	0.0385
5	0.0714	70.00	0.20	0.0231
6	0.2143	70.00	0.20	0.0077
7	0.2000	50.00	5.00	0.3051
8	0.4000	50.00	5.00	0.1459
9	0.2000	50.00	1.00	0.0579
10	0.4000	50.00	1.00	0.0288
11	0.2000	50.00	0.20	0.0115
12	0.4000	50.00	0.20	0.0058
13	0.5000	30.00	5.00	0.1965
14	0.8333	30.00	5.00	0.1161
15	0.5000	30.00	1.00	0.0385
16	0.8333	30.00	1.00	0.0231
17	0.5000	30.00	0.20	0.0077
18	0.8333	30.00	0.20	0.0046

Fig. 4.10 shows the bending direction angle SD variation with strain SD at a constant value of core spacing and curvature. The bending direction angle SD varies linearly with the strain SD. The regression line equations and coefficients of determination (R^2) are included in the figure. As can be seen, the data points with a curvature of 0.214 m^{-1} and core spacing 70 μm coincide with those associated with curvature values of 0.500 m^{-1} and core spacing of 30 μm, since the product of curvature and core spacing is the same in both cases.

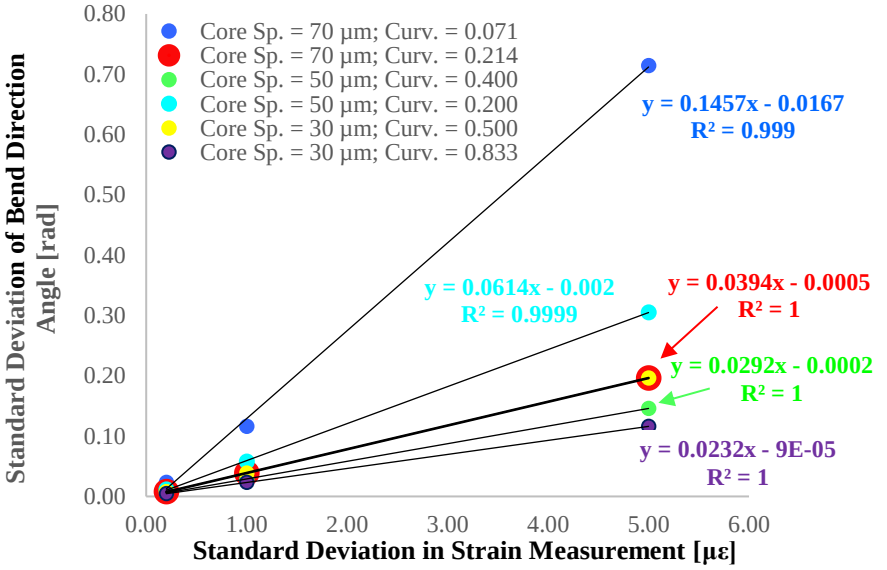

Fig. 4.10. Bending direction angle SD results for each strain SD data point at constant core spacing and curvature values.

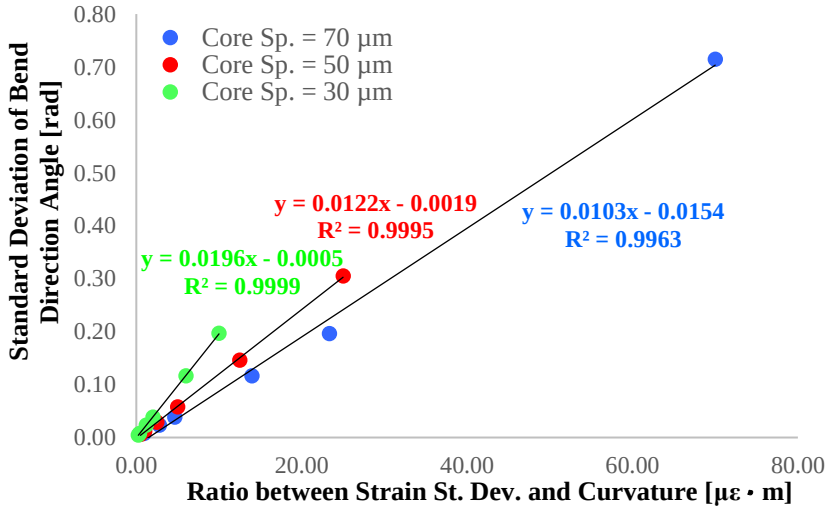

Fig. 4.11. Bending direction angle SD results for each strain SD and curvature ratio data point at constant core spacing values.

Since the accuracy of the bending axis estimation greatly depends on the sensed curvature, the variation of the bending direction angle SD was studied considering the ratio between strain SD and curvature at a fixed value of core spacing (see Fig. 4.11), and the product of core spacing and curvature at a fixed value of strain SD (see Fig. 4.12). In first case, the relationships are linear, whereas in the second is not

linear. The regression line equations and coefficients of determination (R^2) are included in the figures.

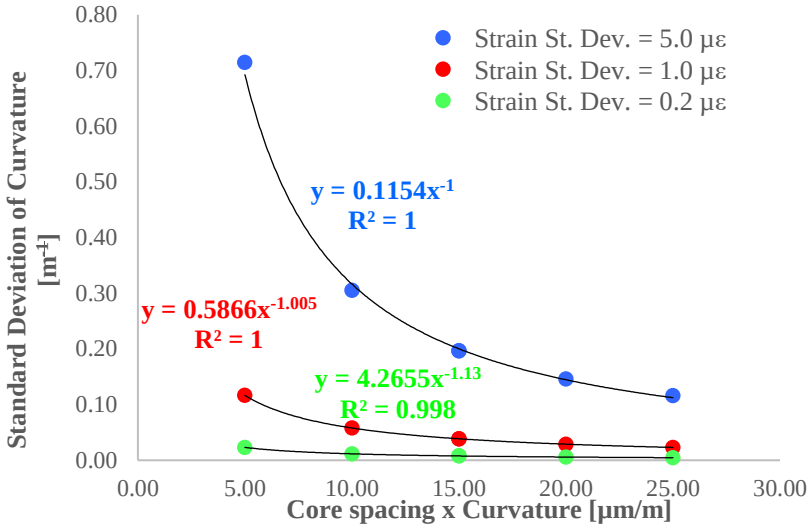

Fig. 4.12. Bending direction angle SD results for each core spacing and curvature product data point at constant strain SD values.

Here again a test of statistical significance was carried out to verify that the length of the sample records (10^6) was statistically robust by comparing the results obtained with the subdatasets and the total dataset. In each simulation, the percentage errors of the subdatasets were compared with the total dataset by Eq. (4.3). The highest percentage error obtained was 0.361, indicating that the simulation can be considered statistically significant. The results are shown in Tables 4.8 and 4.9.

Table 4.8. Bending direction angle SD results; comparison of subdatasets and total dataset.

Simulation N°	SD Bending Direction Angle					
	1º dataset	2º dataset	3º dataset	4º dataset	5º dataset	Total dataset
1	0.713099	0.712740	0.715035	0.715513	0.714393	0.714156
2	0.196032	0.196060	0.196784	0.196507	0.196430	0.196362
3	0.116487	0.116364	0.116278	0.116615	0.116200	0.116389
4	0.038519	0.038558	0.038617	0.038453	0.038412	0.038512
5	0.023031	0.023104	0.023050	0.023048	0.023108	0.023068
6	0.007700	0.007719	0.007686	0.007700	0.007694	0.007700
7	0.305244	0.304521	0.304990	0.305689	0.305210	0.305131
8	0.145566	0.145794	0.146136	0.145968	0.145992	0.145891

9	0.057893	0.058085	0.057790	0.057979	0.057782	0.057906
10	0.028811	0.028781	0.028924	0.028826	0.028872	0.028843
11	0.011516	0.011559	0.011524	0.011556	0.011581	0.011547
12	0.005779	0.005780	0.005779	0.005762	0.005764	0.005773
13	0.196357	0.196175	0.196551	0.196377	0.196933	0.196479
14	0.116109	0.115894	0.116204	0.116303	0.116170	0.116136
15	0.038444	0.038521	0.038628	0.038637	0.038483	0.038543
16	0.023083	0.023074	0.023115	0.023104	0.023102	0.023096
17	0.007700	0.007707	0.007666	0.007697	0.007700	0.007694
18	0.004613	0.004608	0.004622	0.004612	0.004605	0.004612

Table 4.9. Bending direction angle SD results; percentage errors.

Simulation Nº	**Percentage Error**				
	1° dataset	**2° dataset**	**3° dataset**	**4° dataset**	**5° dataset**
1	-0.148	-0.198	0.123	0.190	0.033
2	-0.168	-0.154	0.215	0.073	0.035
3	0.084	-0.021	-0.095	0.194	-0.162
4	0.018	0.120	0.273	-0.153	-0.259
5	-0.161	0.154	-0.077	-0.088	0.173
6	0.000	0.247	-0.176	0.001	-0.072
7	0.037	-0.200	-0.046	0.183	0.026
8	-0.223	-0.066	0.168	0.053	0.069
9	-0.021	0.309	-0.200	0.126	-0.213
10	-0.111	-0.212	0.281	-0.059	0.102
11	-0.274	0.104	-0.204	0.078	0.294
12	0.117	0.119	0.107	-0.190	-0.154
13	-0.062	-0.154	0.037	-0.052	0.231
14	-0.023	-0.209	0.059	0.144	0.029
15	-0.255	-0.057	0.222	0.244	-0.155
16	-0.053	-0.095	0.085	0.036	0.026
17	0.079	0.171	-0.361	0.038	0.072
18	0.019	-0.084	0.213	0.004	-0.153

4.4.5 Discussion

The following conclusions can be drawn from this study:

- MCM is an efficient method to study the propagation of the strain measurement errors in calculating curvature and bending direction.
- The curvature distribution is greatly and non-linearly influenced by the core spacing and depends linearly on the strain SD.
- The SD of the distribution of the angle between bending direction and the axis *x* depends linearly on the core spacing and the measured strain SD. As it is also strongly dependent on the curvature sensed, the accuracy of the sensor is related to the application.
- The precision in determining curvature and bending direction largely depends on the core spacing. A highly sensitive shape sensor could be designed with larger core spacing fibers than those employed in telecommunications.
- The precision of bending direction and curvature detection can be calculated after determining the core spacing of the fiber, the strain measurement SD and the curvature sensed, using the charts in Figures 4.7-4.8 and 4.10-4.12.

The outcomes show the strong influence of strain uncertainty and core spacing on MCF sensor accuracy in sensing curvature and bending direction. The relations identified in this research project could be used to calculate the maximum performance achievable by 7-core MCF curvature sensors after defining the core spacing and strain SD of the interrogation system. However, it should be taken into account that if further errors affect the phenomenon the precision will be lower than expected.

These results show that a different fiber geometry with larger core spacing could be produced by taking advantage of the remarkable improvement that can be obtained by slightly increasing the distance between the outer cores and the fiber axis. Furthermore, the proposed equations can be used to design sensors with the required accuracy for specific cases of determining curvature and bending direction.

It has to be pointed out that, even though this study was focused on errors that affect the performance of multicore fiber shape sensors, the resulting research findings can be applied to both multiple single-core optical fibers sensors equipped with distributed or quasi-distributed strain-sensors, or to shape-sensing arrays in general.

4.5 Case of study 2 - Core position errors effects

4.5.1 Multi-step approach for calculating longitudinal strain, curvature and bending direction

An algorithm was designed in MATLAB® [170] to model the core position error distributions by the Monte Carlo technique and generate the consequent distribution of longitudinal strain, bending direction angle and curvature, taking into account three distinct fiber geometries. The procedure is summarized in the following steps:

- Step 1. Simulation of Gaussian frequency distribution of core position errors (Section 3.3) for each section geometry, considering five different core spacings and three different SD;
- Step 2. Calculation of strain distribution, as shown in Section 3.3, based on the distributions of core position (x_i^j and y_i^j on every iteration), obtained in the previous step, and considering diverse section deformation states, definable through measured longitudinal strain, curvature and bending direction angle (coefficients of the strain plane equation), ε^{long}, $|\kappa|$ and α, as described in Section 2;
- Step 3. Determination of longitudinal strain, bending direction angle and curvature distributions by means of the equations given in Section 2, and tests of statistical significance;
- Step 4. Development of the predictive models.

To clarify the process, a specific example is provided considering the inputs of the first simulation for a three-core sensor (section geometry = 3-core; core spacing = 30.00 μm; SD core position = 0.20 μm; longitudinal strain = 0.00 με; curvature = 0.10 m^{-1}; bending direction angle = 0.00 rad).

First, the core position errors are simulated, according to the SD chosen (in this case 0.20 μm). The real core coordinates are calculated as sum of the exact coordinates, determined considering the geometrical features of the section, and the simulated errors, as shown in Table 4.10:

Table 4.10. Example of real core coordinates calculation.

	Exact Core Coordinates		**Example of Simulated Errors**		**Example of Real Core Coordinates**	
Core	**x_i [μm]**	**y_i [μm]**	**x_i [μm]**	**y_i [μm]**	**x_i [μm]**	**y_i [μm]**
1	30.00	25.98	-0.009	0.303	29.99	26.28
2	-15.00	-25.98	-0.145	0.276	-15.14	-25.70
3	-15.00	0.00	-0.107	-0.279	-15.11	-0.28

Secondly, the strain detected in each core, taking into account the state of deformation of the section (in this example ε^{long} = 0.00 με, $|\kappa|$ = 0.10 m^{-1}, and α = 0.00 rad), is calculated by using Eq. 4.4. By way of illustration, the strain detected in core 1 is computed below:

$$\varepsilon_1 = \varepsilon^{long} + |\kappa| \, (x_1 cos\, \alpha + y_1 sin\, \alpha\,) =$$
$$= 0.00 + 0.10 \, [29.99(cos\, 0.00) + 26.28(sin\, 0.00)] \qquad (4.4)$$

To conclude, the strain detected in the cores, calculated as indicated above, and the simulated core coordinates arising from core position errors, are substituted into Eqs. 6. Thus, the longitudinal strain, ε^{long}, the magnitude of the vector curvature, $|\kappa|$, and the bending direction angle, α, now affected by the errors in core position, are determined by solving the system and using Eqs. 3.12-14.

In each simulation, this procedure was repeated for each of the $3 \cdot 10^6$ iterations, divided into three group (defined as subdataset) of 10^6 iteration each. Then, the SDs of the resulting distribution of longitudinal strain, bending direction angle and curvature were determined considering the 3 subdatasets as well as the entire dataset, which consists of the three subdatasets (in other word all the data of the simulation), and a comparison was drawn to prove the statistical significance of the simulation.

4.5.2 Input and output of the simulations:

45 simulations with $3 \cdot 10^6$ trials were carried out for each fiber geometry.
The inputs of the simulations were

1) Geometrical features of the section:
    a. Section geometry;
    b. Core spacing;
    c. Core position error normal frequency distribution with a certain SD.
2) State of deformation of the section (coefficients of the strain plane equation), which are the shape sensor's output measures:
    a. Longitudinal strain;
    b. Curvature;
    c. Bending direction angle.

The outcomes of the simulations are:

1) Frequency distribution of longitudinal strain;
2) Frequency distribution of curvature;
3) Frequency distribution of bending direction angle.

4.5.3 Sensor section geometry

The sensor section geometry, particularly the position and the number of the cores, has a considerable impact on the precision of the measured longitudinal strain, bending direction and curvature.

The multicore fibers available nowadays and suitable for shape sensing applications are lamentably limited, as, generally, they are the same produced for telecommunication applications. Their diameter is very small (regularly about 125 μm) and the core spacing is normally between 30 and 50 μm [50,53,84,92,133,172,173]. Manufacturing different MCF geometries for sensing purposes would be prohibitively expensive, considering that the sensors market is limited compared to the telecommunications one.

Since better accuracy can be achieved by increasing the core spacing, although less compact, optical shape sensors consisting of multiple optical fibers fastened to a support have been developed [126,128].

This study considered three of the most widely employed fiber geometries in sensing applications (see Fig. 4.13): a three- [50,128,133], four- [53,84,114,126,172] and seven-core section [91–93,95,111,174], with constant angular spacing and equal distance between the outer cores and the sensor axis, including 5 distinct core spacings: 30, 50, 70, 140 and 300μm.

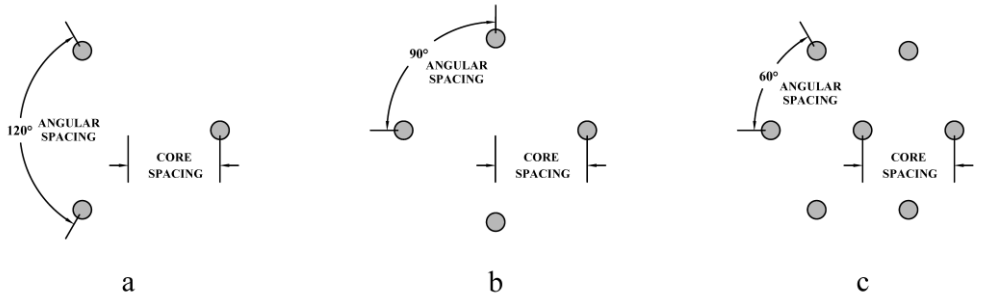

Fig. 4.13. (a) Three-core section geometry; (b) Four-core section geometry; (c) Seven-core section geometry.

4.5.4 Core position simulation errors

The core position error distribution in fiber optic sensors was modeled by the Monte Carlo method with 15 simulations and $3 \cdot 10^6$ iterations for each geometry. Three different standard deviations (SD) were considered to characterize the 3D standard normal distributions (the Gaussian probability distributions were the simulation inputs) of the errors and five distinct core spacings (distance between the sensor axis and the external cores).

By way of example, the 3D Gaussian frequency distribution of the core position for a seven-core geometry is shown in Fig. 4.14.

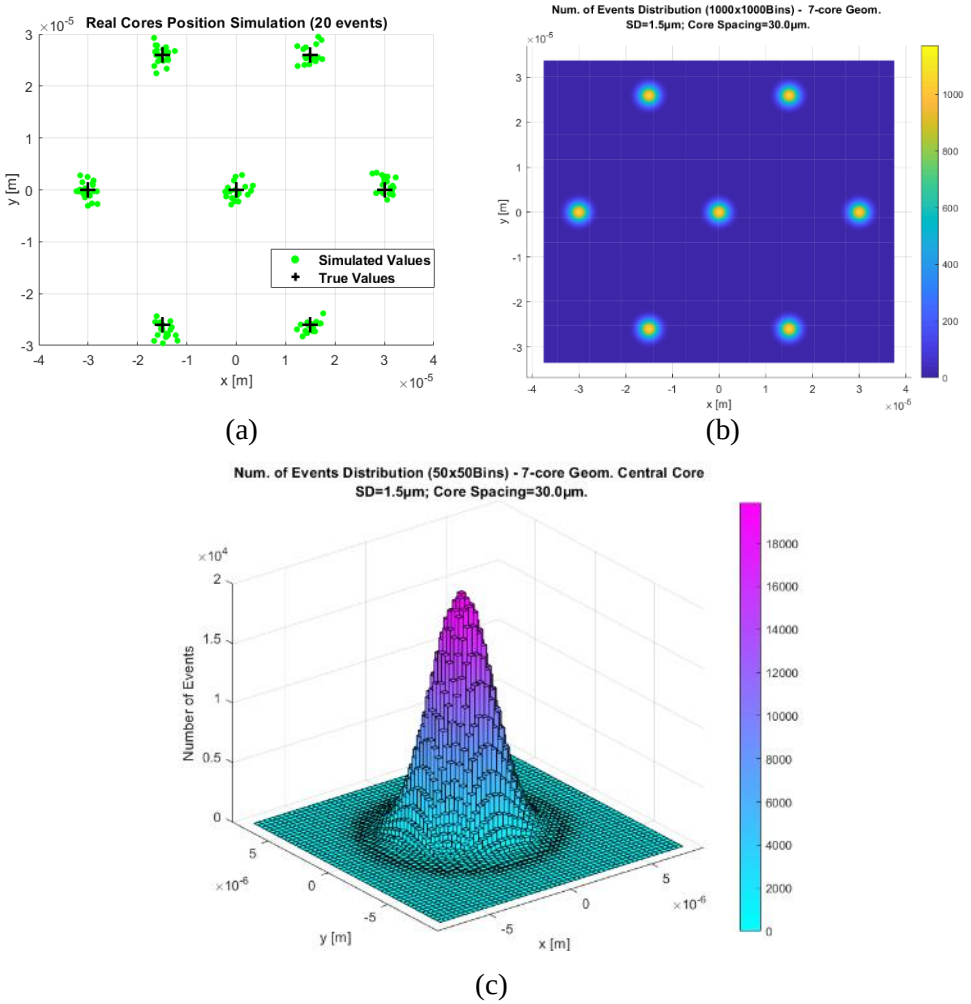

Fig. 4.14. (a) Real core position simulation of 7-core shape sensor (20 events; SD core position = 1.5 μm; Core spacing = 30 μm); Core position 3D frequency distribution (3·106 events; SD core position = 1.5 μm; Core spacing = 30 μm) of a 7-core shape sensor, considering (b) all the seven cores; (c) only the central core [175].

4.5.5 Strain calculation

After generating the 3D frequency distribution of core positions, the input of the simulation and the distribution of the strain sensed by each core can be calculated, by considering a certain state of deformation of the section and assuming that the uncertainty in strain sensing only depends on core position imprecision. The state of deformation can be defined by means of longitudinal strain, bending direction angle and curvature, ε^{long}, α and $|\kappa|$.

The strain sensed by a certain core in each iteration is the sum of two components: the longitudinal strain (average strain of the section) and the bending strain (see Eq. 4.5). The bending strain can be calculated as the shortest distance from the core to the neutral axis multiplied by the magnitude of the strain function gradient (curvature magnitude). The distance from the neutral axis is the abscissa of the point in a Cartesian coordinate system obtained by rotating the *x* and *y* axes counter clockwise through an angle α (see Fig. 3.7 of Chapter 3).

$$\varepsilon_i^j = \varepsilon^{long} + |\kappa| \left[x_i^j \cos\alpha + y_i^j \sin\alpha \right] \tag{4.5}$$

where *i* represents the core considered and *j* the iteration.

Fig. 4.15 shows the frequency distributions of the strain generated due to core position errors with an SD of 0.8 μm in the cores of a four-core sensor with core spacing of 30 μm when the measured curvature is 40 m^{-1} (2.5 cm radius of curvature).

It should be noted that the strain distributions are still Gaussian and that the SD may be much higher than the strain resolution of commercial OFS, which can reach a few microstrains, in the case considered it is 32 με.

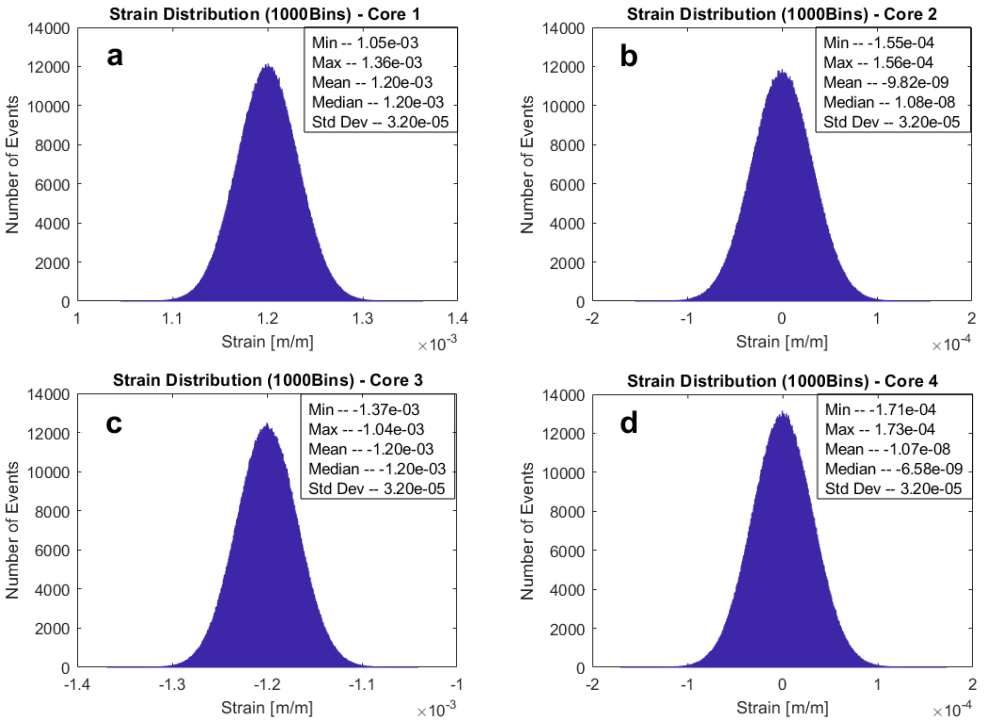

Fig. 4.15. Strain frequency distribution (3·106 events; SD core position = 0.8μm; Core spacing = 30 μm; Measured curvature = 40.0 m-1) of a 4-core shape sensor simulated in (a) Core 1; (b) Core 2; (c) Core 3; (d) Core 4.

4.6 Case of study 2 - Results of the analyses

The outcomes of the experiments are presented this Section.

4.6.1 Longitudinal strain distribution

Fig. 4.16 shows an example of the distributions generated in a three-core sensor with core spacing of 30 μm due to core position errors with an SD of 0.8 μm, when the longitudinal strain, the bending direction angle and the curvature (inputs of the simulation) are respectively, 0.0 μm, 0.0 rad and 40 m^{-1}.

The resulting frequency distributions are clearly Gaussian and the mean values of the distributions coincide with the input of the simulation, showing that the model is well constructed and the number of iterations in the simulation is sufficient.

The propagation law of core position errors can thus be defined by considering only the SD of the distributions obtained in the simulation.

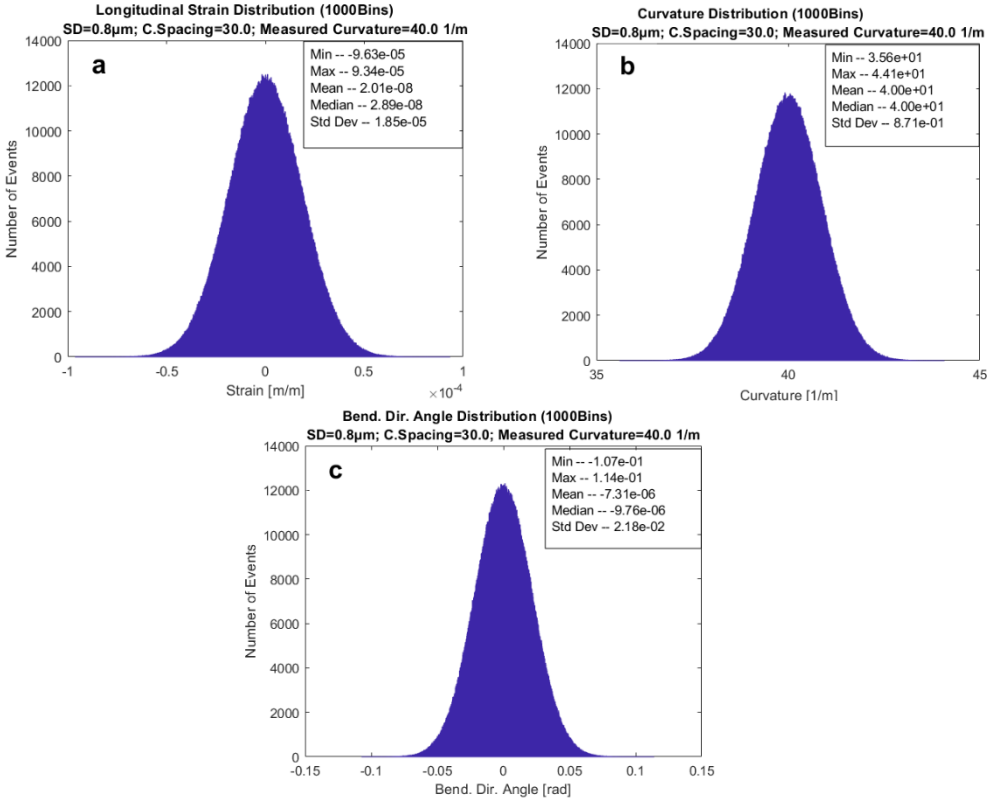

Fig. 4.16. Frequency distribution of (a) longitudinal strain, (b) curvature and (c) bending direction angle of a 3-core shape sensor (3·106 events; SD core position = 0.8 μm; Core spacing = 30 μm; Measured curvature = 40.0 m-1).

4.6.2 Simulation results

As the error distribution depends on the slope of the strain plane, the measured longitudinal strain has no influence on the simulation results. In fact, when there is no bending and the strain plane is parallel to the *xy* plane, the SD of the resulting distribution is null and the bending direction angle is not defined. In the same way, bending direction angle does not influence the resulting distributions, since it depends on the arbitrarily defined Cartesian coordinate system, being the angle between the *x* axis and the bending direction. These two parameters were thus set equal to zero in the simulations.

During the simulations it was found that the SD of the core position error distributions and the measured curvature have a linear influence on the phenomenon, whereas core spacing affects it nonlinearly. Three different measured curvatures and standard deviations (SD) of core position distribution along with five values of core spacings were thus considered in the study, as reported in Table 4.11.

The results of the simulations for three-core, four-core and seven-core geometries are listed in Appendix A-C.

Table 4.11. Inputs of the simulations.

Section Geometrical Features			**Strain Plane Coefficients**		
Section Geometry	**Core Spacing [μm]**	**SD Core Position Distr. [μm]**	**Measured Longitudinal Strain [με]**	**Measured Bend. Dir. Angle [rad]**	**Measured Curvature [1/m]**
Three-core	30.00 50.00	0.20	0.00	0.00	0.10
Four-core	70.00	0.80			5.00
Seven-core	140.00	1.50			40.00
	300.00				

4.6.3 Statistical significance test

As previously explained (Section 4.2.3), MCM needs a stopping rule to define the number of iterations of the simulations (sample size). As the appropriate sample size necessary for steady outcome cannot be theoretically calculated [168], beforehand, it was opted for $3 \cdot 10^6$, which in most cases seem to be satisfactory [163]. To verify the correctness of the assumption, for each simulation, a comparison was drawn between the standard deviations of the distributions obtained from the total dataset and the 3 subdatasets with 10^6 trials each.

The percentage error between the SDs of the subdatasets and the total dataset was determined by Eq. 4.6:

$$E = [(SD^T - SD^S)/SD^T]100 \tag{4.6}$$

where E is the percentage error and the standard deviation of the total dataset and the subdataset are respectively SD^T and SD^S. The highest value of percentage error considering all the simulations of this study is, in absolute terms, 0.198, proving the statistical significance of the simulations.

4.6.4 Curve Fitting Models

The relation between the SD of the frequency distribution of longitudinal strain, bending direction angle and curvature (dependent variables) and SD of the frequency distribution of core position errors, measured curvature and core spacing (independent variables) were identified with two variable curves using the Curve Fitting MATLAB® [170] Toolbox™. A sequence of three models (one for each dependent variable) were calibrated for each section geometry, fitting the results of the simulations, to identify the propagation law of core position uncertainty, determine the mathematical relationship between the considered variables and make the research outcomes more fruitful and user-friendly. The coefficient equations were estimated by a nonlinear regression analysis, based on the errors, including the Coefficient of Determination (R^2), Root-Mean-Square Error (RMSE) and Sum of Squared Errors (SSE):

$$R^2 = 1 - \frac{\sum_i (t_i - o_i)^2}{\sum_i (o_i)^2} \tag{4.7}$$

$$RMSE = \sqrt{\frac{1}{n}\sum_i (t_i - O_i)^2} \tag{4.8}$$

$$SSE = \sum_i (t_i - O_i)^2 \tag{4.9}$$

where t_i is the target value, O_i is the predicted value, and n is the number of data.

The first parameters identified were those that influence the standard deviation of the frequency distribution of longitudinal strain, bending direction and curvature. The curvature frequency distribution was found to be influenced by all three parameters, while core spacing did not influence the longitudinal strain distribution SD, nor did bending direction angle frequency distribution depend on the measured curvature.

The model equations were thus defined *a priori* and their performance, based on the errors, investigated *a posteriori*. In all cases, it was found that one coefficient was enough to efficiently fit the data.

The function that represents the dependence between longitudinal strain distribution SD and core position SD and measured curvature (see Eq. 4.10) was fitted with the

coefficient k_1. Fig. 4.17 shows the surface fitting for the three-core section, by way of example.

Likewise, the function that defines the bending direction angle SD in terms of core position SD and core spacing (see. Eq. 4.12) was determined using the coefficient k_3, as shown in Fig. 4.18.

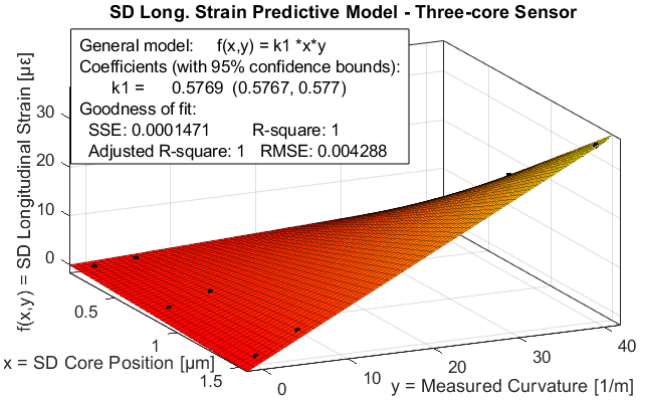

Fig. 4.17. Longitudinal strain SD curve-fitting for a three-core sensor [175].

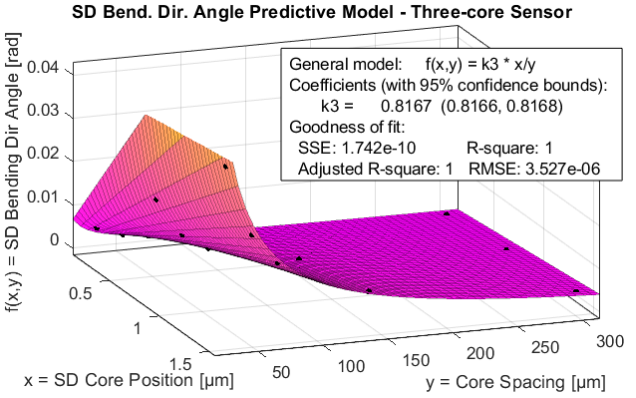

Fig. 4.18. Bending direction angle SD curve-fitting for a three-core sensor [175].

In the case of the curvature distribution SD, a four-variable curve was required to fit the data (Eq. 4.11) with the coefficient k_2. Hence, three distinct curves (see Eq. 4.13-4.15), with one coefficient and three variables each, were calibrated at constant values of measured curvature, 0.1, 5.0 and 40.0 m^{-1}. The value of k_2 was then determined by a linear regression analysis considering the coefficients of the three aforementioned curves. Fig. 4.19 shows, the surface fitting and linear regression of the three-core section geometry.

$$SD\varepsilon^{long} = \boldsymbol{k_1}\,(SDcp \times |\kappa|) \tag{4.10}$$

$$SD|\kappa| = \boldsymbol{k_2}\ (SDcp \times |\kappa|/r) \tag{4.11}$$

$$SD\alpha = \boldsymbol{k_3}\ (SDcp/r) \tag{4.12}$$

$$SD|\kappa|(|\kappa| = 0.1) = \boldsymbol{k'_2}\ (SDcp/r) \tag{4.13}$$

$$SD|\kappa|(|\kappa| = 5.0) = \boldsymbol{k''_2}\ (SDcp/r) \tag{4.14}$$

$$SD|\kappa|\ (|\kappa| = 40.0) = \boldsymbol{k'''_2}\ (SDcp/r) \tag{4.15}$$

where SDcp, SDεlong, SD|κ| and SDα are respectively the standard deviation of normal frequency distribution of core position errors in μm, longitudinal strain in με, curvature in m-1 and bending direction angle in rad, r is the core spacing in μm (distance between the sensor axis and the outer cores), |κ| is the measured curvature in m-1 and k1, k2, k3, k'2, k''2 and k'''2 are the curves coefficients.

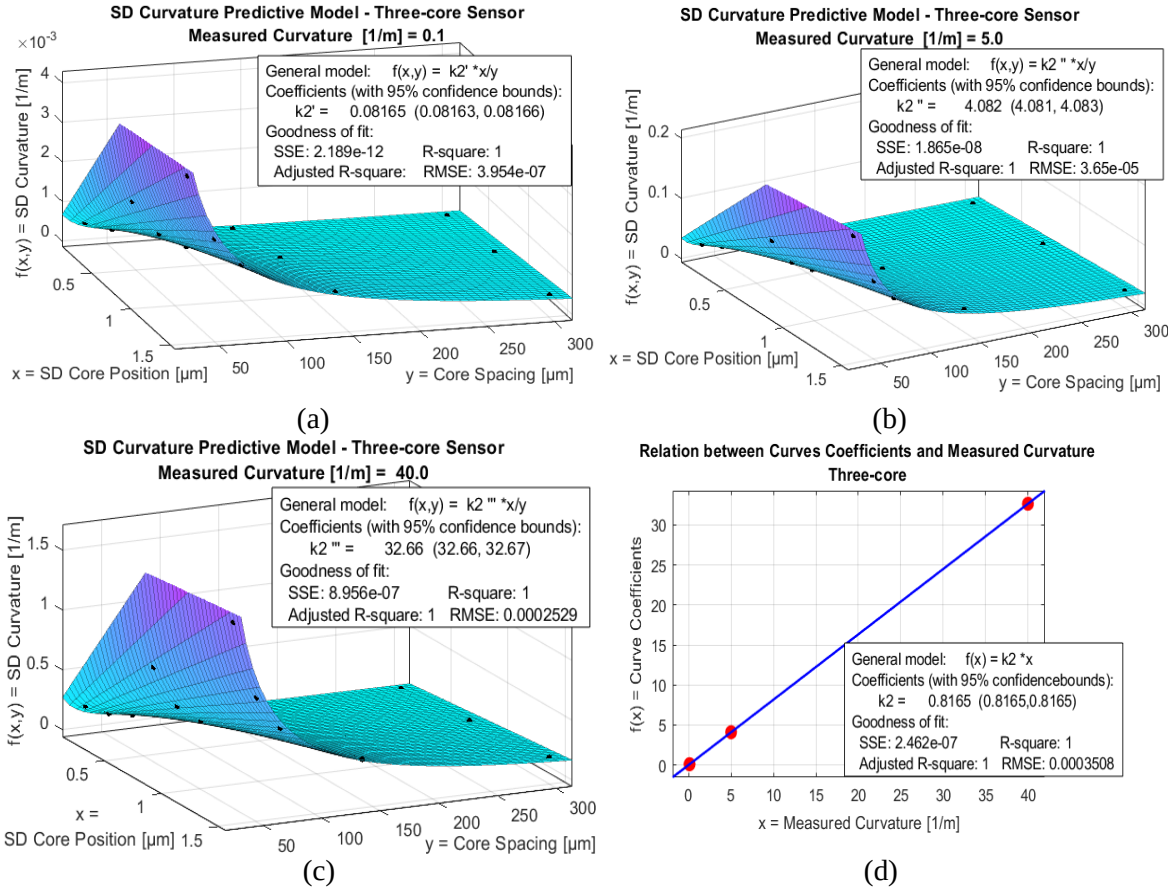

Fig. 4.19. Curvature SD curve-fitting for a three-core sensor with measured curvature of (a) 0.1 m-1; (b) 5.0 m-1; (c) 40.0 m-1; (d) Relationship between the curve coefficients and measured curvature [175].

The curves coefficients for the different section geometries and the results of nonlinear regression analysis that measures the goodness of fit are listed in the Table 4.12:

Table 4.12. Results of the curve fitting analysis for the three different section geometries in the following order: first 3-core, second 4-core and third 7-core.

Function Equation	f(x,y)	Coef	Coef. Value	R^2	RMSE	SSE
$f(x,y) = k_1 x y$	SD ε^{long}	k_1	0.57690	1.000000	0.004288	0.000147
$f(x,y) = k_2' x / y$	SD $\|\kappa\|$ ($\kappa = 0.1$)	k_2'	0.08165	1.000000	0.000000	0.000000
$f(x,y) = k_2'' x / y$	SD $\|\kappa\|$ ($\kappa = 5.0$)	k_2''	4.08200	1.000000	0.000037	0.000000
$f(x,y) = k_2''' x / y$	SD $\|\kappa\|$ ($\kappa = 40.0$)	k_2'''	32.66000	1.000000	0.000253	0.000000
$f(x,y) = k_2 x$	$k_2' k_2'' k_2'''$	k_2	0.81650	1.000000	0.000351	0.000000
$f(x,y) = k_3 x / y$	SD α	k_3	0.81670	1.000000	0.000004	0.000000
$f(x,y) = k_1 x y$	SD ε^{long}	k_1	0.50000	1.000000	0.001380	0.000015
$f(x,y) = k_2' x / y$	SD $\|\kappa\|$ ($\kappa = 0.1$)	k_2'	0.07071	1.000000	0.000000	0.000000
$f(x,y) = k_2'' x / y$	SD $\|\kappa\|$ ($\kappa = 5.0$)	k_2''	3.53600	1.000000	0.000021	0.000000
$f(x,y) = k_2''' x / y$	SD $\|\kappa\|$ ($\kappa = 40.0$)	k_2'''	28.28000	1.000000	0.000207	0.000000
$f(x,y) = k_2 x$	$k_2' k_2'' k_2'''$	k_2	0.70700	1.000000	0.000702	0.000000
$f(x,y) = k_3 x / y$	SD α	k_3	0.70720	1.000000	0.000003	0.000000
$f(x,y) = k_1 x y$	SD ε^{long}	k_1	0.37790	1.000000	0.004876	0.000190
$f(x,y) = k_2' x / y$	SD $\|\kappa\|$ ($\kappa = 0.1$)	k_2'	0.05774	1.000000	0.000000	0.000000
$f(x,y) = k_2'' x / y$	SD $\|\kappa\|$ ($\kappa = 5.0$)	k_2''	2.88600	1.000000	0.000026	0.000000
$f(x,y) = k_2''' x / y$	SD $\|\kappa\|$ ($\kappa = 40.0$)	k_2'''	23.10000	1.000000	0.000142	0.000000
$f(x,y) = k_2 x$	$k_2' k_2'' k_2'''$	k_2	0.57750	1.000000	0.001052	0.000002
$f(x,y) = k_3 x / y$	SD α	k_3	0.57740	1.000000	0.000005	0.000000

It should be noted that Eqs. 4.11 and 4.12 can be applied not only to multicore sensors and Optical Fiber Bundle sensors, in which the typical values of core position SD and core spacing are included in the range examined, but also to multiple single-core optical fiber sensors with a higher standard deviation of core position error distribution and core spacing, such as optical inclinometers. In fact, in this last case, the section geometries generally are the same as the one analyzed in this research [126,128]. Besides, the typical values of core position SD and core spacing are a few millimeters or tenths of millimeter and some tens of millimeters, which means that the ratio between these two parameters, which is what enters in the equations, is still inside the range studied (it can easily be verified converting the millimeters into micrometers and substituting the terms into the equations of the predictive models).

Furthermore, since the model coefficients represent the intensity of error propagation (no error propagation when the coefficients are null), there is an interesting improvement in the uncertainty propagation associated with more cores than those in the three-core section, which has the minimum number required for shape sensing. Table 4.13 shows the percentage reduction in the coefficients of the four-core and seven-core sections compared to the three-core geometry. As mentioned in Section 2, the presence of the central core only affects the accuracy of the longitudinal strain calculation (coefficient k_1), while the seven-core section behaves like a six-core in the other cases.

A good example of application of the predictive models may be the development of optical curvature sensor (optical multicore fiber or optical multi-fiber) for bending of wing aircraft monitoring. As all the engineering applications, it is known the measuring range, taking into consideration what the minimum detectable curvature and the maximum acceptable curvature to avoid damages are, and the required accuracy. Hence, considering the geometrical features of fibers available in the market, it is possible to calculate the uncertainty arising from core position errors, check what of the available fibers fit the requirements and if the errors are acceptable, taking into account that core position errors are not the unique source of errors, which has to be considered [166].

Table 4.13. Comparison in terms of the percentage reduction of the model coefficients between the three-core section and the four-core and seven-core sections.

Coefficient	Four-core geometry	Seven-core geometry
k_1	13.3299	34.4947
k_2'	13.3987	29.2835
k_2''	13.3758	29.2994
k_2'''	13.4109	29.2713
k_2	13.4109	29.2713
k_3	13.4076	29.3008

Fig. 4.20 shows the reduced error propagation, in terms of coefficient percentage, with different numbers of cores.

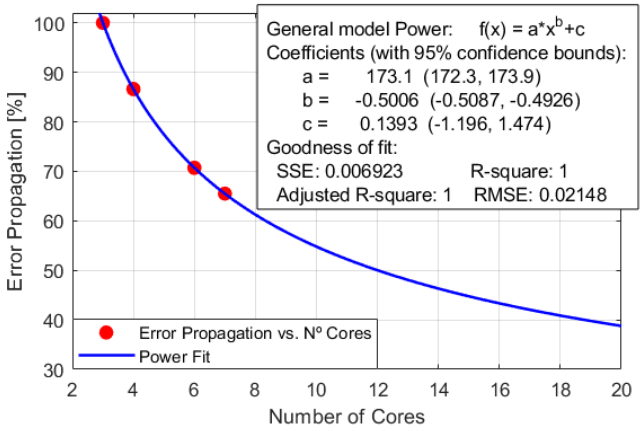

Fig. 4.20. Variation of propagation errors with number of cores [175].

4.6.5 Concluding remarks

The results presented above leads to following conclusions:

- Strain plane calculation through Sum of Squared Errors minimization is a valid approach to deal with different shape sensors section geometries, even when there are section asymmetries.
- The MCM is a potent technique for modeling the propagation of core position errors in computing longitudinal strain, bending and direction curvature.
- The core position SD has a linear influence on the frequency distribution of longitudinal strain, bending direction angle and curvature (Section 4.6.4).
- The SDs of the bending direction angle and curvature distributions strongly depend on core spacing through an inverse relationship, whereas there is no relationship between longitudinal strain SD and core spacing (Section 4.6.4).
- The curvature measured has no influence on bending direction angle, but linearly influences the curvature and longitudinal strain SD, so that in these cases the sensor accuracy is related not only to aspects of product design, but also to the application (Section 4.6.4).
- Increasing the number of cores remarkably improves the power-function relationship (Table 4.13 and Fig. 4.20).

The study shows the important role of core position errors, although, lamentably, manufacturers do not normally provide information on this aspect. The outcomes successfully identify the propagation laws of core position uncertainty and show the considerable influence of number of cores, core spacing and measured curvature on shape sensor accuracy. The resulting predictive models can support user choices and help manufacturers to identify the parameters that need to be changed to achieve better performance. For example, improving the manufacturing process for higher

precision in core positioning, larger core spacing, including more cores, or the performance achievable through different sensor designs.

It has to be pointed out that, even though this study was focused on errors that affect the performance of multicore fiber shape sensors, the resulting research findings can be applied to both multiple single-core optical fibers sensors equipped with distributed or quasi-distributed strain-sensors, or to shape-sensing arrays in general.

4.7 Errors propagation in shape sensing

Although, this study has investigated only the propagation on curvature and bending direction angle calculation, it is easy to understand that the uncertainty considered in this Chapter have direct influence on the errors in shape reconstruction. Nevertheless, the determination of the mathematical relationships between the SD of core position and strain measurement errors and the shape sensing uncertainty is an extremely difficult task and massive workload, since it should take into consideration all the possible combination of sensor shape (the geometry of the curve sensed and the gradients of curvature) and sensor characteristics (number of FBGs or spatial distance between them). Therefore, it was not conducted in this work, whereas an *ad hoc* study should be carried out for each specific application, considering the methodology here presented.

By way of example, Fig. 4.21 shows the simulation of propagation of the core position errors on shape reconstruction of circular helix.

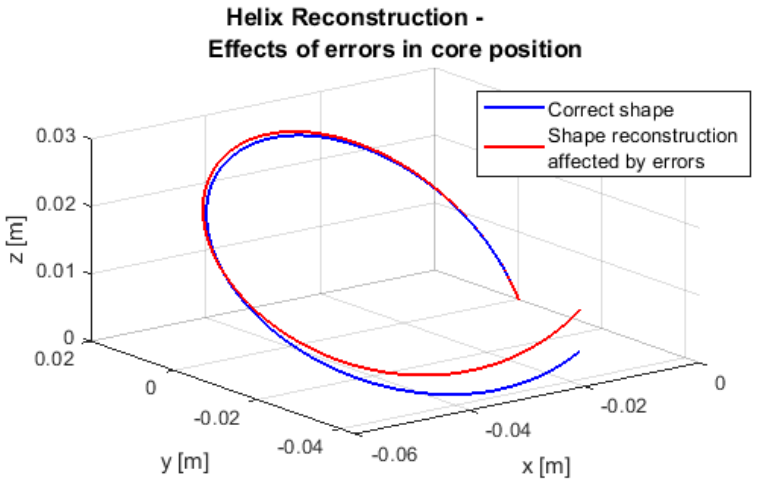

Fig. 4.21. Simulation of the propagation of the core position errors on the reconstruction of the shape of a circular helix with curvature = 33.333 m^{-1} and torsion = 6.667 m^{-1} (Characteristics of the sensor: number of cores = 7; core spacing = 35 µm; number of FBGs = 6; distance between the FBGs along the fiber length = 3 cm; core position errors SD = 0.8 µm)

4.8 Conclusions

This Chapter analyzed the errors of optical multicore fiber shape sensors and presented a series of predictive models to evaluate the impact of several parameters on the performance of these sensors.

The measurement process and uncertainty propagation were simulated using the Monte Carlo method with more than 1 million iterations per simulation. Afterwards, a test of statistical significance was carried out to verify the results of the simulations. Finally, the performance of MCF-base shape sensors was assessed considering the uncertainty in measuring three-dimensional curvature (in terms of standard deviation of the frequency distributions of curvature magnitude and bending direction angle), the basis for the process of shape reconstruction. The analysis was articulated in two parts:

I) Study of the effects of strain measurement uncertainty, which represents the resolution of the interrogation system, taking into account the influence of core spacing and measured curvature;
II) Study of the effects of core position errors, which are due to the manufacturing defects, taking into consideration the influence of core spacing, measured curvature and number of cores.

It has appeared that the accuracy in the determination of the three-dimensional curvature remarkably improves with the decrease of strain measurement and core positioning errors. Moreover, it has been identified the role played by core spacing and number of cores that have significant beneficial effects, as the uncertainty propagation diminishes at increasing values of both parameters.

To conclude, the mathematical relationships between the variables considered were determined and several predictive models were calibrated by fitting the results of the simulations. These models are efficacious instruments for the evaluation of the performance of these sensors and a valid support for the design of new fiber-optic-based shape sensors.

CHAPTER 5

INFLUENCE OF STRAIN SENSOR LENGTH

5.1 Introduction

Several interrogation techniques have been employed to perform shape sensing using continuous and homogeneous optical multicore fibers. Among them, the most relevant are: Optical Frequency Domain Reflectometry (OFDR) based on Rayleigh scattering [92], Brillouin Optical Time Domain Reflectometry [95] and Fiber Bragg Gratings interrogated using Wavelength Division Multiplexing (WDM) analysis [54,93,143,151,152,156,157]. The last one is, by far, the most widely used. The most important reasons behind such predominance are dual:

I. The low-cost of the interrogators based on WDM analysis;
II. The capability of WDM-based interrogators to achieve high-speed data acquisition (order of kHz, while their counterparts only reaches few Hz), which make them attractive for a number of dynamic applications.

On the other hand, when using WDM interrogation systems, the number of the sensors that is possible to read in one fiber is limited to few tens of gratings, notably less of thousands of gratings, which an Optical Frequency Domain Reflectometry (OFDR) can interrogate [176], despite the higher uncertainties [177].

In the light of the above, it is crucial to improve the efficiency of every single FBGs in order to enhance the accuracy of optical shape sensing based on FBG sensor and WDM interrogator, at equal number of strain sensors or better FBG density.

This Chapter reports on an experimental study carried out to identify the influence of FBG length on optical shape sensor performance at equal FGB density.

5.2 FBG-based shape sensors fabrication

The shape sensors were assembled in the Institute of Telecommunications and Multimedia Applications (iTEAM) of the *Universitat Politècnica de València* (UPV) by inscribing four FBGs with a length of 1.5 mm and 8.0 mm (equally spaced along a length of 45mm) in a commercial seven-core MCF from Fibercore Ltd. [94]. The fiber had a cladding diameter of 124.5μm and seven cores with doubly symmetric configuration (see Fig. 5.1): one central core and six external cores equidistant from the fiber axis (core spacing 35 μm) and 60º of angular spacing. Each core had a mode field diameter of 6.4 μm and a numerical aperture of 0.2.

Fig. 5.1. Seven- core MCF cross section [94]

In order to enhance photosensitivity, the fiber optic was hydrogen loaded for two weeks at ambient temperature and a pressure of 20 bars. The phase-mask method [104] was used to inscribe the fiber Bragg gratings by a 244 nm CW frequency-doubled argon-ion laser with 60 mW output power. The spectrum of the central core of both sensors is shown in Fig. 5.2.

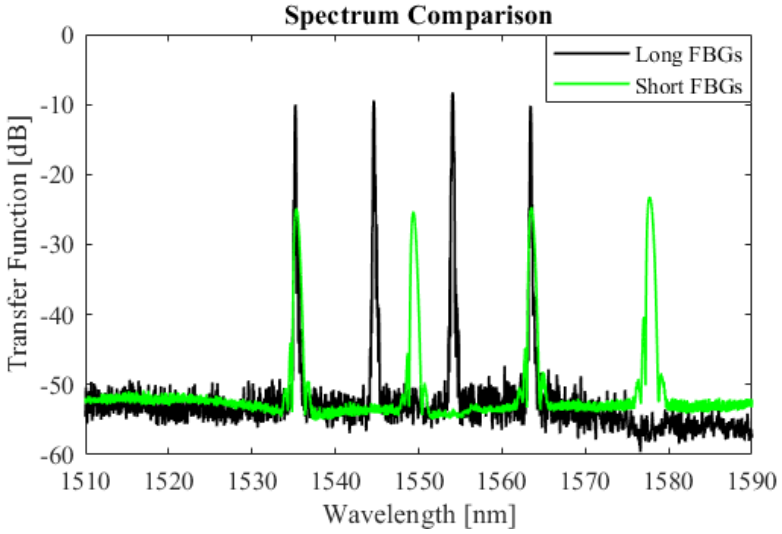

Fig. 5.2. Spectrum comparison of the two sensors with long and short FBGs [178].

5.3 Experimental setup

In order to test sensor performance, an experimental setup was designed to ensure accurate readings. An aluminum mold was made on a high-precision computer numerical controlled (CNC) machine with a maximum positioning error of a few tens of micrometers to ensure the marginal influence of fiber positioning errors on shape reconstruction accuracy. The mold (see Fig. 5.3) consisted of a plate with five

engraved semicircles with radii of 55, 50, 45, 40 and 35 mm, for Tests1 to 5, respectively.

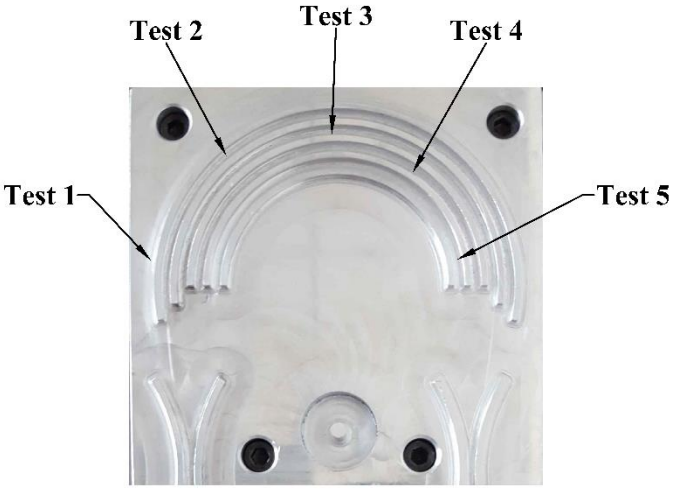

Fig. 5.3. Shape-sensing mold [178].

The fibers were placed around each of the semi-circles on the mold, from the lowest to the highest curvature, and stretched along the semicircles using two multi-axis stages for nano-positioning, interrogated by a Static Optical Sensing Interrogator (sm125) combined with a Channel Multiplexer (sm041) (Micron Optics). The experimental setup can be seen in Fig. 5.4.

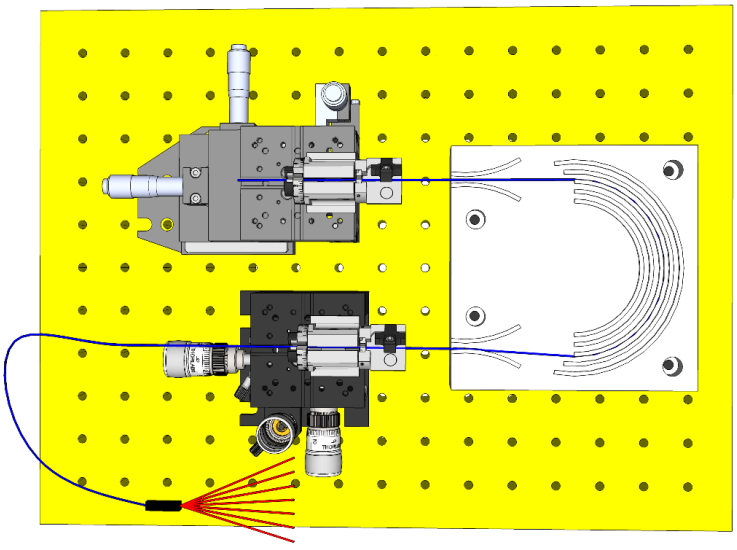

Fig. 5.4. Experimental setup [179].

5.4 Results and discussion

5.4.1 Strain sensing results

Since the local bending in each instrumented section was calculated from the strain sensed by the cores, the repeatability and precision of the MCF strain sensors were first assessed by tracking the FBG peaks simultaneously in all seven cores at a constant temperature for two minutes at an acquisition rate of 0.5 Hz. The shift in the FBG wavelength was then converted into strain by dividing the wavelength shift by a gauge factor value equal to 1.2 microstrain/pm, obtained from different tensile tests in accordance with [180]. The measured strain values followed a normal distribution. Their standard deviations (SD) are reported in Table 5.1.

Table 5.1. Comparison of the normal strain distribution SDs detected by MCF shape sensors.

Standard Deviation of Strain Measurements [με] - Test 1								
Core	1	2	3	4	5	6	7	
FBG 1	0.4911	0.6175	0.5673	0.5437	0.5616	0.6042	0.6095	**Long FBGs**
FBG 2	0.6126	0.6045	0.5823	0.5400	0.4553	0.4629	0.5776	
FBG 3	0.4590	0.7009	0.8630	0.6308	0.6439	0.4951	0.5001	
FBG 4	0.5586	0.6590	0.7115	0.6467	0.5339	0.6587	0.5356	
FBG 1	1.7457	2.0023	1.9268	1.6449	1.6916	2.3905	1.7643	**Short FBGs**
FBG 2	2.3445	1.8208	1.6640	2.5776	1.6821	2.0045	1.8354	
FBG 3	1.9885	1.6443	2.3988	2.5314	3.0691	1.7810	1.3503	
FBG 4	1.5843	1.5292	2.0616	2.6288	2.2684	2.0137	1.9562	

The strain distribution SDs were mostly homogeneous in all the sections and cores of both sensors and were strongly affected by grating length. In fact, those of the short FBGs were three or four times higher than those detected by the long FBGs.

Strain detection precision depends on the accuracy of the interrogation system, which is related to the resolution of the read-out of the reflected wavelengths, peak tracking technique [181], FBG spectrum and the noise signal.

5.4.2 Curvature sensing results

Curvature was calculated from the bending strain, which is the difference between the strain measured in the straight and bent sensors. To calculate the bending strain, the FBG wavelength peaks were initially detected in the straight sensors and then the peaks shifts were tracked in the curved fibers. The wavelength peak shifts were

converted into strain by dividing them by the gauge factor, while the curvature was calculated from Eqs. 6 and 7.

Although the peak shifts are influenced by the longitudinal strain due to axial loading and temperature variation, no compensation was necessary since the longitudinal strain affects all the cores equally and therefore has no influence on the slope of the bending strain plane, on which the curvature depends.

Once again, the results of the long-FBG-based MCF are considerably better. The sources of errors in the case of curvature sensing are diverse and include the resolution of the interrogation system and inaccuracy in the geometry of the sensor and in the sensor positioning [152,166,175]. Table 5.2 lists the curvature detected by both sensors in the five tests.

Table 5.2. Comparison of curvature values detected by two MCF shape sensors.

	Test 1	**Test 2**	**Test 3**	**Test 4**	**Test 5**	
Curvature [1/m]	*18.1818*	*20.0000*	*22.2222*	*25.0000*	*28.5714*	
Section 1	18.3154	19.7832	22.3003	24.7801	28.3600	**Long FBGs**
Section 2	17.9226	20.0031	21.9657	25.1781	28.3339	
Section 3	18.5390	19.8496	22.7328	25.3513	28.4611	
Section 4	17.8365	20.0638	22.3428	24.9200	28.5443	
Average Value	18.1534	19.9249	22.3354	25.0574	28.4248	
Average Error	-0.0284	-0.0751	0.1132	0.0574	-0.1466	
St. Deviation	0.2867	0.1131	0.2720	0.2217	0.0838	
Section 1	17.8974	19.6786	21.5104	25.4391	28.6197	**Short FBGs**
Section 2	18.2177	19.8971	21.9127	24.5911	28.6836	
Section 3	18.0101	19.6753	22.5028	25.3401	28.6064	
Section 4	19.1247	21.2615	23.7737	25.7340	30.0321	
Average Value	18.3125	20.1281	22.4249	25.2761	28.9854	
Average Error	0.1306	0.1281	0.2027	0.2761	0.4140	
St. Deviation	0.4828	0.6605	0.8550	0.4212	0.6050	

5.4.3 Shape sensing results

The shape of the fiber-optic sensors was reconstructed by using the procedure explained in Chapter 3. As it was not possible to calculate the torsion function, because the fiber was neither spun nor fastened to the mold, and, hence, it was impossible either to calculate the torsional strain and compensate the fiber twisting or to avoid it (as it will be illustrated in Chapter 6), 2D shape sensing was performed. An algorithm was developed in Mathematica code [182] for the linear interpolation of the curvature function $\kappa(s)$, based on the curvature calculated in the instrumented sections, and to reconstruct the 2D shape of the of MCF arrays through numerical integration of the Frenet-Serret equations (Eq. 3.16). Fig. 5.5 shows the shapes of the two fiber optic sensors, which were sensed, while the fibers were stretched along the semicircles on the mold (see Fig. 5.3).

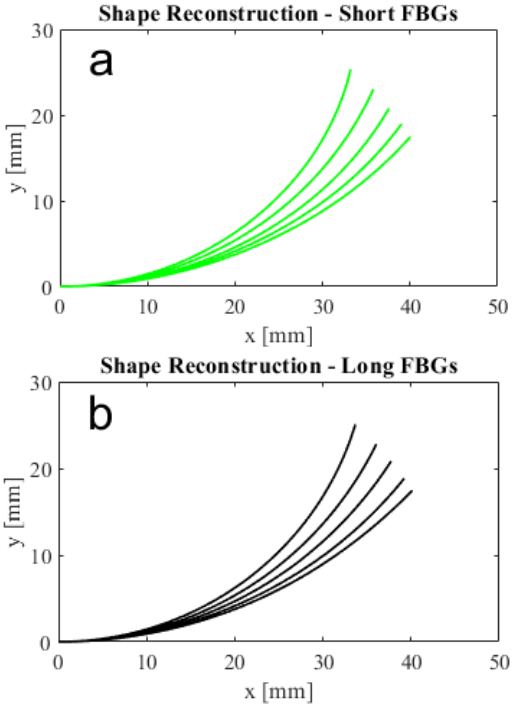

Fig. 5.5. Reconstructed shape of MCF sensors by (a) short FBGs and (b) long FBGs [178].

In order to evaluate the shape sensors performance, the shape reconstruction errors were determined (considered as the distance between the exact position of the fibers and the reconstructed shape position) (see Fig. 5.6).

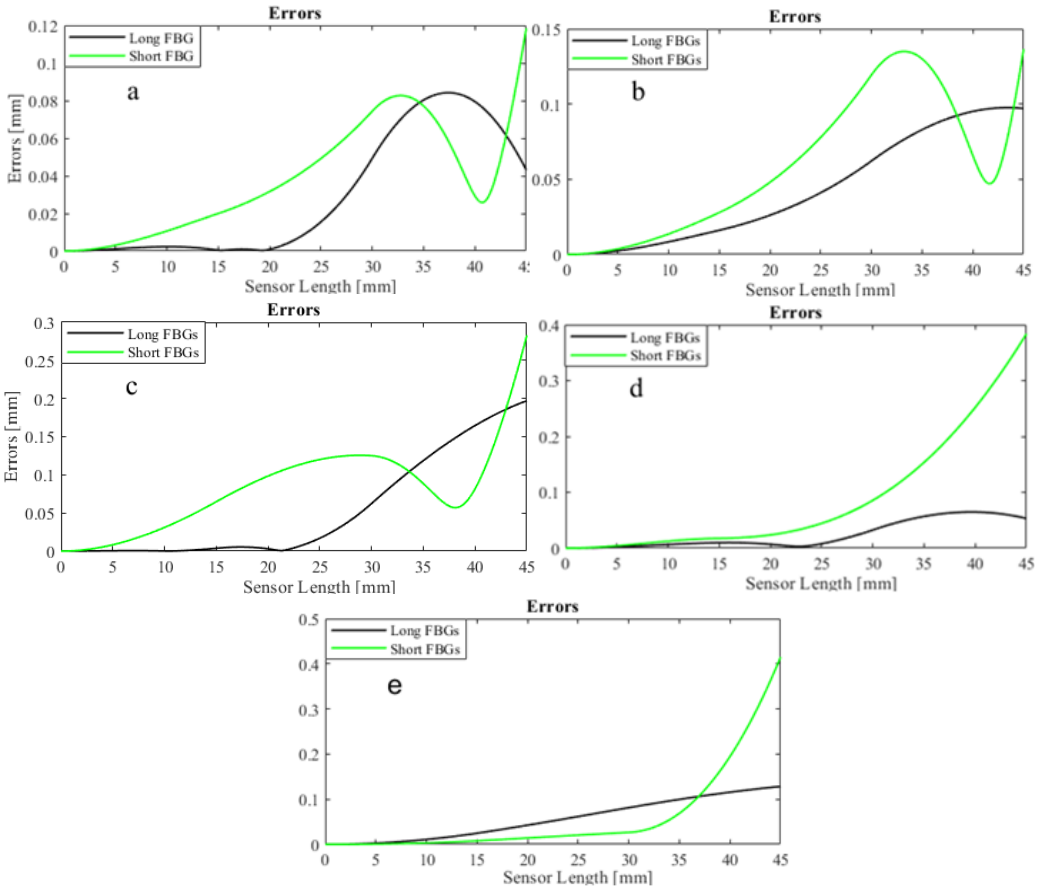

Fig. 5.6. Shape reconstruction errors of two MCF shape sensor arrays in (a) Test 1; (b) Test 2; (c) Test 3; (d) Test 4; (e) Test 5 [178].

As in the previous cases, the errors obtained with multicore sensors based on short FBGs are significantly greater, meaning that the strain and curvature sensing errors propagate and affect shape reconstruction, the sources of errors being, in fact, the same discussed in the previous sections. The largest long FBG errors are between 0.05 and 0.20 mm (0.11% and 0.44% of sensor length), while those of the short FBG sensors are several times greater, i.e. between 0.12 and 0.41 mm (0.26% and 0.91% of sensor length) and vary much more widely.

5.4.4 Discussion

Two optical MCF shape sensors were assembled by inscribing long (8.0mm) and short (1.5mm) FBGs in commercial 7-core fiber. All the necessary steps for shape reconstruction were traced, including strain sensing, curvature calculation and shape integration, and sensor performance was compared at each stage.

The optical MCF sensor based on long FBGs was shown to be significantly more precise and efficient than the short-FBG-based variant in all conditions. The main reason for the different performance was attributed to the capacity of long FBGs to average the local errors in longer lengths and to the differences in the sensors' spectra. Long FBGs are considerably stronger than short ones and so the peaks are narrower and can be detected more efficiently, as can be seen in Fig. 5.7.

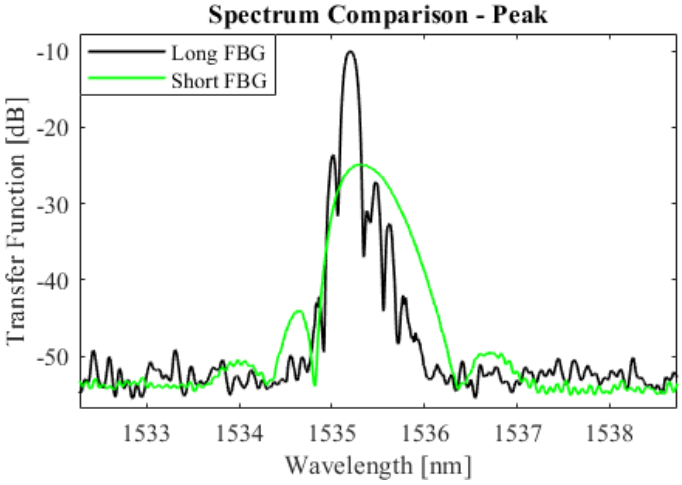

Fig. 5.7. Peak comparison of long and short FBGs [178].

To sum up, this experimental study first proves that strong FBGs can significantly enhance the shape tracking accuracy of optical multicore fiber sensors, without increasing FBG density per meter. This effect is particularly favorable when employing the WDM technique, because the number of trackable FBGs is limited and cannot be increased to improve shape reconstruction resolution. In addition, WDM analysis is the only one that reaches high frequency data acquisition. Nevertheless, even when the FBGs are interrogated by an OFDR, which allows higher grating density by reading up to several thousand gratings, long gratings can still ensure better performance at equal FBG density.

5.5 Conclusions

This Chapter has reported on an experimental and numerical study conducted to investigate the influence of strain sensors length (fiber Bragg gratings) on the performance of multicore fiber shape sensors. Two optical multicore fiber shape sensors were fabricated by inscribing long and short FBGs of the length of, respectively, 8.0 mm and 1.5 mm in a commercial 7-core fiber. Lastly, in order to comprehensively asses and compare the sensors performance, all the necessary steps for shape reconstruction were traced, including strain sensing, curvature calculation and shape reconstruction.

In all conditions, the sensor based on long FBGs was demonstrated to be remarkably more accurate. This was attributed to the ability of long FBGs to average local errors in longer length and to their narrower and stronger, thus more easily trackable, reflection peaks.

In this way, it has been first evidenced that long FBGs can remarkably improve the accuracy of MCF-based shape sensing. The use of long FBGs is notably advantageous, when wavelength division multiplexing technique is employed and, hence, the number of gratings utilizable is limited and dependent on the breadth of spectral transmission window.

The results obtained apply to both multiple single-core optical fibers and multicore optical fibers with embedded quasi-distributed strain sensors, which have the same cross section geometry, but different core spacing. In the light of the above, these new results lay the basis for the design of new and more efficient shape sensors.

CHAPTER 6 FIBER TWISTING MEASUREMENT AND COMPENSATION

6.1 Introduction

The approach for shape reconstruction illustrated in Chapter 3 is valid in absence of fiber twisting. Regrettably, due to the high flexibility, multicore fiber shape sensors are frequently subject to twisting, in addition to bending and longitudinal strain. The twisting notably reduces the shape sensors' accuracy, causing significant uncertainty in the bending direction determination, when performing 3D shape sensing [116,148,152].

Notwithstanding the vast amount of research conducted on shape sensing, this problem has not been addressed yet in an adequate manner. Tan et al. developed a torsion sensor based on inter-core mode coupling by tapering a multicore seven-core fiber [183]. Notwithstanding the innovation of this approach, it cannot be employed for shape sensing, since the fiber structure becomes inhomogeneous due to the tapering. Askins et al. first investigated the twisting of optical fibers using a tether fiber [117]. Despite its remarkable novelty, such research is not representative of the overwhelming majority of fiber optic shape sensors, consisting of MCF, and does not provide any information about the behavior of these sensors at high levels of twisting deformation, since only analyzed a limited dynamic range of twisting rotation, between ±600°/m.

Twisting measurement using MCF is an extremely arduous task due to the littleness of the state of strain generated, as a result of the small core spacing. In order to overcome this limit, the multicore fiber could be pre-twisted to increase the twisting sensibility. In this respect, recent progresses in fabrication techniques have made possible the manufacturing of spun/twisted multicore fiber with very small spin pitch, 20mm (50 turn/m) [91] and even 15.4 mm (64.9 turn/m) [93,94]. Nevertheless, an in-depth study focused on the performance of this new special multicore fiber is still missing.

This Chapter address this problem and shows an innovative method to compensate the twisting of FOSSs and, thereby, enhance the accuracy in 3D shape reconstruction in presence of fiber twisting, by employing a spun multicore fiber (also called twisted multicore fiber), with one of the most used geometry for sensing applications: the seven-core fiber.

6.2 Shape sensing in presence of twisting

This section illustrates an innovative approach, based on the Saint-Venant's Torsion Theory for homogeneous circular cylinders, to calculated the multicore fiber twisting from the longitudinal strain of sensed in fiber cores and presents an enhancement of the method, proposed by Moore and Rogge [50], in order to reconstruct shape in presence of fiber twisting using spun MCF.

6.2.1 Twisting sensing

An optical fiber, subject to pure torsion/external twisting, which must not be confused with the geometric torsion τ, can be studied as a circular cylinder that has one fixed end and the other rotates of an angle θ. Hypothesizing that the fiber has perfectly elastic behavior, plane sections remain plane, radii remain straight and cross sections remain plane and circular, it is possible to apply the Saint-Venant's Torsion Theory for homogeneous circular cylinders [184]. Thereby, the sensor is in a state of pure shear and the shear strain γ in an element of the sensor is given by Eq. (6.1).

$$\gamma = r\frac{d\theta}{ds} \tag{6.1}$$

where r is the radial distance of the element from the sensor axis and $d\theta/ds$ represents the rate of change of the angle of twisting. Since every cross section has the same radius and is subjected to the same torque, the angle $\theta(s)$ varies linearly between extremities and $d\theta/ds$ is constant. Furthermore, the shear strain varies linearly with r, from zero at the centerline to a peak value at the free surface.

To calculate the longitudinal strain in a core, distant r from the axis, it can be considered that the cores, initially straight, become circular helices ($d\theta/ds$ is constant) due to twisting, as shown in Fig. 6.1.

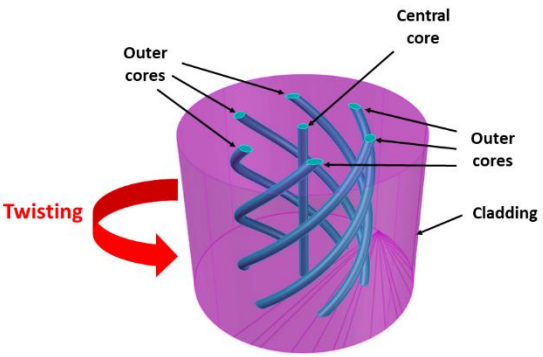

Fig. 6.1. Twisted multicore seven-core fiber [185].

The length of a core in a twisted multicore fiber can be calculated as the length of a circular helix by Eq. (6.2):

$$x = \sqrt{h^2 + r^2\theta^2} \tag{6.2}$$

where *x* is the length of the core, *h* is the length of the sensor and *r* is the distance of the core from the sensor axis and the reciprocal distance between the closest outer cores, generally called core-to-core spacing or, simply, core spacing.

Thus, the longitudinal strain of the cores due to twisting can be calculated from the definition of strain (Eq. (6.3)).

$$\varepsilon = \frac{x-h}{h} = \frac{\sqrt{h^2+r^2\theta^2}-h}{h} \tag{6.3}$$

As it can be noticed from (3), the longitudinal strain is remarkably influenced by the core spacing, length of the sensor and angle of twisting being the same. Moreover, the central core is not affected by the twisting, since its axis coincides with the sensor axis. Fig. 6.2 shows the variation of longitudinal strain due to twisting of an outer core in relation to core spacing and twisting angle per meter.

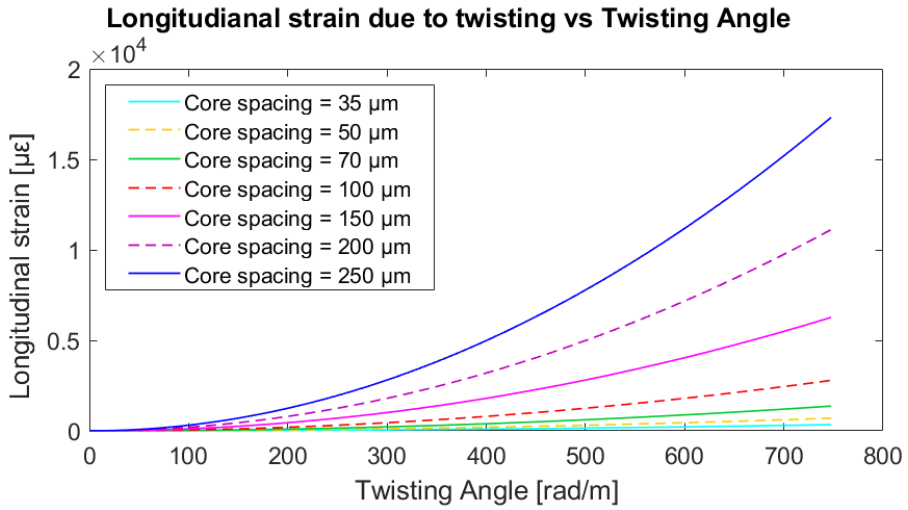

Fig. 6.2. Longitudinal strain due to twisting in relation to core spacing and twisting angle [186].

When performing three-dimensional shape sensing, the sensor is not only subject to twisting but also to bending, axial strain and thermal expansion. In this case, the component of strain due to twisting, ε_{twist}, can be calculated as defined in Eq. (6.4).

$$\varepsilon_{twist} = \frac{\sum_{i=1}^{n} \varepsilon_i^{outer}}{(n-1)} - \varepsilon_{central} \tag{6.4}$$

where ε_i^{outer} is the strain of the *i-th* outer core, $\varepsilon_{central}$ is the strain of the central core and *n* is the number of cores.

Eq. (6.4) is valid for the seven-core section geometry studied in this research and for all the section geometries with a central core and several outer cores, equidistant form the sensor axis and with equal angular spacing between them, such as the four-core and five-core section geometries with, respectively, 3 and 4 outer cores and 1 central core.

Finally, the angle of twisting can be calculated from the strain sensed in the cores, combining (6.3) and (6.4), as defined in Eq. (6.5).

$$\theta = \sqrt{\frac{h^2\varepsilon_{twist}^2 + 2h^2\varepsilon_{twist}}{r^2}} \tag{6.5}$$

It has to be pointed out that the longitudinal strain generated in the outer cores by the twisting of a non-twisted multicore fiber does not depend on direction of rotation. In other words, the twisting of a non-twisted MCF of an angle $-\theta$ or $+\theta$ always produces a positive longitudinal strain variation of the outer cores, making impossible to distinguish the sense of twisting rotation from the strain detected in the cores. To avoid this problem, a spun/pre-twisted MCF has to be used. Thereby, a twisting rotation in the direction concordant with the pre-twisting rotation produces an elongation of the outer cores, while, a twisting in the opposite direction, produces shortening. Furthermore, using a spun multicore fiber is also possible to increase the sensor sensitivity to twisting, as shown in Fig. 3 for a multicore fiber with core spacing of 35 μm.

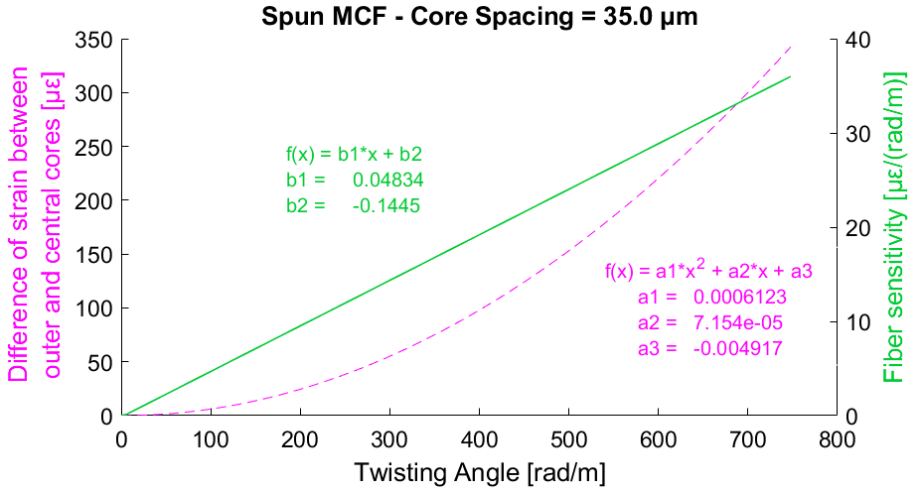

Fig. 6.3. Longitudinal strain due to twisting and fiber sensitivity to twisting in relation twisting angle for a multicore fiber with core spacing of 35 μm [186].

6.2.2 Shape reconstruction with twisting compensation

Fiber optic shape sensors are OFSs with multiple cores and embedded strain sensors. Under the Kirchhoff's rod hypotheses [155], the longitudinal strain of the fiber and

the three-dimensional curvature along fiber's length can be calculated from the strain sensed by the cores, using the Eqs. (6.6), (6.7), and (6.8) [46,166,175,187].

$$\begin{cases} \varepsilon_{long} = \sum_{i=1}^{n} \varepsilon_i / n \\ \kappa_x = \sum_{i=1}^{n} x_i \varepsilon_i / \sum_{i=1}^{n} x_i^2 \\ \kappa_y = \sum_{i=1}^{n} y_i \varepsilon_i / \sum_{i=1}^{n} y_i^2 \end{cases} \tag{6.6}$$

$$|\kappa| = \sqrt{\kappa_x^2 + \kappa_y^2} \tag{6.7}$$

$$\alpha = \tan^{-1}(\kappa_x / \kappa_y) \tag{6.8}$$

where ε_{long} is the longitudinal strain, κ_x, κ_y and $|\kappa|$ are the two components of curvature and the curvature magnitude, x_i, y_i and ε_i are, respectively, the coordinates and the strain of the *i-th* core, and α is the bending direction angle, which defines the bending direction.

Once calculated the fiber twisting along the fiber, its effects can be compensated by applying the superposition principle and correcting the bending direction angle in each instrumented section according to Eq. (6.9).

$$\alpha' = \alpha - \theta \tag{6.9}$$

where α' is the compensated bending direction angle.

Hence, by mean of interpolation or curve fitting [50,151], the functions of curvature, $\kappa(s)$, and torsion, $\tau(s)$, along the fiber can be determined respectively from curvature and from the bending direction angle (see Eqs. (6.9) and (6.10)).

$$\tau(s) = \frac{d\alpha\prime}{ds} \tag{6.10}$$

Finally, the 3D shape of the sensors can be obtained through numerical integration of the Frenet-Serret formulas (Eq. (6.11))[50]:

$$\begin{bmatrix} \boldsymbol{T}' \\ \boldsymbol{N}' \\ \boldsymbol{B}' \end{bmatrix} = \begin{bmatrix} 0 & \kappa & 0 \\ -\kappa & 0 & \tau \\ 0 & -\tau & 0 \end{bmatrix} \begin{bmatrix} \boldsymbol{T} \\ \boldsymbol{N} \\ \boldsymbol{B} \end{bmatrix} \tag{6.11}$$

where $\boldsymbol{T}$, $\boldsymbol{N}$ and $\boldsymbol{B}$ are, respectively, the tangent, normal and binormal vectors.

It is worth noting that the approach here presented is valid for several optical strain sensing technologies, including FBGs, Brillouin and Rayleigh scattering, and for different number of cores and sensor geometries, including multi-fiber shape sensors and multicore fiber shape sensors. Nonetheless, this research is only focused on multicore fiber shape sensors, since they are the most used [34,46,50,52], thanks to their compactness, ease of handling and availability, being employed for communication purposes.

It is also worth pointing out that, when it is valid the assumption of absence or negligibility of external twisting/torsion, its compensation can be omitted, for instance when the shape sensor is fastened to a rigid support, although this would limit its handiness and compactness and restrict its possible applications. Whereas, in general cases, if not compensated, the twisting leads to remarkable uncertainty in the determination of the bending direction and drastically reduces the accuracy of the sensor in performing three-dimensional shape sensing.

6.3 Fabrication of the shape sensor based on Spun MCF

A pre-twisted fiber optic shape sensor was produced in the Institute of Telecommunications and Multimedia Applications (iTEAM) of the *Universitat Politècnica de València* (UPV) by writing Fiber Bragg Gratings in a spun 7-core multicore fiber (see Fig. 1) with a spin pitch of 15.4 mm (64.9 rotation/meter), manufactured and provided by FIBERCORE Ltd. [93,94]. The fiber had seven single-mode cores (mode field diameter of 6.4 μm and numerical aperture of 0.2) with doubly symmetric configuration (60º of angular spacing and core spacing of 35 μm) and a cladding diameter of 125.1 μm.

The spun multicore fiber was hydrogen-loaded for 14 days at ambient temperature and at a pressure of 20 bars with the purpose of improving the photosensitivity. Afterward, four FBG were inscribed in a 44mm long portion of the fiber by means of a 244 nm CW frequency-doubled argon-ion laser with 60 mW output power using the phase-mask method [104]. The size of the laser beam was adjusted in order to reach all cores and the inscription was carried out simultaneously in the seven cores.

6.4 Experimental setup

Fig. 6.4 illustrates the experimental setup. The pre-twisted fiber optic shape sensor was fastened with two fiber rotators, situated at 44 mm distance from one another and assembled on multi-axis stages for nano-positioning.

First, the left fiber rotator was turned from 0° to 270° in the direction coherent with the pre-twisting and, then, moved back to the initial position. This sense of rotation is defined positive because stretches the outer cores. Thereafter, the right rotator was rotated between 0° and -270° in the negative sense of rotation, which shortens the outer cores. The sensor was interrogated by using a Static Optical Sensing Interrogator (sm125) combined with a Channel Multiplexer (sm041) (Micron Optics).

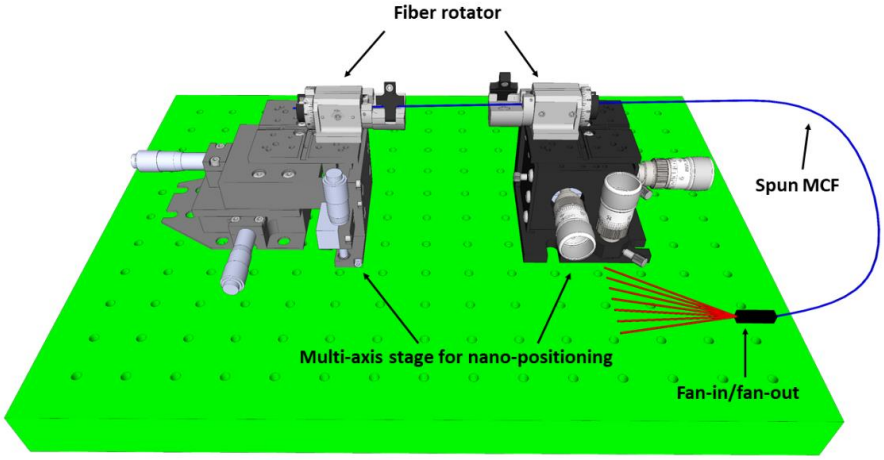

Fig. 6.4. Experimental setup [186].

6.5 Results and discussion

The pre-twisted multicore shape sensor was placed on the fiber rotators and the core spectra were recorded. Then, the FBG peaks were tracked during the experiments and their wavelength shifts were calculated and converted into strain, dividing them by a gauge factor value of 1.2 pm/με, obtained from several tensile tests and in accordance with the literature [180]. The spectra of the seven cores are plotted in Fig. 6.5.

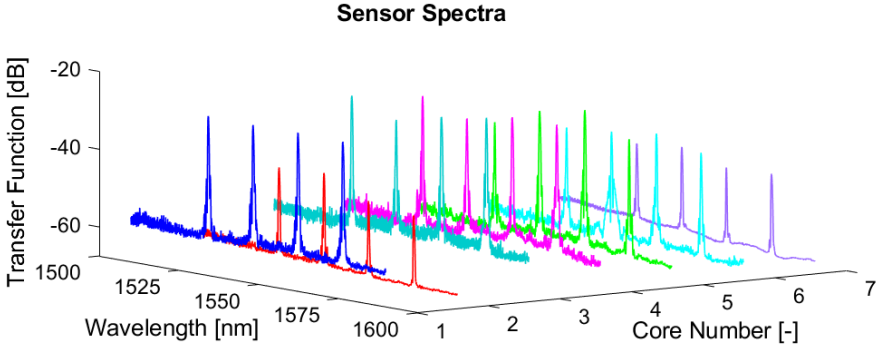

Fig. 6.5. Core spectra (the central core is the core number 1, while the cores from 2 to 7 are outer cores ordered in clockwise direction) [186].

With the aim of evaluating the accuracy of the sensor in measuring twisting, the strain of the cores was tracked, while the sensor was being twisted in the positive and negative sense of rotation, considering as positive the direction of rotation that elongates the outer cores. The values of twisting angle applied during the experiments and the resulting values of strain of the outer core due to twisting,

calculated in accordance with the theoretical approach presented in Subsection 6.2.1, are listed in Table 6.1.

Table 6.1. Inputs and outputs of the experiments according to the theoretical approach presented in Subsection 6.2.1.

Test nº	Twisting rotation [°]	Twisting and pre-twisting rotation [rad]	Fiber spin pitch [mm]	Outer cores strain variation due to twisting and pre-twisting [με]	Outer cores strain variation due to twisting [με]
0	0	17.95	15.40	101.95	0.00
1	5	18.04	15.33	102.95	0.99
2	10	18.13	15.25	103.95	1.99
3	15	18.21	15.18	104.95	3.00
4	20	18.30	15.11	105.96	4.00
5	30	18.48	14.96	107.99	6.03
6	40	18.65	14.82	110.04	8.08
7	50	18.82	14.69	112.11	10.15
8	60	19.00	14.55	114.19	12.24
9	90	19.52	14.16	120.57	18.62
10	120	20.05	13.79	127.13	25.18
11	150	20.57	13.44	133.86	31.90
12	180	21.09	13.11	140.76	38.80
13	210	21.62	12.79	147.83	45.88
14	240	22.14	12.49	155.08	53.12
15	270	22.66	12.20	162.50	60.55
0	0	17.95	15.40	101.95	0.00
1	-5	17.86	15.48	100.96	-0.99
2	-10	17.78	15.55	99.98	-1.97
3	-15	17.69	15.63	99.00	-2.95
4	-20	17.60	15.71	98.03	-3.93
5	-30	17.43	15.86	96.09	-5.86
6	-40	17.25	16.02	94.18	-7.78
7	-50	17.08	16.19	92.28	-9.67
8	-60	16.90	16.35	90.41	-11.55
9	-90	16.38	16.88	84.89	-17.06
10	-120	15.86	17.43	79.55	-22.40
11	-150	15.33	18.03	74.39	-27.57
12	-180	14.81	18.67	69.39	-32.56
13	-210	14.29	19.35	64.57	-37.38
14	-240	13.76	20.09	59.93	-42.03
15	-270	13.24	20.88	55.45	-46.50

Fig. 6.6 shows the comparison between the predicted values and the outcomes of the experiments. The experiments results are perfectly consistent with the outputs of the theoretical approach, proving that the hypotheses of the Saint-Venant's Torsion Theory hold in this problem and that the fiber has elastic behavior even at high values of deformation. Altogether, the sensor, long 44 mm, was able to detect the fiber twisting with an average sensitivity of 0.23 pm/° and an accuracy of 4.81° within a wide dynamic range of ± 270° (± 6136.4°/m), while the maximum error was of 13.53°.

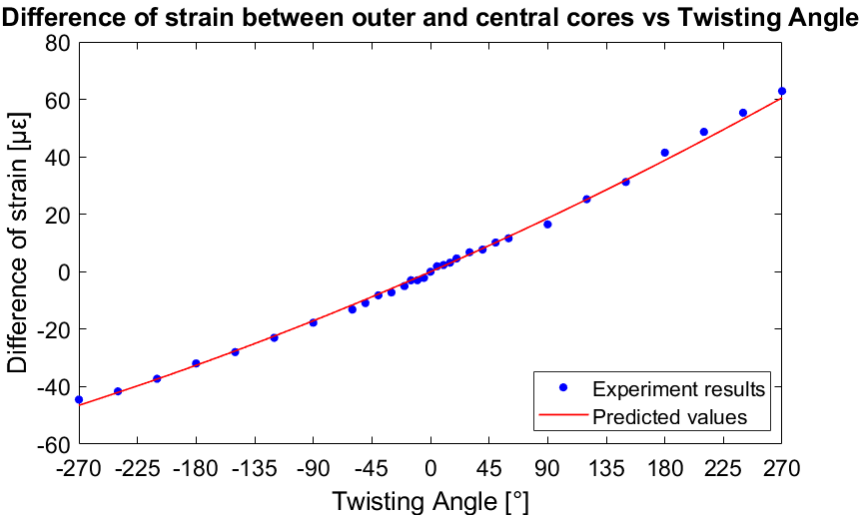

Fig. 6.6. Comparison between predicted values and experiment outcomes [186].

It has to be highlighted that, even though the fiber has a perfectly elastic behavior, the relationship between strain and twisting angle is a nonlinear and monotonically increasing function, as shown by Eq. (6.5) and Fig. 6.6. In the light of this, the sensitivity of the sensor to twisting as well as its accuracy grow with the increasing twisting and pre-twisting rotations (decreasing spin pitch). Consequently, the performance of the sensor can be improved by increasing the pre-twisting rotation, in addition to increasing the core spacing (see Eq. (6.9)). Moreover, it has to be emphasized that no temperature compensation was necessary, since the distance between the cores of the spun multicore fiber is extremely small (35 μm) and, therefore, it can be assumed that the temperature is constant in the section.

6.6 Conclusions

This Chapter presented a simple and efficient method to improve the accuracy in shape sensing by compensating the fiber twisting and described an experimental study performed to evaluate the performance in twisting sensing of a novel fiber optic shape sensor based on spun MCF.

Firstly, a theoretical approach was developed to model the mechanical behavior of the multicore fiber according to the Saint-Venant's Torsion Theory. Next, the sensor was fabricated, by inscribing 4 FBGs in a spun 7-core multicore fiber with a spin pitch of 15.4 mm/turn manufactured by FIBERCORE. Finally, a series of experiments was carried out to sense the fiber twisting, evaluate the performance of the sensor and, thus, corroborate the theoretical approach.

The results of the experimental study, perfectly consistent with the theory, first showed that optical shape sensors based on spun multicore fiber are capable of sensing twisting with high accuracy. Overall, the sensor reached a sensitivity and an accuracy in twisting sensing of, respectively, 0.23 pm/° of 4.81° within a wide dynamic range of ± 270°. Besides, it has been demonstrated that spun multicore fibers have a perfectly elastic behavior at high level of twisting deformation, confirming the validity of the Saint-Venant's Torsion Theory.

The outcomes of the experiments, first demonstrate that optical shape sensors based on spun multicore fiber are efficiently able to sense twisting and, by defining the influence of core spacing and spin pitch on the accuracy of pre-twisted fiber optic shape sensor in twisting sensing, lay the foundations for the design of a new generation of optical shape sensors.

CHAPTER 7

CONCLUSIONS AND FUTURE WORK

7.1 Summary and conclusions

Fiber optic shape sensing, an innovative branch of optical fiber sensors technologies, consists in dynamic and continuous shape monitoring using a single optical cable with embedded strain sensors. This technique offers a valuable alternative to the traditional approaches for structural health monitoring to directly track the deformed shape of structures, thanks to its outstanding advantages, including no necessity of computational models, ease of installation, no need of visual contact and infrastructure closure for data acquisition and all the advantages of OFS technologies.

Notwithstanding its great potentialities, a more profound understanding of the parameters that influence the accuracy of optical multicore fiber shape sensing is fundamental to make this technology ready for field applications.

In this research, four aspects that remarkably influence the accuracy in shape sensing of optical multicore fibers were investigated:

- The accuracy of the interrogation system, in particular, the uncertainty in strain measurement sensing considering different core spacing and curvature measured;
- The core position errors due to manufacturing defects, taking into account the effects of core spacing, curvature measured and number of cores (sensor geometry);
- Effects of strain sensor length, considering fiber Bragg gratings;
- Errors due to fiber twisting for different values of core spacing.

Furthermore, an innovative approach for twisting compensation using spun multicore fiber was proposed.

The results of the analyses are summarized in the following subsections.

7.1.1 Effects of strain resolution and core position errors

High precision in three-dimensional curvature calculation (curvature and bending direction computation) is crucial for efficient shape sensing, being the input for the

shape reconstruction process. Furthermore, curvature and bending direction sensing are employed in a number of in structural health monitoring applications [133], such as continuous monitoring of the verticality of structures, including buildings, towers, bridge piles, etc.

This study focused on the propagation of strain measurement uncertainty and core position errors in curvature and bending direction sensing, simulating the measurement process by using the Monte Carlo method with more than 1 million iterations per simulation. A statistical significance test was then carried out to verify the results of the simulations. Finally, the relationships between the variables involved were determined calibrating a series of predictive models.

It was found that the accuracy in 3D curvature calculation notably grows at increasing values of accuracy in strain sensing and core positioning. Besides, it was demonstrated the role played by core spacing and number of cores, which resulted to have significant beneficial effects, since great values of both parameters correspond to a slower uncertainty propagation.

The quantitative definition of the mathematical relationship between the variables is of paramount importance to improve the performance of multicore fiber sensors. There are a multitude of commercial interrogation systems available in the market and the accuracy of these products is declared in terms of strain. Consequently, how the accuracy in strain sensing affects the accuracy in three-dimensional curvature sensing is essential to select the proper interrogation unit for curvature/shape monitoring purposes and it can be determined by using the predictive models developed in this study.

The situation is more complex, in the case of the geometrical parameters considered in this study, such as core spacing, core position and number of cores. In fact, this investigation clearly shows their strong influence on curvature and shape sensing. Nevertheless, the multicore fibers available nowadays and suitable for sensing applications are lamentably limited, as, generally, they are the same produced for telecommunication applications. This leads to the following consequences:

- The diameter of commercial MCFs is very small (regularly about 125 μm) and the core spacing is normally between 30 and 50 μm [50,53,84,92,133,172,173];
- The number of cores of standard multicore fiber are generally the ones studied in the second part of this study: 3-core, 4-core and 7-core fiber;
- Core position errors are due to errors in the manufacturing process, range between a few hundred nanometers to one micrometer [93,188] and depend on the optical fiber drawing technique and the production equipment. Regrettably, customarily, manufacturing companies do not provide any information in this regard.

Manufacturing different MCF geometries for sensing purposes can be prohibitively expensive, considering that the sensors market is limited compared to the telecommunications one. However, this study demonstrated that such MCFs would have a multitude of application fields. Since better accuracy can be achieved by increasing the core spacing, optical shape sensors consisting of multiple optical fibers fastened to a support can be developed, although less compact [126,128].

In the light of the above, this research work means to increase awareness of the researchers and professionals about this matter.

7.1.2 Influence of strain sensors length

This experimental and numerical study focuses on the influence of strain sensors length on the performance of multicore fiber shape sensor with embedded fiber Bragg gratings. Two optical multicore fiber shape sensors were fabricated by writing long and short FBGs of the length of, respectively, 8.0 mm and 1.5 mm in a commercial 7-core fiber. The necessary steps for shape reconstruction were traced, comprising strain sensing, curvature calculation and shape integration, and thus sensors performances were contrasted.

In all conditions, the sensor based on long FBGs was found to be remarkably more accurate than the short variant. This was imputed to the ability of long FBGs to average local errors in longer distance and to its narrower and stronger reflection peaks compared to short ones, which make the peaks more easily trackable.

In this way, it has been first demonstrated that long gratings can remarkably improve the accuracy of shape sensing using optical MCF sensors. The employment of long FBGs is particularly convenient, when wavelength division multiplexing technique is used and, therefore, the number of gratings utilizable is limited, being dependent on the breadth of spectral transmission window, and cannot be increased to achieve better performance.

Nonetheless, also when the gratings are read with an Optical Frequency Domain Reflectometry (OFDR), which allows the increase of the FBGs density, by interrogating even thousands of them, (while the uncertainties in the strain measurement of a single FBG is higher [177]) to enhance the accuracy, the use of long FBGs can still guarantee better performance, the number of gratings being equal.

7.1.3 Fiber twisting measurement and compensation

The last part of the thesis reports on experimental study carried out to investigate the performance in sensing and compensating twisting of an innovative fiber optic shape sensor based on spun (or pre-twisted) MCF and presents a simple method to enhance the accuracy in shape sensing by means of twisting compensation.

First, a theoretical approach based on the Saint-Venant's Torsion Theory was developed to model the mechanical behavior of the fiber. Next, the sensor was fabricated, by writing four FBGs in a spun 7-core multicore fiber (spin pitch of 15.4 mm/turn) manufactured and provided by FIBERCORE. To conclude, a series of twisting experiments were performed to corroborate the theoretical approach and assess the performance of the sensor.

The outcomes of the experiments, perfectly consistent with the theory, first demonstrate that optical shape sensors based on spun multicore fiber are efficiently able to sense twisting. In addition, it was proved that the spun multicore fiber maintains a perfectly elastic behavior, even at high level of twisting deformation, assumption underpinning the Saint-Venant's Torsion Theory. Altogether, the sensor was able to sense twisting with a sensitivity of 0.23 pm/° and accuracy of 4.81° within a wide dynamic range of ± 270°.

The research outcomes, by defining the influence of core spacing and spin pitch on the accuracy of pre-twisted fiber optic shape sensor in twisting sensing, lays the foundations for the design of a new generation of optical multicore fiber sensor for 3D shape sensing.

7.2 Future prospective

This research brought to light many factors that can influence the accuracy of shape sensing based on optical multicore fiber with embedded strain sensors. Besides, powerful instruments were developed to analytically predict their achievable performance. Even though this new technology is not fully prepared for field applications, the deeper comprehension of these aspects significantly contributes to consolidate it and raise awareness of its limits.

Significant improvement that can be accomplished by enhancing the accuracy in strain measurement and core position and increasing the number of cores or the length of FBG strain sensors. Nevertheless, the main priority to successfully implement this new technology in structural health monitoring application is to manufacture standard fiber geometries with larger core spacing. Two main reasons are related to this observation: I) the core spacing resulted to be the parameter that most influences the performance of these sensors in curvature, twisting and shape sensing; II) this is the most easily achievable solution. On the other hand, the increase of the number of cores makes the process of FBGs inscription and fiber manufacturing notably more complex. In addition, the technology necessary for the fabrication of multicore fibers with significant higher accuracy in core position or more precise interrogation systems would represent an enormous cost. Instead, the manufacturing of multicore fiber with larger core spacing is attainable with the fabrication technique already employed for the fabrication of standard and commercial multicore fiber.

By using Equation 3.6, considering a strain resolution equal to 1 με, typical value for commercial interrogation system nowadays and neglecting all the other source of errors and geometrical parameters considered in this study (strain measurement accuracy, core position errors and number of cores), it is possible to define a simple and approximated relationship between the core spacing and the curvature resolution of shape sensor, as illustrated in Fig. 7.1.

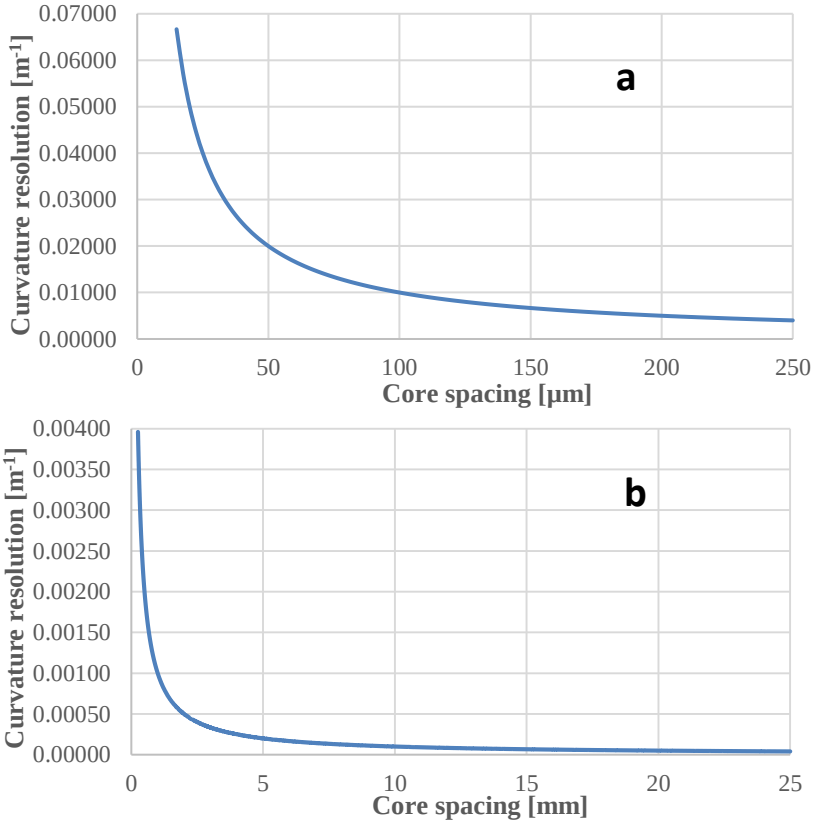

Fig. 7.1. Relationship between curvature resolution and core spacing for a strain resolution of 1 με, in the range of core spacing between (a) 30 and 250 μm; (b) 0.250 and 25 mm.

Multicore fiber shape sensors with large core spacing can find application in bridge and tunnel health monitoring, typical applications of SHM, where the correct tracking of the deformed shape of the structure is of fundamental importance, as explained in Section 2.3.1.

By way of example, to estimate the order of magnitude of curvature in SHM applications, the American Association of State Highway and Transportation Officials (AASHTO) in the AASHTO LRFD Bridge Design Specifications [189,190], Article 2.5.2.6, advises that the maximum deformation of a bridge should not exceed the Span Length, *L*, divided by 800, (*L/800*) for general vehicular bridges,

and divided by 1000, (*L/1000*) for vehicular bridges with pedestrian traffic. In this last case, considering two spans simply supported of length of 30 m and 100 m, the curvature would be 0.00045 m^{-1} and 0.00013 m^{-1}. The curvature resolution of a multicore fiber shape sensor with core spacing of 25 mm (25000 μm) would be 0.00004 m^{-1}, far below. Similar considerations can be done in the case of tunnels health monitoring or geotechnical applications.

Several researchers tried to obtain shape sensors with larger core spacing and better curvature resolutions, manufacturing multi-fiber shape sensor, composed by multiple optical fibers fastened to a support with the aim of developing a novel optical inclinometer [126,128]. The idea is interesting, nevertheless, these solutions are less compact, and the accuracy of the results obtained was poor compared to the theoretical value, because of the nonstandardized fabrication procedure.

In conclusion, there is a multitude of possible application for fiber optic shape sensor in civil engineering application, such as bridges and tunnel health monitoring and geotechnical application, as inclinometer. However, new geometries need to be developed.

REFERENCES

[1] Mattei NJ. INFRASTRACTURE REPORT CARD 2017: A comprehensive assesment of Americas's Infrastructure. Asce 2017:1–112.

[2] Hao S. I-35W Bridge Collapse. J Bridg Eng 2010;15:608–14. doi:10.1061/(ASCE)BE.1943-5592.0000090.

[3] DoL/OSHA U. Investigation of March 15, 2018 Pedestrian Bridge Collapse at Florida International University, Miami, FL 2019:115.

[4] Cao R, El-Tawil S, Agrawal AK. Miami Pedestrian Bridge Collapse: Computational Forensic Analysis. J Bridg Eng 2020;25:04019134. doi:10.1061/(ASCE)BE.1943-5592.0001532.

[5] Morgese M, Ansari F, Domaneschi M, Cimellaro GP. Post-collapse analysis of Morandi's Polcevera viaduct in Genoa Italy. J Civ Struct Heal Monit 2020;10:69–85. doi:10.1007/s13349-019-00370-7.

[6] Morandi bridge collapse triggers calls for investment in infrastructure. New Eur 2018:https://www.neweurope.eu/article/the-collapse-of-t.

[7] Hajela P, Soeiro FJ. Structural damage detection based on static and modal analysis. AIAA J 1990;28:1110–5. doi:10.2514/3.25174.

[8] Chang PC, Flatau A, Liu SC. Review Paper: Health Monitoring of Civil Infrastructure. Struct Heal Monit An Int J 2003;2:257–67. doi:10.1177/1475921703036169.

[9] Feng D, Feng MQ. Computer vision for SHM of civil infrastructure: From dynamic response measurement to damage detection – A review. Eng Struct 2018;156:105–17. doi:10.1016/j.engstruct.2017.11.018.

[10] Li X, Ji Z, Zhu H, Gu C. A feasibility study of the measuring accuracy and capability of wireless sensor networks in tunnel monitoring. Front Struct Civ Eng 2012;6:111–20. doi:10.1007/s11709-012-0150-1.

[11] Brownjohn JM. Structural health monitoring of civil infrastructure. Philos Trans R Soc A Math Phys Eng Sci 2007;365:589–622. doi:10.1098/rsta.2006.1925.

[12] Agdas D, Rice JA, Martinez JR, Lasa IR. Comparison of Visual Inspection and Structural-Health Monitoring As Bridge Condition Assessment Methods. J Perform Constr Facil 2016;30:04015049. doi:10.1061/(ASCE)CF.1943-5509.0000802.

[13] López-Higuera JM, Cobo LR, Incera AQ, Cobo A. Fiber optic sensors in

structural health monitoring. J Light Technol 2011;29:587–608. doi:10.1109/JLT.2011.2106479.

[14] Haksoo Choi, Sukwon Choi, Hojung Cha. Structural Health Monitoring system based on strain gauge enabled wireless sensor nodes. 2008 5th Int. Conf. Networked Sens. Syst., IEEE; 2008, p. 211–4. doi:10.1109/INSS.2008.4610888.

[15] Schaefer P-L, Barrier G, Chagnon G, Alonso T, Moreau-Gaudry A. Strain Gauges Based 3D Shape Monitoring of Beam Structures Using Finite Width Gauge Model. Exp Tech 2019;43:599–611. doi:10.1007/s40799-019-00312-4.

[16] Campanella C, Cuccovillo A, Campanella C, Yurt A, Passaro V. Fibre Bragg Grating Based Strain Sensors: Review of Technology and Applications. Sensors 2018;18:3115. doi:10.3390/s18093115.

[17] He J, Zhou Y, Guan X, Zhang W, Wang Y, Zhang W. An Integrated Health Monitoring Method for Structural Fatigue Life Evaluation Using Limited Sensor Data. Materials (Basel) 2016;9:894. doi:10.3390/ma9110894.

[18] Grosse C, McLaskey G, Bachmaier S, Glaser SD, Krüger M. A hybrid wireless sensor network for acoustic emission testing in SHM. In: Tomizuka M, editor. Sensors Smart Struct. Technol. Civil, Mech. Aerosp. Syst. 2008, vol. 6932, 2008, p. 693238. doi:10.1117/12.775641.

[19] Nair A, Cai CS. Acoustic emission monitoring of bridges: Review and case studies. Eng Struct 2010;32:1704–14. doi:10.1016/j.engstruct.2010.02.020.

[20] Cha Y-J, Choi W, Büyüköztürk O. Deep Learning-Based Crack Damage Detection Using Convolutional Neural Networks. Comput Civ Infrastruct Eng 2017;32:361–78. doi:10.1111/mice.12263.

[21] Ye XW, Dong CZ, Liu T. A Review of Machine Vision-Based Structural Health Monitoring: Methodologies and Applications. J Sensors 2016;2016:1–10. doi:10.1155/2016/7103039.

[22] Milillo P, Porcu MC, Lundgren P, Soccodato F, Salzer J, Fielding E, et al. The ongoing destabilization of the mosul dam as observed by synthetic aperture radar interferometry. 2017 IEEE Int. Geosci. Remote Sens. Symp., vol. 7, IEEE; 2017, p. 6279–82. doi:10.1109/IGARSS.2017.8128442.

[23] Gentile C. Application of Radar Technology to Deflection Measurement and Dynamic Testing of Bridges. Radar Technol., vol. 395, InTech; 2010, p. 116–24. doi:10.5772/7178.

[24] Gentile C, Bernardini G. Radar-based measurement of deflections on bridges and large structures. Eur J Environ Civ Eng 2010;14:495–516.

doi:10.1080/19648189.2010.9693238.

[25] Mottershead JE, Friswell MI. Model Updating In Structural Dynamics: A Survey. J Sound Vib 1993;167:347–75. doi:10.1006/jsvi.1993.1340.

[26] Frau A, Pieczonka L, Porcu MC, Staszewski WJ, Aymerich F. Analysis of elastic nonlinearity for impact damage detection in composite laminates. J Phys Conf Ser 2015;628:012103. doi:10.1088/1742-6596/628/1/012103.

[27] Porcu MC, Patteri DM, Melis S, Aymerich F. Effectiveness of the FRF curvature technique for structural health monitoring. Constr Build Mater 2019;226:173–87. doi:10.1016/j.conbuildmat.2019.07.123.

[28] Porcu MC, Pieczonka L, Frau A, Staszewski WJ, Aymerich F. Assessing the Scaling Subtraction Method for Impact Damage Detection in Composite Plates. J Nondestruct Eval 2017;36:33. doi:10.1007/s10921-017-0413-9.

[29] Sohn H, Farrar CR, Hunter NF, Worden K. Structural Health Monitoring Using Statistical Pattern Recognition Techniques. J Dyn Syst Meas Control 2001;123:706–11. doi:10.1115/1.1410933.

[30] Tosi D, Schena E, Molardi C, Korganbayev S. Fiber optic sensors for sub-centimeter spatially resolved measurements: Review and biomedical applications. Opt Fiber Technol 2018;43:6–19. doi:10.1016/j.yofte.2018.03.007.

[31] He J, Zhou Z, Jinping O. Optic fiber sensor-based smart bridge cable with functionality of self-sensing. Mech Syst Signal Process 2013;35:84–94. doi:10.1016/j.ymssp.2012.08.022.

[32] Roveri N, Carcaterra A, Sestieri A. Real-time monitoring of railway infrastructures using fibre Bragg grating sensors. Mech Syst Signal Process 2015;60–61:14–28. doi:10.1016/j.ymssp.2015.01.003.

[33] Alian H, Konforty S, Ben-Simon U, Klein R, Tur M, Bortman J. Bearing fault detection and fault size estimation using fiber-optic sensors. Mech Syst Signal Process 2019;120:392–407. doi:10.1016/j.ymssp.2018.10.035.

[34] Beisenova A, Issatayeva A, Tosi D, Molardi C. Fiber-Optic Distributed Strain Sensing Needle for Real-Time Guidance in Epidural Anesthesia. IEEE Sens J 2018;18:8034–44. doi:10.1109/JSEN.2018.2865220.

[35] Sultangazin A, Kusmangaliyev J, Aitkulov A, Akilbekova D, Olivero M, Tosi D. Design of a Smartphone Plastic Optical Fiber Chemical Sensor for Hydrogen Sulfide Detection. IEEE Sens J 2017;17:6935–40. doi:10.1109/JSEN.2017.2752717.

[36] Madrigal J, Barrera D, Sales S. Refractive Index and Temperature Sensing Using Inter-Core Crosstalk in Multicore Fibers. J Light Technol

2019;37:4703–9. doi:10.1109/JLT.2019.2917629.

[37] Piestrzyńska M, Dominik M, Kosiel K, Janczuk-Richter M, Szot-Karpińska K, Brzozowska E, et al. Ultrasensitive tantalum oxide nano-coated long-period gratings for detection of various biological targets. Biosens Bioelectron 2019;133:8–15. doi:10.1016/j.bios.2019.03.006.

[38] Zhao Y, Zhou X, Li X, Zhang Y. Review on the graphene based optical fiber chemical and biological sensors. Sensors Actuators B Chem 2016;231:324–40. doi:10.1016/j.snb.2016.03.026.

[39] Gertsbakh I. Measurand and Measurement Errors. Meas. Theory Eng., Berlin, Heidelberg: Springer Berlin Heidelberg; 2003. doi:10.1007/978-3-662-08583-7_1.

[40] Li P, Zhang Z, Zhang J. Simultaneously identifying displacement and strain flexibility using long-gauge fiber optic sensors. Mech Syst Signal Process 2019;114:54–67. doi:10.1016/j.ymssp.2018.05.005.

[41] Zhou Z, Liu W, Huang Y, Wang H, Jianping H, Huang M, et al. Optical fiber Bragg grating sensor assembly for 3D strain monitoring and its case study in highway pavement. Mech Syst Signal Process 2012;28:36–49. doi:10.1016/j.ymssp.2011.10.003.

[42] Mieloszyk M, Ostachowicz W. Moisture contamination detection in adhesive bond using embedded FBG sensors. Mech Syst Signal Process 2017;84:1–14. doi:10.1016/j.ymssp.2016.07.006.

[43] Fuhr PL, Kajenski PJ, Kunkel DL, Huston DR. A subcarrier intensity modulated fiber optic sensor for structural vibration measurements. Mech Syst Signal Process 1993;7:133–43. doi:10.1006/mssp.1993.1003.

[44] Zheng D, Cai Z, Floris I, Madrigal J, Pan W, Zou X, et al. Temperature-insensitive optical tilt sensor based on a single eccentric-core fiber Bragg grating. Opt Lett n.d. doi:10.1364/OL.99.099999.

[45] Amanzadeh M, Aminossadati SM, Kizil MS, Rakić AD. Recent developments in fibre optic shape sensing. Meas J Int Meas Confed 2018;128:119–37. doi:10.1016/j.measurement.2018.06.034.

[46] Floris I, Madrigal J, Sales S, Adam JM, Calderón PA. Experimental study of the influence of FBG length on optical shape sensor performance. Opt Lasers Eng 2020;126:105878. doi:10.1016/j.optlaseng.2019.105878.

[47] Gander MJ, MacPherson WN, McBride R, Jones JDC, Zhang L, Bennion I, et al. Bend mesurement using Bragg gratings in multicore fibre. Electron Lett 2000;36:2–3.

[48] Miller GA, Askins CG, Friebele EJ. Shape sensing using distributed fiber

optic strain measurements. Second Eur. Work. Opt. Fibre Sensors, vol. 5502, 2004, p. 528. doi:10.1117/12.566653.

[49] Duncan RG, Froggatt ME, Kreger ST, Seeley RJ, Gifford DK, Sang AK, et al. High-accuracy fiber-optic shape sensing. In: Peters KJ, editor. Phenomena, Technol. Appl. NDE Heal. Monit. 2007, vol. 6530, 2007, p. 65301S. doi:10.1117/12.720914.

[50] Moore JP, Rogge MD. Shape sensing using multi-core fiber optic cable and parametric curve solutions. Opt Express 2012;20:2967. doi:10.1364/OE.20.002967.

[51] Moon H, Jeong J, Kang S, Kim K, Song Y-W, Kim J. Fiber-Bragg-grating-based ultrathin shape sensors displaying single-channel sweeping for minimally invasive surgery. Opt Lasers Eng 2014;59:50–5. doi:10.1016/j.optlaseng.2014.03.005.

[52] Khan F, Denasi A, Barrera D, Madrigal J, Sales S, Misra S. Multi-Core Optical Fibers With Bragg Gratings as Shape Sensor for Flexible Medical Instruments. IEEE Sens J 2019;19:5878–84. doi:10.1109/JSEN.2019.2905010.

[53] MacPherson WN, Silva-Lopez M, Barton JS, Moore AJ, Jones JDC, Zhao D, et al. Tunnel monitoring using multicore fibre displacement sensor. Meas Sci Technol 2006;17:1180–5. doi:10.1088/0957-0233/17/5/S41.

[54] Barrera D, Madrigal J, Delepine-Lesoille S, Sales S. Multicore optical fiber shape sensors suitable for use under gamma radiation. Opt Express 2019;27:29026. doi:10.1364/OE.27.029026.

[55] ITN-FINESSE, http://itn-finesse.eu/ n.d.

[56] Koch E, Dietzel A. Surface reconstruction by means of a flexible sensor array. Sensors Actuators A Phys 2017;267:293–300. doi:10.1016/j.sna.2017.10.023.

[57] Wang Q, Liu Y. Review of optical fiber bending/curvature sensor. Meas J Int Meas Confed 2018;130:161–76. doi:10.1016/j.measurement.2018.07.068.

[58] Wong WY, Wong MS. Detecting spinal posture change in sitting positions with tri-axial accelerometers. Gait Posture 2008;27:168–71. doi:10.1016/j.gaitpost.2007.03.001.

[59] Griffith C, Dare P, Danish L. Calibration enhancement of ShapeAccelArray technology for long term deformation monitoring applications. IEEE/ION Position, Locat. Navig. Symp., IEEE; 2010, p. 621–6. doi:10.1109/PLANS.2010.5507183.

[60] Green E, Mikkelsen PE. Deformation Measurements with Inclinometers

1952.

[61] Stark TD, Choi H. Slope inclinometers for landslides. Landslides 2008;5:339–50. doi:10.1007/s10346-008-0126-3.

[62] Hou X, Yang X, Huang Q. Using Inclinometers to Measure Bridge Deflection. J Bridg Eng 2005;10:564–9. doi:10.1061/(ASCE)1084-0702(2005)10:5(564).

[63] Plamondon A, Delisle A, Larue C, Brouillette D, McFadden D, Desjardins P, et al. Evaluation of a hybrid system for three-dimensional measurement of trunk posture in motion. Appl Ergon 2007;38:697–712. doi:10.1016/j.apergo.2006.12.006.

[64] Dementyev A, Kao HLC, Paradiso JA. SensorTape: Modular and programmable 3D-aware dense sensor network on a tape. UIST 2015 - Proc 28th Annu ACM Symp User Interface Softw Technol 2015:649–58. doi:10.1145/2807442.2807507.

[65] Mentzer MA. Fiber Optic Sensors. vol. 20020456. CRC Press; 2002. doi:10.1201/9780824744571.

[66] Lee B. Review of the present status of optical fiber sensors. Opt Fiber Technol 2003;9:57–79. doi:10.1016/S1068-5200(02)00527-8.

[67] Rao Y-J. In-fibre Bragg grating sensors. Meas Sci Technol 1997;8:355–75. doi:10.1088/0957-0233/8/4/002.

[68] Correia R, James S, Lee S-W, Morgan SP, Korposh S. Biomedical application of optical fibre sensors. J Opt 2018;20:073003. doi:10.1088/2040-8986/aac68d.

[69] Barrias A, Casas J, Villalba S. A Review of Distributed Optical Fiber Sensors for Civil Engineering Applications. Sensors 2016;16:748. doi:10.3390/s16050748.

[70] Leung CKY, Wan KT, Inaudi D, Bao X, Habel W, Zhou Z, et al. Review: optical fiber sensors for civil engineering applications. Mater Struct 2015;48:871–906. doi:10.1617/s11527-013-0201-7.

[71] Griffioen W. Optical fiber mechanical reliability. 1995. doi:10.6100/IR435417.

[72] Matthewson MJ, Kurkjian CR, Gulati ST. Strength measurement of opticaal fibers by bending. J Am Ceram Sosiety 1986;69:815–21. doi:10.1111/j.1151-2916.1986.tb07366.x.

[73] Kurkjian CR, Krause JT, Matthewson MJ. Strength and fatigue of silica optical fibers. J Light Technol 1989;7:1360–70. doi:10.1109/50.50715.

[74] Glaesemann GS. Advancements in mechanical strength and reliability of optical fibers. Reliab. Opt. Fibers Opt. Fiber Syst. A Crit. Rev., vol. 10295, 1999, p. 1029502. doi:10.1117/12.361072.

[75] Meltz G, Dunphy JR, Glenn WH, Farina JD, Leonberger FJ. Fiber Optic Temperature And Strain Sensors. In: Verga Scheggi AM, editor., 1987, p. 104. doi:10.1117/12.941093.

[76] Bao X, Chen L. Recent Progress in Distributed Fiber Optic Sensors. Sensors 2012;12:8601–39. doi:10.3390/s120708601.

[77] Ishio H, Minowa J, Nosu K. Review and Status of Wavelength-Division-Multiplexing Technology and Its Application. J Light Technol 1984;2:448–63. doi:10.1109/JLT.1984.1073653.

[78] Kersey AD, Morey WW. Multiplexed Bragg grating fibre-laser strain-sensor system with mode-locked interrogation. Electron Lett 1993;29:112–4. doi:10.1049/el:19930073.

[79] Chen; PC, Sirkis JS. Method and apparatus for determining the shape of a flexible body, US Patent 6256090B1, 2001.

[80] Greenaway AH, Burnett JG, Harvey AR, Blanchard PM, Lloyd PA, Mcbride R, et al. Optical fibre bend sensor, World Intellectual Property Organization Patent WO1998059219A3. https://patents.google.com/patent/WO1998059219A3, 1998.

[81] Greenaway AH, Burnett JG, Harvey AR, McBride PAL, Russell PSJ, Blanchard PM. Optical fiber bend sensor, US Patent US6389187B1, 2002.

[82] Blanchard PM, Burnett JG, Erry GRG, Greenaway AH, Harrison P, Mangan B, et al. Two-dimensional bend sensing with a single, multi-core optical fibre. Smart Mater Struct 2000;9:132–40. doi:10.1088/0964-1726/9/2/302.

[83] Burnett JG, Blanchard PM, Greenaway AH. Optical Fibre-based Vectoral Shape Sensor 2000;36.

[84] Flockhart GMH, MacPherson WN, Barton JS, Jones JDC, Zhang L, Bennion I. Two-axis bend measurement with Bragg gratings in multicore optical fiber. Opt Lett 2003;28:387. doi:10.1364/OL.28.000387.

[85] MacPherson WN, Flockhart GMH, Maier RRJ, Barton JS, Jones JDC, Zhao D, et al. Pitch and roll sensing using fibre Bragg gratings in multicore fibre. Meas Sci Technol 2004;15:1642–6. doi:10.1088/0957-0233/15/8/036.

[86] Clements GM. Fiber optic sensor for precision 3-D position measurement, US Patent 6888623B2, 2003.

[87] Zhang L, Qian J, Shen L, Zhang Y. FBG sensor devices for spatial shape

detection of intelligent colonoscope. IEEE Int. Conf. Robot. Autom. 2004. Proceedings. ICRA '04. 2004, vol. 2004, IEEE; 2004, p. 834-840 Vol.1. doi:10.1109/ROBOT.2004.1307253.

[88] Yi X, Niu F, He J, Fan H. The 3D shape analysis of elastic rod in shape sensing medical robot system. 2010 IEEE Int. Conf. Robot. Biomimetics, IEEE; 2010, p. 1014–8. doi:10.1109/ROBIO.2010.5723465.

[89] Froggatt ME, Duncan RG. Fiber optic position and/or shape sensing based on rayleigh scatter, US Patent 7772541B2, 2010.

[90] Moore JP, Rogge MD. Shape Sensing Using a Multi-Core Optical Fiber Having an Arbitrary Initial Shape in the Presence of Extrinsic Forces, US Patent 8746076B2, 2014.

[91] Westbrook PS, Feder KS, Kremp T, Taunay TF, Monberg E, Kelliher J, et al. Integrated optical fiber shape sensor modules based on twisted multicore fiber grating arrays. In: Gannot I, editor. Opt. Fibers Sensors Med. Diagnostics Treat. Appl. XIV, vol. 8938, 2014, p. 89380H. doi:10.1117/12.2041775.

[92] Westbrook PS, Kremp T, Feder KS, Ko W, Monberg EM, Wu H, et al. Continuous Multicore Optical Fiber Grating Arrays for Distributed Sensing Applications. J Light Technol 2017;35:1248–52. doi:10.1109/JLT.2017.2661680.

[93] Cooper LJ, Webb AS, Gillooly A, Hill M, Read T, Maton P, et al. Design and performance of multicore fiber optimized towards communications and sensing applications. In: Jiang S, Digonnet MJF, editors. Proc. SPIE - Int. Soc. Opt. Eng., vol. 9359, 2015, p. 93590H. doi:10.1117/12.2076950.

[94] https://www.fibercore.com/product/multicore-fiber n.d.

[95] Zhao Z, Soto MA, Tang M, Thévenaz L. Distributed shape sensing using Brillouin scattering in multi-core fibers. Opt Express 2016;24:25211. doi:10.1364/OE.24.025211.

[96] Khan F, Roesthuis RJ, Misra S. Force sensing in continuum manipulators using fiber Bragg grating sensors. 2017 IEEE/RSJ Int. Conf. Intell. Robot. Syst., vol. 2017- Septe, IEEE; 2017, p. 2531–6. doi:10.1109/IROS.2017.8206073.

[97] Zhang S, Bae Lee S, Fang X, Sam Choi S. In-fiber grating sensors. Opt Lasers Eng 1999;32:405–18. doi:10.1016/S0143-8166(99)00052-4.

[98] Rao Y. Recent progress in applications of in-fibre Bragg grating sensors. Opt Lasers Eng 1999;31:297–324. doi:10.1016/S0143-8166(99)00025-1.

[99] Ferraro P, De Natale G. On the possible use of optical fiber Bragg gratings

as strain sensors for geodynamical monitoring. Opt Lasers Eng 2002;37:115–30. doi:10.1016/S0143-8166(01)00141-5.

[100] Spirin V., Shlyagin M., Miridonov S., Jiménez FJM, Gutiérrez RML. Fiber Bragg grating sensor for petroleum hydrocarbon leak detection. Opt Lasers Eng 1999;32:497–503. doi:10.1016/S0143-8166(00)00021-X.

[101] Botsis J, Humbert L, Colpo F, Giaccari P. Embedded fiber Bragg grating sensor for internal strain measurements in polymeric materials. Opt Lasers Eng 2005;43:491–510. doi:10.1016/j.optlaseng.2004.04.009.

[102] Ma Z, Chen X. Fiber Bragg Gratings Sensors for Aircraft Wing Shape Measurement: Recent Applications and Technical Analysis. Sensors 2018;19:55. doi:10.3390/s19010055.

[103] Salo J, Korhonen I. Calculated estimate of FBG sensor's suitability for beam vibration and strain measuring. Measurement 2014;47:178–83. doi:10.1016/j.measurement.2013.08.017.

[104] Kashyap R. Fiber Bragg Gratings. 2nd Editio. Elsevier; 2010.

[105] Masoudi A, Newson TP. Contributed Review: Distributed optical fibre dynamic strain sensing. Rev Sci Instrum 2016;87:011501. doi:10.1063/1.4939482.

[106] Ding Z, Wang C, Liu K, Jiang J, Yang D, Pan G, et al. Distributed Optical Fiber Sensors Based on Optical Frequency Domain Reflectometry: A review. Sensors 2018;18:1072. doi:10.3390/s18041072.

[107] Thévenaz L. Review and Progress on Distributed Fibre Sensing. Opt. Fiber Sensors, Washington, D.C.: OSA; 2006, p. ThC1. doi:10.1364/OFS.2006.ThC1.

[108] Yuksel K. Rayleigh-based Optical Reflectometry Techniques for Distributed Sensing Applications. 2009 11th Int. Conf. Transparent Opt. Networks, IEEE; 2009, p. 1–5.

[109] Palmieri L. Distributed Optical Fiber Sensing Based on Rayleigh Scattering. Open Opt J 2013;7:104–27. doi:10.2174/1874328501307010104.

[110] Loranger S, Gagné M, Lambin-Iezzi V, Kashyap R. Rayleigh scatter based order of magnitude increase in distributed temperature and strain sensing by simple UV exposure of optical fibre. Sci Rep 2015;5:11177. doi:10.1038/srep11177.

[111] Westbrook PS, Kremp T, Feder KS, Ko W, Monberg EM, Wu H, et al. Performance characteristics of continuously grated multicore sensor fiber. In: Chung Y, Jin W, Lee B, Canning J, Nakamura K, Yuan L, editors. vol. 10323, 2017, p. 103236I. doi:10.1117/12.2263481.

[112] Schenato L. A Review of Distributed Fibre Optic Sensors for Geo-Hydrological Applications. Appl Sci 2017;7:896. doi:10.3390/app7090896.

[113] Thévenaz L. Brillouin distributed time-domain sensing in optical fibers: state of the art and perspectives. Front Optoelectron China 2010;3:13–21. doi:10.1007/s12200-009-0086-9.

[114] Barrera D, Gasulla I, Sales S. Multipoint Two-Dimensional Curvature Optical Fiber Sensor Based on a Nontwisted Homogeneous Four-Core Fiber. J Light Technol 2015;33:2445–50. doi:10.1109/JLT.2014.2366556.

[115] Barrera D, Madrigal J, Sales S. Long Period Gratings in Multicore Optical Fibers for Directional Curvature Sensor Implementation. J Light Technol 2018;36:1063–8. doi:10.1109/JLT.2017.2764951.

[116] Klute S, Duncan R, Fielder R, Butler G, Mabe J, Sang A, et al. Fiber-Optic Shape Sensing and Distributed Strain Measurements on a Morphing Chevron. 44th AIAA Aerosp. Sci. Meet. Exhib., Reston, Virigina: American Institute of Aeronautics and Astronautics; 2006, p. 1–23. doi:10.2514/6.2006-624.

[117] Askins CG, Miller GA, Friebele EJ. Bend and Twist Sensing in a Multiple-Core Optical Fiber. OFC/NFOEC 2008 - 2008 Conf. Opt. Fiber Commun. Fiber Opt. Eng. Conf., IEEE; 2008, p. 1–3. doi:10.1109/OFC.2008.4528404.

[118] Chan HM, Allen R. Jr. P. In-situ three-dimensional shape rendering from strain values obtained through optical fiber sensors, US Patent 8970845B1, 2015.

[119] Jibson RW. Methods for assessing the stability of slopes during earthquakes—A retrospective. Eng Geol 2011;122:43–50. doi:10.1016/j.enggeo.2010.09.017.

[120] Shanmugam G, Wang Y. The landslide problem. J Palaeogeogr 2015;4:109–66. doi:10.3724/SP.J.1261.2015.00071.

[121] Simeoni L, Mongiovì L. Inclinometer Monitoring of the Castelrotto Landslide in Italy. J Geotech Geoenvironmental Eng 2007;133:653–66. doi:10.1061/(ASCE)1090-0241(2007)133:6(653).

[122] Miller GA, Askins CG, Cranch GA. Interferometric interrogation of a multicore fiber, two-axis inclinometer. In: Jones JDC, editor. 20th Int. Conf. Opt. Fibre Sensors, vol. 7503, 2009, p. 75032R. doi:10.1117/12.835386.

[123] Zheng D, Liu Z, Floris I, Sales S. Temperature-insensitive 2D inclinometer based on pendulum-assisted fiber Bragg gratings. In: Kalli K, Brambilla G, O'Keeffe SO, editors. Seventh Eur. Work. Opt. Fibre Sensors, vol. 1119905, SPIE; 2019, p. 17. doi:10.1117/12.2539286.

[124] Miller GA. Fabrication of a Multifiber Optical Inclinometer. IEEE Photonics Technol Lett 2015;27:1289–92. doi:10.1109/LPT.2015.2420853.

[125] Liu H, Zhu Z, Zheng Y, Liu B, Xiao F. Experimental study on an FBG strain sensor. Opt Fiber Technol 2018;40:144–51. doi:10.1016/j.yofte.2017.09.003.

[126] Wang YL, Shi B, Zhang TL, Zhu HH, Jie Q, Sun Q. Introduction to an FBG-based inclinometer and its application to landslide monitoring. J Civ Struct Heal Monit 2015;5:645–53. doi:10.1007/s13349-015-0129-4.

[127] Li J, Correia R, Chehura E, Staines S, James SW, Tatam RP. A fibre Bragg grating-based inclinometer system for ground movement measurement. In: Santos JL, Culshaw B, López-Higuera JM, MacPherson WN, editors. Proc. SPIE - Int. Soc. Opt. Eng., vol. 7653, 2010, p. 765314. doi:10.1117/12.866334.

[128] Lenke P, Wendt M, Krebber K, Glötzl R. Highly sensitive fiber optic inclinometer: easy to transport and easy to install. 21st Int. Conf. Opt. Fibre Sensors, vol. 7753, 2011, p. 775352. doi:10.1117/12.884695.

[129] MacPherson WN, Silva-Lopez M, Barton JS, Moore AJ, Jones JDC, Zhao D, et al. Tunnel monitoring using multicore fiber displacement sensor. vol. 5855, 2005, p. 274. doi:10.1117/12.623992.

[130] Chen Z, Zhou X, Wang X, Dong L, Qian Y. Deployment of a Smart Structural Health Monitoring System for Long-Span Arch Bridges: A Review and a Case Study. Sensors 2017;17:2151. doi:10.3390/s17092151.

[131] Kang D, Chung W. Integrated monitoring scheme for a maglev guideway using multiplexed FBG sensor arrays. NDT E Int 2009;42:260–6. doi:10.1016/j.ndteint.2008.11.001.

[132] Kissinger T, Chehura E, Staines SE, James SW, Tatam RP. Dynamic Fiber-Optic Shape Sensing Using Fiber Segment Interferometry. J Light Technol 2018;36:917–25. doi:10.1109/JLT.2017.2750759.

[133] Villatoro J, Van Newkirk A, Antonio-Lopez E, Zubia J, Schülzgen A, Amezcua-Correa R. Ultrasensitive vector bending sensor based on multicore optical fiber. Opt Lett 2016;41:832–5. doi:10.1364/OL.41.000832.

[134] Bang H-J, Kim H-I, Lee K-S. Measurement of strain and bending deflection of a wind turbine tower using arrayed FBG sensors. Int J Precis Eng Manuf 2012;13:2121–6. doi:10.1007/s12541-012-0281-2.

[135] Gherlone M, Cerracchio P, Mattone M. Shape sensing methods: Review and experimental comparison on a wing-shaped plate. Prog Aerosp Sci 2018;99:14–26. doi:10.1016/j.paerosci.2018.04.001.

[136] Nicolas M, Sullivan R, Richards W. Large Scale Applications Using FBG Sensors: Determination of In-Flight Loads and Shape of a Composite Aircraft Wing. Aerospace 2016;3:18. doi:10.3390/aerospace3030018.

[137] Freydin M, Rattner MK, Raveh DE, Kressel I, Davidi R, Tur M. Fiber-Optics-Based Aeroelastic Shape Sensing. AIAA J 2019;57:5094–103. doi:10.2514/1.J057944.

[138] Shi C, Luo X, Qi P, Li T, Song S, Najdovski Z, et al. Shape Sensing Techniques for Continuum Robots in Minimally Invasive Surgery: A Survey. IEEE Trans Biomed Eng 2017;64:1665–78. doi:10.1109/TBME.2016.2622361.

[139] Beisenova A, Issatayeva A, Tosi D, Molardi C. Fiber-Optic Distributed Strain Sensing Needle for Real-Time Guidance in Epidural Anesthesia. IEEE Sens J 2018;18:8034–44. doi:10.1109/JSEN.2018.2865220.

[140] Jäckle S, Eixmann T, Schulz-Hildebrandt H, Hüttmann G, Pätz T. Fiber optical shape sensing of flexible instruments for endovascular navigation. Int J Comput Assist Radiol Surg 2019;14:2137–45. doi:10.1007/s11548-019-02059-0.

[141] Beisenova A, Issatayeva A, Iordachita I, Blanc W, Molardi C, Tosi D. Distributed fiber optics 3D shape sensing by means of high scattering NP-doped fibers simultaneous spatial multiplexing. Opt Express 2019;27:22074. doi:10.1364/OE.27.022074.

[142] Parent F, Loranger S, Mandal KK, Iezzi VL, Lapointe J, Boisvert J-S, et al. Enhancement of accuracy in shape sensing of surgical needles using optical frequency domain reflectometry in optical fibers. Biomed Opt Express 2017;8:2210. doi:10.1364/BOE.8.002210.

[143] Roesthuis RJ, Kemp M, van den Dobbelsteen JJ, Misra S. Three-Dimensional Needle Shape Reconstruction Using an Array of Fiber Bragg Grating Sensors. IEEE/ASME Trans Mechatronics 2014;19:1115–26. doi:10.1109/TMECH.2013.2269836.

[144] Khan F, Roesthuis RJ, Misra S. Force sensing in continuum manipulators using fiber Bragg grating sensors. IEEE Int Conf Intell Robot Syst 2017;2017-Septe:2531–6. doi:10.1109/IROS.2017.8206073.

[145] Roesthuis RJ, Kemp M, van den Dobbelsteen JJ, Misra S. Three-Dimensional Needle Shape Reconstruction Using an Array of Fiber Bragg Grating Sensors. IEEE/ASME Trans Mechatronics 2014;19:1115–26. doi:10.1109/TMECH.2013.2269836.

[146] K. Mandal K, Parent F, Martel S, Kashyap R, Kadoury S. Calibration of a needle tracking device with fiber Bragg grating sensors. In: Webster RJ,

Yaniv ZR, editors. Med. Imaging 2015 Image-Guided Proced. Robot. Interv. Model., vol. 9415, 2015, p. 94150X. doi:10.1117/12.2081198.

[147] Henken K, Van Gerwen D, Dankelman J, Van Den Dobbelsteen J. Accuracy of needle position measurements using fiber Bragg gratings. Minim Invasive Ther Allied Technol 2012;21:408–14. doi:10.3109/13645706.2012.666251.

[148] van der Heiden MS, Henken KR, Chen LK, van den Bosch BG, van den Braber R, Dankelman J, et al. Accurate and efficient fiber optical shape sensor for MRI compatible minimally invasive instruments. In: Mazuray L, Wartmann R, Wood AP, de la Fuente MC, Tissot J-LM, Raynor JM, et al., editors. Opt. Syst. Des. 2012, vol. 8550, 2012, p. 85500L. doi:10.1117/12.981141.

[149] Duncan RG, Froggatt ME, Kreger ST, Seeley RJ, Gifford DK, Sang AK, et al. High-accuracy fiber-optic shape sensing. In: Peters KJ, editor. Sens. Syst. Networks Phenomena, Technol. Appl. NDE Heal. Monit. 2007, vol. 6530, 2007, p. 65301S. doi:10.1117/12.720914.

[150] Park Y, Elayaperumal S, Daniel B, Ryu SC, Shin M, Savall J, et al. Real-Time Estimation of 3-D Needle Shape and Deflection for MRI-Guided Interventions. IEEE/ASME Trans Mechatronics 2010;15:906–15. doi:10.1109/TMECH.2010.2080360.

[151] Jäckle S, Strehlow J, Heldmann S. Shape Sensing with Fiber Bragg Grating Sensors. In: Handels H, Deserno TM, Maier A, Maier-Hein KH, Palm C, Tolxdorff T, editors. Bild. für die Medizin 2019, Wiesbaden: Springer Fachmedien Wiesbaden; 2019, p. 258–63. doi:10.1007/978-3-658-25326-4_58.

[152] Henken KR, Dankelman J, Van Den Dobbelsteen JJ, Cheng LK, Van Der Heiden MS. Error Analysis of FBG-Based Shape Sensors for Medical Needle Tracking. IEEE/ASME Trans Mechatronics 2014;19:1523–31. doi:10.1109/TMECH.2013.2287764.

[153] Langer J, Singer D a. Lagrangian Aspects of the Kirchhoff Elastic Rod. SIAM Rev 1996;38:605–18. doi:10.1137/S0036144593253290.

[154] Bauchau OA, Craig JI. Euler-Bernoulli beam theory. In: Bauchau OA, Craig JI, editors. Struct. Anal., Dordrecht: Springer Netherlands; 2009, p. 173–221. doi:10.1007/978-90-481-2516-6_5.

[155] O'Reilly OM. Kirchhoff's Rod Theory. Model. Nonlinear Probl. Mech. Strings Rods Role Balanc. Laws, Cham: Springer International Publishing; 2017, p. 187–268. doi:10.1007/978-3-319-50598-5_5.

[156] Ryu SC, Dupont PE. FBG-based shape sensing tubes for continuum robots. Proc - IEEE Int Conf Robot Autom 2014:3531–7.

doi:10.1109/ICRA.2014.6907368.

[157] Chen Z, Hefferman G, Yuan L, Song Y, Wei T. Terahertz-range interrogated grating-based two-axis optical fiber inclinometer. Opt Eng 2016;55:026106. doi:10.1117/1.OE.55.2.026106.

[158] Moore JP, Rogge MD. Shape sensing using multi-core fiber optic cable and parametric curve solutions. Opt Express 2012;20:2967. doi:10.1364/OE.20.002967.

[159] Joint Committee For Guides In Metrology. JCGM 100:2008, Evaluation of measurement data — Guide to the expression of uncertainty in measurement. 2008.

[160] Joint Committee For Guides In Metrology. JCGM 101:2008, Evaluation of measurement data — Supplement 1 to the " Guide to the expression of uncertainty in measurement " — Propagation of distributions using a Monte Carlo method. 2008.

[161] Synek V. Effect of insignificant bias and its uncertainty on the coverage probability of uncertainty intervals. Part 2. Evaluation for a found insignificant experimental bias. Talanta 2007;71:1304–11. doi:10.1016/j.talanta.2006.06.038.

[162] Papadopoulos CE, Yeung H. Uncertainty estimation and Monte Carlo simulation method. Flow Meas Instrum 2001;12:291–8. doi:10.1016/S0955-5986(01)00015-2.

[163] Shahanaghi K, Nakhjiri P. A new optimized uncertainty evaluation applied to the Monte-Carlo simulation in platinum resistance thermometer calibration. Meas J Int Meas Confed 2010;43:901–11. doi:10.1016/j.measurement.2010.03.008.

[164] Saviano AM, Lourenço FR. Measurement uncertainty estimation based on multiple regression analysis (MRA) and Monte Carlo (MC) simulations – Application to agar diffusion method. Measurement 2018;115:269–78. doi:10.1016/j.measurement.2017.10.057.

[165] Lequin RM. Guide to the Expression of Uncertainty of Measurement: Point/Counterpoint. Clin Chem 2004;50:977–8. doi:10.1373/clinchem.2003.030528.

[166] Floris I, Sales S, Calderón PAPA, Adam JMJM. Measurement uncertainty of multicore optical fiber sensors used to sense curvature and bending direction. Meas J Int Meas Confed 2019;132:35–46. doi:10.1016/j.measurement.2018.09.033.

[167] Kova evi M, Nikezi D, Djordjevich A. Monte Carlo simulation of curvature

gauges by ray tracing. Meas Sci Technol 2004;15:1756–61. doi:10.1088/0957-0233/15/9/011.

[168] Gilman M. A brief survey of stopping rules in Monte Carlo simulations. Second Conf Appl Simulations 1968:16–20.

[169] Dimov IT, McKee S. Monte Carlo Methods for Applied Scientists 2008:1–9.

[170] MATLAB R2015a, The MathWorks, Inc., Natick, Massachusetts US. MATLAB R2015a, The MathWorks, Inc., Natick, Massachusetts, United States n.d.

[171] Floris I, Sales S, Calderón PA, Adam JM. Measurement uncertainty of multicore optical fiber sensors used to sense curvature and bending direction. Meas J Int Meas Confed 2019;132:35–46. doi:10.1016/j.measurement.2018.09.033.

[172] Fender A, MacPherson WN, Maier RRJ, Barton JS, George DS, Howden RI, et al. Two-axis accelerometer based on multicore fibre Bragg gratings. IEEE Sens J 2007;8:66190Q-66190Q – 4. doi:10.1117/12.738411.

[173] Lally EM, Reaves M, Horrell E, Klute S, Froggatt ME. Fiber optic shape sensing for monitoring of flexible structures. In: Tomizuka M, Yun C-B, Lynch JP, editors. Proc. SPIE - Int. Soc. Opt. Eng., vol. 8345, 2012, p. 83452Y. doi:10.1117/12.917490.

[174] Zheng D, Madrigal J, Chen H, Barrera D, Sales S. Multicore fiber-Bragg-grating-based directional curvature sensor interrogated by a broadband source with a sinusoidal spectrum. Opt Lett 2017;42:3710. doi:10.1364/OL.42.003710.

[175] Floris I, Calderón PA, Sales S, Adam JM. Effects of core position uncertainty on optical shape sensor accuracy. Measurement 2019;139:21–33. doi:10.1016/j.measurement.2019.03.031.

[176] Childers BA, Froggatt ME, Allison SG, Moore, Sr. TC, Hare DA, Batten CF, et al. Use of 3000 Bragg grating strain sensors distributed on four eight-meter optical. In: McGowan A-MR, editor., 2001, p. 133–42. doi:10.1117/12.429650.

[177] Yuksel K, Moeyaert V, Megret P, Wuilpart M. Complete Analysis of Multireflection and Spectral-Shadowing Crosstalks in a Quasi-Distributed Fiber Sensor Interrogated by OFDR. IEEE Sens J 2012;12:988–95. doi:10.1109/JSEN.2011.2167142.

[178] Floris I, Madrigal J, Sales S, Adam JM, Calderón PA. Experimental study of the influence of FBG length on Optical Multicore Shape Sensors performance. Opt Lasers Eng 2020;126:105878.

[179] Floris I, Madrigal J, Sales S, Adam JM, Calderón PA. Experimental study of the influence of FBG length on optical shape sensor performance. Asia Commun. Photonics Conf., IEEE; 2019.

[180] Black RJ, Zare D, Oblea L, Park Y-L, Moslehi B, Neslen C. On the Gage Factor for Optical Fiber Grating Strain Gages. Proc Soc Adv Mater Process Eng 2008;52, 2008.

[181] Tosi D. Review and Analysis of Peak Tracking Techniques for Fiber Bragg Grating Sensors. Sensors 2017;17:2368. doi:10.3390/s17102368.

[182] Wolfram S. The Mathematica Book, Fifth Edition. Wolfram Media, Inc; 2003.

[183] Tan F, Liu Z, Tu J, Yu C, Lu C, Tam H-Y. Torsion sensor based on inter-core mode coupling in seven-core fiber. Opt Express 2018;26:19835. doi:10.1364/oe.26.019835.

[184] Love AEH. A Treatise on the Mathematical Theory of Elasticity. vol. 1. 1st ed. Cambridge University Press; 1892.

[185] Floris I, Madrigal J, Sales S, Calderón PA, Adam JM. Twisting compensation of optical multicore fiber shape sensors for flexible medical instruments. In: Gannot I, editor. Opt. Fibers Sensors Med. Diagnostics Treat. Appl. XX, vol. 1123316, SPIE; 2020, p. 41. doi:10.1117/12.2543783.

[186] Floris I, Madrigal J, Sales S, Calderón PA, Adam JM. Twisting measurement and compensation of optical shape sensor based on spun multicore fiber. Mech Syst Signal Process 2020;140:106700. doi:10.1016/j.ymssp.2020.106700.

[187] Floris I, Adam JM, Calderòn PA, Sales S. Measurement uncertainty of 7-core multicore fiber shape sensors. In: Kalli K, Brambilla G, O'Keeffe SO, editors. Seventh Eur. Work. Opt. Fibre Sensors, SPIE; 2019, p. 22. doi:10.1117/12.2539421.

[188] Sun X, Li J, Burgess DT, Hines M, Zhu B. A multicore optical fiber for distributed sensing 2014;9098:1–5. doi:10.1117/12.2050130.

[189] American Association of State Highway and Transportation Officials (AASHTO). AASHTO LRFD Bridge Design Specifications, 8th Edition -. 2017.

[190] Barker MG, Staebler J, Karl E. Barth. Serviceability Limits and Economical Steel Bridge - U.S. Department of Trasportation. Federal Highway Aministration. 2011.

APPENDIX

Appendix A. Results of the simulations for a three-core sensor.

Simulation N°	Core Spacing [µm]	SD Core Position [µm]	Measured Curvature [1/m]	SD Long. Strain [µε]	SD Curvature [1/m]	SD Bend. Direction Angle [rad]
1	30.00	0.20	0.10	0.0116	0.0005	0.0054
2	30.00	0.20	5.00	0.5771	0.0272	0.0054
3	30.00	0.20	40.00	4.6204	0.2177	0.0054
4	30.00	0.80	0.10	0.0462	0.0022	0.0218
5	30.00	0.80	5.00	2.3066	0.1087	0.0218
6	30.00	0.80	40.00	18.4694	0.8714	0.0218
7	30.00	1.50	0.10	0.0866	0.0041	0.0408
8	30.00	1.50	5.00	4.3284	0.2041	0.0409
9	30.00	1.50	40.00	34.6075	1.6336	0.0409
10	50.00	0.20	0.10	0.0115	0.0003	0.0033
11	50.00	0.20	5.00	0.5775	0.0163	0.0033
12	50.00	0.20	40.00	4.6220	0.1307	0.0033
13	50.00	0.80	0.10	0.0462	0.0013	0.0131
14	50.00	0.80	5.00	2.3099	0.0654	0.0131
15	50.00	0.80	40.00	18.4932	0.5224	0.0131
16	50.00	1.50	0.10	0.0865	0.0025	0.0245
17	50.00	1.50	5.00	4.3298	0.1225	0.0245
18	50.00	1.50	40.00	34.6471	0.9793	0.0245
19	70.00	0.20	0.10	0.0116	0.0002	0.0023
20	70.00	0.20	5.00	0.5778	0.0117	0.0023
21	70.00	0.20	40.00	4.6148	0.0933	0.0023
22	70.00	0.80	0.10	0.0462	0.0009	0.0093
23	70.00	0.80	5.00	2.3095	0.0466	0.0093
24	70.00	0.80	40.00	18.4857	0.3732	0.0093
25	70.00	1.50	0.10	0.0866	0.0017	0.0175
26	70.00	1.50	5.00	4.3327	0.0874	0.0175
27	70.00	1.50	40.00	34.6400	0.6996	0.0175
28	140.00	0.20	0.10	0.0115	0.0001	0.0012
29	140.00	0.20	5.00	0.5776	0.0058	0.0012
30	140.00	0.20	40.00	4.6225	0.0467	0.0012

31	140.00	0.80	0.10	0.0462	0.0005	0.0047
32	140.00	0.80	5.00	2.3093	0.0233	0.0047
33	140.00	0.80	40.00	18.4788	0.1867	0.0047
34	140.00	1.50	0.10	0.0866	0.0009	0.0087
35	140.00	1.50	5.00	4.3293	0.0437	0.0088
36	140.00	1.50	40.00	34.6410	0.3498	0.0087
37	300.00	0.20	0.10	0.0116	0.0001	0.0005
38	300.00	0.20	5.00	0.5770	0.0027	0.0005
39	300.00	0.20	40.00	4.6163	0.0218	0.0005
40	300.00	0.80	0.10	0.0462	0.0002	0.0022
41	300.00	0.80	5.00	2.3092	0.0109	0.0022
42	300.00	0.80	40.00	18.4676	0.0871	0.0022
43	300.00	1.50	0.10	0.0867	0.0004	0.0041
44	300.00	1.50	5.00	4.3310	0.0204	0.0041
45	300.00	1.50	40.00	34.6495	0.1633	0.0041

Appendix B. Results of the simulations for a four-core sensor.

Simulation N°	Core Spacing [μm]	SD Core Position [μm]	Measured Curvature [1/m]	SD Long. Strain [με]	SD Curvature [1/m]	SD Bend. Direction Angle [rad]
1	30.00	0.20	0.10	0.0100	0.0005	0.0047
2	30.00	0.20	5.00	0.5001	0.0236	0.0047
3	30.00	0.20	40.00	3.9991	0.1887	0.0047
4	30.00	0.80	0.10	0.0400	0.0019	0.0189
5	30.00	0.80	5.00	1.9989	0.0943	0.0189
6	30.00	0.80	40.00	16.0044	0.7541	0.0189
7	30.00	1.50	0.10	0.0750	0.0035	0.0354
8	30.00	1.50	5.00	3.7510	0.1768	0.0354
9	30.00	1.50	40.00	30.0010	1.4135	0.0354
10	50.00	0.20	0.10	0.0100	0.0003	0.0028
11	50.00	0.20	5.00	0.5004	0.0141	0.0028
12	50.00	0.20	40.00	4.0021	0.1132	0.0028
13	50.00	0.80	0.10	0.0400	0.0011	0.0113
14	50.00	0.80	5.00	1.9989	0.0566	0.0113
15	50.00	0.80	40.00	15.9892	0.4526	0.0113
16	50.00	1.50	0.10	0.0750	0.0021	0.0212
17	50.00	1.50	5.00	3.7508	0.1060	0.0212
18	50.00	1.50	40.00	30.0103	0.8483	0.0212
19	70.00	0.20	0.10	0.0100	0.0002	0.0020
20	70.00	0.20	5.00	0.5004	0.0101	0.0020
21	70.00	0.20	40.00	3.9994	0.0807	0.0020
22	70.00	0.80	0.10	0.0400	0.0008	0.0081
23	70.00	0.80	5.00	2.0007	0.0404	0.0081
24	70.00	0.80	40.00	15.9967	0.3235	0.0081
25	70.00	1.50	0.10	0.0750	0.0015	0.0151
26	70.00	1.50	5.00	3.7499	0.0757	0.0151
27	70.00	1.50	40.00	30.0081	0.6065	0.0152
28	140.00	0.20	0.10	0.0100	0.0001	0.0010
29	140.00	0.20	5.00	0.5001	0.0050	0.0010
30	140.00	0.20	40.00	3.9993	0.0404	0.0010
31	140.00	0.80	0.10	0.0400	0.0004	0.0040
32	140.00	0.80	5.00	1.9990	0.0202	0.0040

33	140.00	0.80	40.00	15.9995	0.1615	0.0040
34	140.00	1.50	0.10	0.0750	0.0008	0.0076
35	140.00	1.50	5.00	3.7529	0.0379	0.0076
36	140.00	1.50	40.00	29.9950	0.3031	0.0076
37	300.00	0.20	0.10	0.0100	0.0000	0.0005
38	300.00	0.20	5.00	0.5001	0.0024	0.0005
39	300.00	0.20	40.00	4.0008	0.0189	0.0005
40	300.00	0.80	0.10	0.0400	0.0002	0.0019
41	300.00	0.80	5.00	1.9991	0.0094	0.0019
42	300.00	0.80	40.00	15.9932	0.0754	0.0019
43	300.00	1.50	0.10	0.0750	0.0004	0.0035
44	300.00	1.50	5.00	3.7487	0.0177	0.0035
45	300.00	1.50	40.00	30.0062	0.1414	0.0035

Appendix C. Results of the simulations for a seven-core sensor.

Simulation N°	Core Spacing [μm]	SD Core Position [μm]	Measured Curvature [1/m]	SD Long. Strain [με]	SD Curvature [1/m]	SD Bend. Direction Angle [rad]
1	30.00	0.20	0.10	0.0076	0.0004	0.0039
2	30.00	0.20	5.00	0.3780	0.0192	0.0038
3	30.00	0.20	40.00	3.0238	0.1540	0.0038
4	30.00	0.80	0.10	0.0302	0.0015	0.0154
5	30.00	0.80	5.00	1.5117	0.0770	0.0154
6	30.00	0.80	40.00	12.0815	0.6158	0.0154
7	30.00	1.50	0.10	0.0567	0.0029	0.0289
8	30.00	1.50	5.00	2.8363	0.1442	0.0289
9	30.00	1.50	40.00	22.6819	1.1552	0.0289
10	50.00	0.20	0.10	0.0076	0.0002	0.0023
11	50.00	0.20	5.00	0.3781	0.0115	0.0023
12	50.00	0.20	40.00	3.0246	0.0924	0.0023
13	50.00	0.80	0.10	0.0302	0.0009	0.0092
14	50.00	0.80	5.00	1.5122	0.0462	0.0092
15	50.00	0.80	40.00	12.0875	0.3695	0.0092
16	50.00	1.50	0.10	0.0567	0.0017	0.0173
17	50.00	1.50	5.00	2.8336	0.0865	0.0173
18	50.00	1.50	40.00	22.6794	0.6927	0.0173
19	70.00	0.20	0.10	0.0076	0.0002	0.0017
20	70.00	0.20	5.00	0.3781	0.0082	0.0016
21	70.00	0.20	40.00	3.0214	0.0660	0.0016
22	70.00	0.80	0.10	0.0302	0.0007	0.0066
23	70.00	0.80	5.00	1.5118	0.0330	0.0066
24	70.00	0.80	40.00	12.1000	0.2642	0.0066
25	70.00	1.50	0.10	0.0567	0.0012	0.0124
26	70.00	1.50	5.00	2.8335	0.0619	0.0124
27	70.00	1.50	40.00	22.6942	0.4947	0.0124
28	140.00	0.20	0.10	0.0076	0.0001	0.0008
29	140.00	0.20	5.00	0.3781	0.0041	0.0008
30	140.00	0.20	40.00	3.0242	0.0330	0.0008
31	140.00	0.80	0.10	0.0302	0.0003	0.0033
32	140.00	0.80	5.00	1.5118	0.0165	0.0033

33	140.00	0.80	40.00	12.0985	0.1319	0.0033
34	140.00	1.50	0.10	0.0567	0.0006	0.0062
35	140.00	1.50	5.00	2.8355	0.0309	0.0062
36	140.00	1.50	40.00	22.6826	0.2476	0.0062
37	300.00	0.20	0.10	0.0076	0.0000	0.0004
38	300.00	0.20	5.00	0.3781	0.0019	0.0004
39	300.00	0.20	40.00	3.0244	0.0154	0.0004
40	300.00	0.80	0.10	0.0303	0.0002	0.0015
41	300.00	0.80	5.00	1.5105	0.0077	0.0015
42	300.00	0.80	40.00	12.0911	0.0616	0.0015
43	300.00	1.50	0.10	0.0567	0.0003	0.0029
44	300.00	1.50	5.00	2.8353	0.0144	0.0029
45	300.00	1.50	40.00	22.6951	0.1154	0.0029